AD-A135 253 HIGH RESOLUTION FREQUENCY SWEPT IMAGING(U) MOORE SCHOOL 1/2
OF ELECTRICAL ENGINEERING PHILADELPHIA PA N H FARHAT
30 SEP 83 ARO-16828.6-EL DAAG29-80-K-0024

UNCLASSIFIED F/G 9/4 NL

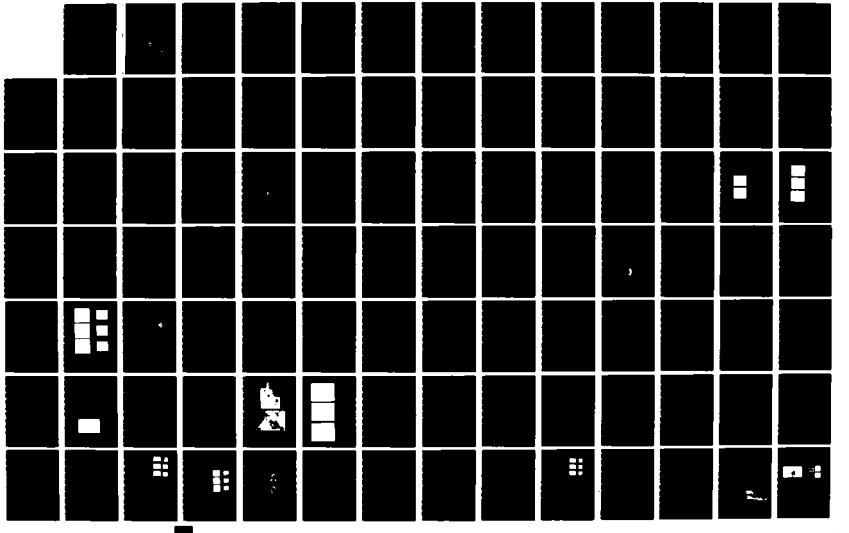

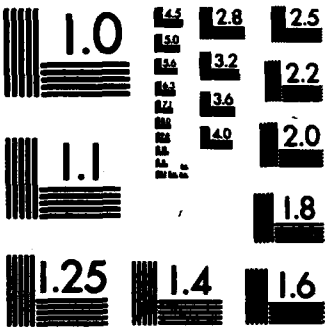

HIGH RESOLUTION FREQUENCY SWEPT IMAGING

FINAL REPORT

PREPARED BY:

N. H. FARHAT

UNIVERSITY of PENNSYLVANIA

The Moore School of Electrical Engineering

PHILADELPHIA, PENNSYLVANIA 19104

HIGH RESOLUTION FREQUENCY SWEPT IMAGING

FINAL REPORT

PREPARED BY:

N. H. FARHAT

SEPTEMBER 30, 1983

U.S. ARMY RESEARCH OFFICE

GRANT NUMBER: DAAG29-80-K-0024 P02

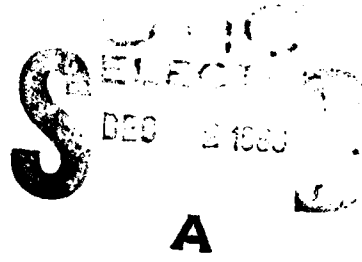

UNIVERSITY OF PENNSYLVANIA
THE MOORE SCHOOL OF ELECTRICAL ENGINEERING
ELECTRO-OPTICS AND MICROWAVE-OPTICS LABORATORY
PHILADELPHIA, PENNSYLVANIA

UNLCASSIFIED

SECURITY CLASSIFICATION OF THIS PAGE *(When Data Entered)*

REPORT DOCUMENTATION PAGE	READ INSTRUCTIONS BEFORE COMPLETING FORM
1. REPORT NUMBER: P2	2. GOVT ACCESSION NO.: AD-A135253	3. RECIPIENT'S CATALOG NUMBER
4. TITLE *(and Subtitle)*: HIGH RESOLUTION FREQUENCY SWEPT IMAGING	5. TYPE OF REPORT & PERIOD COVERED: Final Report July 21, 1980-July 20, 1983
	6. PERFORMING ORG. REPORT NUMBER
7. AUTHOR(s): N.H. Farhat	8. CONTRACT OR GRANT NUMBER(s): DAAG29-80-K-0024
9. PERFORMING ORGANIZATION NAME AND ADDRESS: University of Pennsylvania, The Moore School of Electrical Engineering, 200 S. 33rd St., Phila., PA. 19104	10. PROGRAM ELEMENT, PROJECT, TASK AREA & WORK UNIT NUMBERS
11. CONTROLLING OFFICE NAME AND ADDRESS: U. S. Army Research Office, Post Office Box 12211, Research Triangle Park, NC 27709	12. REPORT DATE: September 30, 1983
	13. NUMBER OF PAGES: 146
14. MONITORING AGENCY NAME & ADDRESS*(if different from Controlling Office)*	15. SECURITY CLASS. *(of this report)*: UNCLASSIFIED
	15a. DECLASSIFICATION/DOWNGRADING SCHEDULE: N/A

16. DISTRIBUTION STATEMENT *(of this Report)*

Approved for public release; distribution unlimited.

17. DISTRIBUTION STATEMENT *(of the abstract entered in Block 20, if different from Report)*

N/A

18. SUPPLEMENTARY NOTES

THE VIEW, OPINIONS, AND/OR FINDINGS CONTAINED IN THIS REPORT ARE THOSE OF THE AUTHOR(S) AND SHOULD NOT BE CONSTRUED AS AN OFFICIAL DEPARTMENT OF THE ARMY POSITION, POLICY, OR DECISION, UNLESS SO DESIGNATED BY OTHER DOCUMENTATION.

19. KEY WORDS *(Continue on reverse side if necessary and identify by block number)*

Microwave imaging, wavelength diversity, polarization diversity, tomography, back-projection, target derived reference, speckle suppression, 3-D display, 3-D point spread function.

20. ABSTRACT *(Continue on reverse side if necessary and identify by block number)*

A Target shape estimation in the context of inverse scattering from far field data is a longstanding problem of considerable present day interest. It can be shown from inverse scattering theory that multiaspect (monostatic or bistatic) frequency or impulse response measurements of the far field of a scattering object can be used to access the 3-D Fourier space or p-space of the object. *Tomographic* or *projection* images of the scattering object can then be reconstructed from the p-space data based on the *projection-slice theorem* stemming from the

DD FORM 1 JAN 73 1473 EDITION OF 1 NOV 65 IS OBSOLETE

UNCLASSIFIED

-1-SECURITY CLASSIFICATION OF THIS PAGE *(When Data Entered)*

multidimensional Fourier transform. The above principles embody the foundation of 3-D tomographic or projective imaging radars capable of furnishing unprecedented resolution through a judicial combination of angular (spatial), spectral, and polarization diversity.

During the period of this report efficient methods for accessing the 3-D Fourier space of conducting and dielectric objects were studied and implemented using a versatile automated microwave measurement and imaging facility. The facility is capable of simulating any innovative or existing radar imaging configuration in the (2-18) GHz range cost-effectively, i.e., without having to actually build a prototype of the imaging aperture. Polarization diversity and automated digital correction of the acquired data for system response and anechoic chamber clutter are provided for. Plans for extending the capabilities of this facility well into the millimeter range are underway. High resolution projection images of complex objects were obtained for the first time from realistic data collected with this facility utilizing wavelength and polarization diversity measurements in the (6-17) GHz. Three-dimensional resolution of one to two centimeters was demonstrated for both conducting and dielectric bodies of complex shape. Efficient accessing of the Fourier space was achieved with the aid of a unique *target derived reference* (TDR) technique that can synthesize the equivalent of a reference point on the target during data processing. The many advantages of the TDR method make the implementation of 3-D tomographic imaging radar concepts practical. Use of polarization information and appriori knowledge of object symmetry are shown to lead to image enhancement and to achieving projection images of several test objects, including a scale model of a B-52, with unprecedented resolution. Similar projection images of dielectric bodies show the excellent potential of 3-D tomographic imaging techniques in nondestructive evaluation (NDE) specially when these are extended to the millimeter wave range.

Several hybrid (opto-digital) 3-D image reconstruction and display methods with potential of real-time operation were studied. These lead to the development of a *Fourier camera*, an incoherent Fourier transform (F.T) technique, suited for use with spatially incoherent scenes including CRT displays. The method is opto-electronic in nature and is based on the projection-slice theorem. Wide dynamic range and complex operation are achieved by elimination of the dynamic bias problem that plagues most incoherent F.T schemes and by using two colors to represent the real and imaginary parts of an input function. Throughputs of one to two orders of magnitude better than digital array processors appear feasible.

The above research is providing the foundations of a new generation of imaging radars capable of yielding 3-D image detail of distant objects with near optical resolution or better especially when operation through atmospheric turbulence and inclement weather is desired.

Also during the period of this report work was initiated on the use of frequency diversity in 3-D imaging of incoherent objects. Experiments conducted using acoustical noise and cross-spectral power density measurements have yielded high resolution projection image of a 3-D distribution of acoustic noise emitters establishing thereby for the first time the validity of accessing the Fourier space of incoherent objects by spectrally selective cross-correlation measurements. This work has important implications in incoherent imaging where the spectral content of random wavefields is utilized to gain information about the 3-D structure of the emitting object. Work in this area and on our Fourier camera are being merged in an investigation of incoherent imaging systems that incorporate smart multiaperture systems akin to those in the compound eye of certain insects. Such systems have the promise of being optimized to perform certain detection and identification tasks better than traditional imaging.

TABLE OF CONTENTS

HIGH RESOLUTION FREQUENCY SWEPT IMAGING

1. INTRODUCTION AND STATEMENT OF THE PROBLEM STUDIED

The implementation of high resolution longwave (microwave and acoustic) inverse scattering or holographic imaging systems involves measurement of the object scattered field over extended recording apertures that subtend sufficiently large solid angles at the object. Because of the discrete nature of longwave sensors, only a sampled version of the scattered field distribution over the recording aperture can be recorded. Sampling considerations ordinarily require dense sampling to avoid retrieved image degradation through deterioration of the impulse response and aliasing. The cost of implementing such densely sampled apertures is at present quite prohibitive because of the large number and high cost of the coherent sensors needed to form the aperture specially for the imaging of remote scattering objects where the extent of the aperture required to yield useful resolution is quite large even at millimeter wavelengths. Obviously *aperture thinning* by reduction of the number of elements can be employed to cut cost. However a systematic study of ordered and random aperture thinning [1],[2] indicates rapid deterioration in resolution and image quality with degree of thinning. The effect of aperture thinning is best described by its influence on the shape and level of side-lobes of the impulse response or point spread function of the aperture [2]. It is generally true that even with an acceptable degree of thinning, where the deterioration of image quality is still tolerable, the cost of longwave apertures remains generally high. To overcome this constraint we have proposed and studied during the period of this report the use of target derived reference techniques [3]-[6],[14] and demon-

strated the utility of wavelength diversity [3],[4] as a means of making a highly thinned (sparse) aperture collect more information about a scattering conducting or nondispersive object thus imparting to the aperture a resolution capability better than would be possible monochromatically at the shortest operational wavelength case. The effect of wavelength diversity can be explained in terms of spectral aperture synthesis or as trade-off between costly spatial degrees of freedom associated with the number of elements and the less costly spectral degrees of freedom associated with wavelength diversity. Specifically one can show from inverse scattering theory [3]-[8] that coherent multiaspect monostatic or bistatic measurements of the far field scattered by a plane wave illuminated nondispersive object as a function of frequency, can be used to access the 3-D Fourier space $\Gamma(\bar{p})$ of the object scattering function $\gamma(\bar{r})$, $\bar{r}$ and $\bar{p}$ being 3-D position vectors in object space and Fourier space, respectively. *The scattering function represents the 3-D geometrical distribution* and strength of those object scattering centers that contribute to the measured field. Normalization of the measured field for range-phase, clutter, and system frequency response leads in principle to accessing a finite volume $\Gamma_m(\bar{p})$ of the Fourier space $\Gamma(\bar{p})$. It is possible then as shown by computer simulation in references [3] and [4] to retrieve a *diffraction* and *noise limited* version $\gamma_d(\bar{r})$ of the object scattering function $\gamma(\bar{r})$ by 3-D Fourier inversion.

Our research program in wavelength and polarization diversity imaging involves the analytical, numerical, and experimental evaluation of the potential and utility of the concepts briefly outlined above for developing the foundations of a new generation of cost-effective imaging radars capable of providing 3-D image information about distant scatterers either *tomographically* or *projectively* with near optical resolution or even better. Such capability will be valuable in

remote and medium range object identification and classification, in developing criteria for radar-cross section management (enhancement or reduction), in nondestructive evaluation (NDE), and remote imaging for damage assessment.

To this end, our research during the period of this report has focused on the study and assessment of efficient and "smart" procedures for data acquisition employing novel TDR techniques. These techniques applied in the 6-17 GHz regime have enabled the accessing of a single slice in the 3-D Fourier space of complex shaped test objects and subsequent reconstruction of a *projection image* of the 3-D distribution of scattering centers. Unprecedented centimeter resolution has been demonstrated using realistic data collected in our *Experimental Microwave Imaging Facility* for a relatively small number of angular "looks" or object aspect angles. Despite their excellent quality, these microwave images indicate several avenues for improvement that have the potential of making them approach and perhaps exceed the quality and resolution of optical and IR imagers whose resolution is limited by turbulent or inclement atmospheric conditions realizing thereby the full potential of wavelength and polarization diversity imaging techniques predicted by theory.

Constraints on accessing the Fourier space over the extended volumes required for the study of true 3-D tomographic imaging imposed by limitations on the volume of data that can be stored in and handled (for example by our present MINC 11/03 computer) have prompted us to examine the concept of tomographic (and projective) image retrieval from incomplete Fourier space data [9] whereby the Fourier space of the scatterer is accessed over a curved surface instead of over a volume as would ordinarily be needed in order to retrieve 3-D object detail. The results (see Appendix V) pave the way for a realistic way of studying 3-D tomographic imaging of scale models of aerospace and other man made objects from actual data collected in our anechoic chamber measurement facility.

During the preceeding period of the program the emphasis has mainly been on the development of static stepped frequency measurement techniques suitable for use in automated measurements of objects that are stationary while the data is being collected. Dynamic frequency swept data acquisition techniques are needed in the imaging of moving targets. We have started the study of such dynamic methods and these will be receiving increased attention in our work. These are being developed for use in demonstrating near optical microwave imagery of for example a passing aircraft.

The thrust of our research in wavelength and polarization diversity in the future will therefore be aimed at the study and development of efficient dynamic data acquisition techniques that can be applied outside the confines of the laboratory and on the detailed study of methods of improving image quality which include the use of *a priori* knowledge and robust (noise tolerant) deconvolution for image enhancement and restoration. The fact that the 3-D accessed Fourier space data can be reduced in dimensionality to 2-D or 1-D through the application of the projection-slice theorem will allow the study and comparison of the effectiveness of 1-D and 2-D enhancement and restoration methods. In fact, reduction of dimensionality is proving to be a most useful and powerful tool in our research in image understanding and processing.

An analysis of the point-spread function (PSF) of idealized wavelength diversity imaging systems shows that considerable advantages of improved resolution and speckle suppression can be obtained by increasing the spectral range beyond the 6-17 GHz range utilized so far in our experimental studies. This is expected however to lead in practice to situations where spectral information can be collected only over separate non overlapping segments of the overall spectral window desired where high power sources, receivers and other gear are available. A segmented spectral

window will then result leading to the accessing of the Fourier space over unconnected regions. The feasibility of using robust interpolation methods to "fill in" the data in the missing bands will therefore be considered in our future research. The experimental counterpart of this future research requires extending the lower frequency bound of our measurement system down to 2 GHz or lower and the upper bound initially to 40 GHz. Reducing the lower bound of our system from 6 GHz to 2 GHz is particularly important for supressing certain resonance effects apparent in the images retrieved so far, while increasing the upper bound will lead to visualization of finer detail of the test objects utilized in our studies. The net effect is expected to be a dramatic improvement of image quality beyond the good images of Laboratory scale objects already obtained and to better prediction of the imaging performance of broadband microwave systems with real-world objects.

To fully utilize the 3-D imaging capabilities of wavelength and polarization diversity imaging we have been also concerned with the study of high speed hybrid (opto-digital) computing as a means for true 3-D image reconstruction and display. The ability to display a true 3-D image is extremely important for exploiting the full potential of the human eye-brain system in recognition specially when the number of the 3-D distributed microwave scattering centers on a visualized target is limited. One hybrid computing scheme being studied (see Appendix VI) is based on carrying out a series of 2-D optical Fourier transforms of *weighted projection holograms*, corresponding to different slices of the object, at very high frame rates employing incoherent light. The ability to perform 2-D fourier transforms of natural scenes at high speed with this scheme provides a new means of 3-D image formation based again on the projection-slice theorem which will be considered also in our future work in addition to our research in 3-D incoherent imaging techniques based on spectrally selective cross-correlation measurements (see Appendix IX). Both of the above aspects of our research are leading our

research to the consideration of multiaperture systems capable of performing specific remote sensing tasks with high efficiency as in certain biological systems [10],[11].

2. SUMMARY OF IMPORTANT RESULTS

The research program covered by this final report was initiated to study and develop optimal data acquisition and image reconstruction procedures suitable for use in inverse scattering and three-dimensional microwave imaging by wavelength and polarization diversity. Important findings and accomplishments of the program and conclusions that can be drawn from them are summarized below. Details are found in Appendices I to XI.

(a) The first centimeter resolution microwave projective and tomographic imagery of scattering centers of a complex conducting target from data measured utilizing frequency, angular, and polarization diversity techniques is demonstrated. This is achieved with realistic microwave scattering data obtained with a versatile experimental microwave imaging facility consisting of a network analyzer that was designed, assembled and installed in an anechoic chamber environment under partial support from this program. A variety of test targets are utilized in the study ranging from simple to complex shaped targets. Digital signal processing techniques are employed in the preprocessing and image retrieval.

(b) Several TDR (target derived reference) schemes were conceived and evaluated for the purpose of removing the range-phase term from the collected data to facilitate accessing the 3-D Fourier space of the scatterer. One of these involving: (i) precise range estimation from each coherent T/R (transmitter/receiver) station interrogating the target from different aspects to a

prominent visible scattering center on the target or to a scattering centroid, and (ii) use of successive cross-correlation of adjacent angular records for fine phase-adjustment "phase tweeking", was shown to be practical enabling the retrieval of imagery with unprecedented resolution.

(c) Microwave image reconstruction using a filtered-back projection scheme as opposed to the Fourier inversion scheme was studied and demonstrated for the first time in microwave imaging.

(d) Three-dimensional imaging of dielectrics was studied and demonstrated in the context of non-destructive evaluation.

(e) The utility of our microwave measurement facility, not only in microwave imaging studies, but also as a versatile tool for characterizing and evaluating the performance of microwave components and devices such as antennas, amplifiers, modulators ... etc., and in instrument calibration over a wideband of frequencies covering 2-18 GHz range was established.

(f) High quality images were obtained using digital image reconstruction algorithms based on far field inverse scattering considerations under the physical optics and Born approximations. These demonstrate that the physical optics scattering regime can furnish a viable approach for imaging the scattering centers of an object.

(g) The multiaspect frequency response data used in image formation were obtained from far field measurements done without having to maintain phase coherence from one frequency response measurement to another. This has important implications when multi-aspect interrogation of the scatterer with an array of widely spaced broadband monostatic coherent transmitter/receiver stations is employed as the mode for data acquisition. It means that maintenance of phase coherence between the sources at the various stations is not essential during data acquisition. The phase coherence is introduced through the TDR technique during data

processing. This eliminates the need for reference signal distribution networks which are known to be a major obstacle in the realization of giant microwave coherent imaging apertures because of economical and practical constraints on their implementation and is expected to considerably reduce atmospheric phase distortions and doppler effects in wavelength diversity imaging of remote moving targets.

(h) A study of phase retreival from amplitude data in the context of inverse scattering and wavelength diversity imaging was conducted because of the great simplicity of measuring amplitude alone instead of amplitude and phase. It is found that the individual frequency responses of a scatterer are *causal* but not *minimum phase*. As a result phase retreival from amplitude through the Hilbert transform does not appear to be viable. Preliminary results of a digital simulation show however that phase information retreived from multiaspect amplitude responses of a test object consisting of a collection of point scatterers yields the correct image plus additional spurious detail. Further investigation of this aspect of our study is planned.

(i) The Fourier domain slice data accessed by the microwave imaging system described in our work (see Appendix VII) is identical to the Fourier domain data that one might access in the inverse SAR geometry of Fig. 2 (a) of Appendix VII or the imaging radar network geometry of Fig. 2 (b) of Appendix VII. The equivalence of the latter two geometries can be verified by drawing the $\bar{p}$-space sampling format for these equivalent geometries to find that they are identical since both access the $\bar{p}$-space of the scatterer over the same range of aspect angles one doing so sequentially in time as the scatterer progresses in its flight and the other acquiring the same data all at once. The question of $\bar{p}$-space data acquisition in the presence of scatterer motion is not discussed in our reported work since the emphasis has been on imagery of stationary scatterers in an anechoic chamber

environment. As mentioned earlier a study of accessing the $\bar{p}$-space of a scatterer in the presence of relative motion is currently underway.

(j) Because the TDR technique results in a recording configuration similar to that of a lensless Fourier transform hologram, the resolution and spacial sampling requirement from the recording device (recording aperture) are greatly relaxed. This leads to significant reduction of the number of receiving elements in the recording aperture that are needed to achieve good image quality.

(k) Because in addition to being dependent on geometry the dimensions of the acquired three-dimensional data manifold in $\bar{p}$-space are dependent on the spectral range of the incident wave, super-resolution (i.e., resolution beyond the classical limit of the available physical aperture) is achieved. This aperture synthesis by frequency diversity further helps in cutting down array cost, since a highly thinned array aperture can be used to frequency synthesize a larger array with higher filling factor.

(l) One of the significant accomplishments of this phase of our program has been the use of a vector reformulation of inverse scattering in an experimental demonstration of frequency diversity imaging that accounts fully for the vector nature of the electromagnetic field and provides therefore ways in which polarization diversity can be utilized to improve image quality.

(m) Customarily, the scattering function $\gamma(\bar{r})$ (see Appendix VII) is identified as the scattering function of the object, defined when the object is perfectly reflecting, as unity within it and zero outside [7],[8]. The results presented in Appendix VII show that in practice $\gamma(\bar{r})$ can assume zero values on those parts of scatterer's surface that are not seen by the imaging system (i.e., do not scatter radiation in the direction of the observation points but rather scatter it specularly away from them). An example is found in the case of the flat wing sections and other gross detail in imagery presented in Appendix VII.

(n) The data collected by a thinned array of coherent receivers intercepting the wavefield scattered from a distant target, as the frequency of its illumination and/or its direction of incidence is changed, can be stored as a three-dimensional data manifold in Fourier domain from which a 3-D image of the target can be retrieved by means of (i) a three-dimensional Fourier transform, (ii) a sequence of two-dimensional Fourier transforms based on the weighted Fourier projection theorem, or (iii) a sequence of one-dimensional Fourier transform and using the filtered-back-projection theorem. The PSF (Point Spread Function) is spatially variant since the size and shape of the three-dimensional data manifold in $\bar{p}$-space and therefore the PSF and resolution will depend on the relative positions between the target, transmitter and receiving array and also on the spectral range of the illumination utilized.

(o) Assuming the scattering process is linear, the frequency response of a scatterer is related to the impulse response by a Fourier transform. This means that when impulse illumination is utilized, instead of frequency swept illumination, a three-dimensional manifold in $\bar{p}$-space may be generated by Fourier transforming the far field impulse response measured at each receiver, correcting for unequal delay times, and storing the result in $\bar{p}$-space of the object at the values of $\bar{p}$ accessed by each receiver. The image reconstruction algorithms utilized in our work and referred to earlier can then be used to yield three-dimensional image information. Time domain inverse scattering concepts as extensively studied for example by Moffatt [12] and Bennett [13] are then applicable.

(p) Projection imagery of characteristic highlights or scattering centers of complex shaped targets of the kind employed in our work is shown to provide sufficient geometrical image detail to enable target classification and identification which is the goal in a modern imaging radar system.

(q) The centimeter resolution referred to in item (a) is demonstrated through the use of frequency diversity in the 6-17 GHz range and angular diversity over 90° (polarization diversity that combines two orthogonal states of polarizations in the data acquisition can also be used) and through the use of digital image reconstruction and enhancement algorithms. Excellent microwave image quality is obtained from data contained in a single finite slice of the Fourier domain accessed in a polar format of 128 equally spaced radial lines covering an angle of 90° with each radial line containing 128 complex data points covering a spectral window of 6-17 GHz. A study, of the effect of angular aperture reduction and thinning, shows that reducing the number of radial lines (angular looks) covering the 90° angular aperture from 128 to 32 causes little change in image quality while narrowing the angular aperture to 45° does not degrade the image quality to a degree that renders it unrecognizable.

(r) The retrieved image is nearly free of speckle noise which plagues conventional coherent imaging systems. Speckle noise suppression is attributed to frequency diversity which tends to suppress and smooth out the side-lobes of the impulse response (or PSF) of a coherent imaging system making it behave thereby like a speckle-free incoherent imaging system as discussed in Appendix X.

(s) The range resolution of the wavelength diversity imaging process studied in our work will not deteriorate with range to the target, as long as signal-to-noise ratio and the extent of the spectral and angular (aspect) windows utilized are preserved. This lends credence to the proposal of cost-effective, extremely broadband coherent radar networks composed of several tens of stations distributed over continental distance for use in the imaging and identification of aerospace targets with centimeter resolution. Such resolution may surpass the capability of conventional optical system whose resolution, un-

like microwave systems, is severely degraded by atmospheric turbulance.

(t) Linear and nonlinear digital image processing using a priori and a posteriori knowledge can be applied to modify the original reconstructed image to an enhanced version more informative subjectively pleasing to the observer. This indicates that a powerful image processor is a necessary tool for the future research work in the M.O./E.O. Laboratory. In the future this will be achieved by connecting our MINC 11/2 computer to a VAX 750 made accessible to our work by the Artificial Intelligence and Robotics Laboratory of the Moore School.

(u) The techniques developed demonstrate that microwave tomographic imaging systems can be used in the study of not only conducting scatterers but also dielectric objects for non-destructive evaluation.

(v) The results of the tomographic imagery presented in this report show that more research work is necessary in studying recording geometries and image processing in order to present a three-dimensional tomographic image cost-effectively, for example through the use of inverse convolution (deconvolution) techniques that can remove the effect of the PSF of the $\bar{p}$-space accessed by the highly thinned semi-circular apertures considered in Appendix V.

(w) The microwave imaging approach studied in our work has the potential of being implementable in a real-time microwave imaging radar with the aid of advanced microwave instrumentation such as comb generators, channelized receivers, monopulse trackers, and array processors and coherent and noncoherent hybrid (opto-digital) computing devices that have the potential for furnishing true 3-D image display.

(x) The concepts of 3-D tomographic and projective imaging by wavelength and angular diversity studied extensively in our work are extendable to interferometric imaging of 3-D incoherent objects (see Appendix XI). Preliminary experimental results obtained using ultrasound are extremely encouraging. These

lay the foundation for passive imaging radiometers in which the spectral degrees of freedom of the random wave-field generated by the object can be utilized to obtain 3-D detail.

We conclude this section by noting several areas of application which would benefit from the findings reported here when either microwave or acoustical radiations are utilized.

(a) Construction of images of distant aero-space objects, surface vessels, and submerged objects.

(b) Nondestructive evaluation of dielectric products and materials.

(c) Detection and identification of buried objects.

(d) Biomedical imaging of tumors for medical diagnosis.

(e) Active or passive remote sensing for resource identification, recovery, and management.

(f) Prediction of storms and tornados.

(g) Analysis and synthesis of microwave networks.

(h) Speech analysis.

3. REFERENCES

1. N.H. Farhat, "Longwave Holography", in *Holography in Medicine*, P. Greguss (Ed.), IPC Science and Technology Press, Richmond (England), 1975.

2. N.H. Farhat, et. al., "Real-Time Microwave Holography - A Feasibility Study", University of Pennsylvania Report - Prepared for University Science Center Inc., Oct. 1972.

3. N.H. Farhat and C.K. Chan, "Three-Dimensional Imaging by Wave-Vector Diversity", Presented at the 8th Int. Symp. on Acoust. Imaging, Key Biscayne, Fla., 1978 and published in *Acoustical Imaging*, Vol. 8, A. Metherell (Ed.), pp. 499-516, Plenum Press, New York 1980.

4. C.K. Chan and N. Farhat, "Frequency Swept Tomographic Imaging of Three-Dimensional Perfectly Conducting Objects", IEEE Trans. on Ant. and Prop., Special Issue on Inverse Methods in Electromagnetics, Vol. AP-29, pp. 312-319, March 1981.

5. N.H. Farhat, W.I. Landauer and W.E. Wallace, "Computer Assisted Naval Applications of Holography", Computer Command and Control Co., Report No. 132-4, prepared for Naval Analysis Programs, Office of Naval Research under contract No. N0014-69-C-0167, February 1973.

6. N. Farhat, C.K. Chan and T.H. Chu, "A Target Derived Reference Technique for Frequency Diversity Imaging", North American Radio Science Meeting, Quebec, 1980.

7. N. Bojarski, "Inverse Scattering", Naval Air Command Final Report N000 19-73-C-0312F, Feb. 1974.

8. R.M. Lewis, "Physical Optics Inverse Diffraction", IEEE Trans. on Ant. and Prop., Vol. AP-17, pp. 308-314, May 1969.

9. N.H. Farhat, "Inverse Scattering Reconstructions From Incomplete Fourier Space Data", Presented at and Published in the Technical Digest of the OSA/AFOSR 1983 Topical Meeting on Signal Recovery and Synthesis with Incomplete Information and Partial Constraints", Lake Tahoe, Nevada.

10. C. Alexoff, "Limits of Passive Imaging", ERIM Rept. 0484, Aug. 1983. Proc. of ARO/ERIM Wrokshop held May 24-26, 1983, Mackinak Island, Mich.

11. J.J. Hopfield, "Neural Networks and Physical Systems With Emergent Collective Computational Abilities", Proc. Natl. Acad. Sci., USA, Vol. 79, pp. 2554-2558, April 1982.

12. H.C. Moffat et.al., "Transient Response Characteristics in Identification and Imaging", IEEE Trans. on Ant. and Prop., Vol. AP-29, pp. 195-205, March 1981.

References - Continued

13. C.L. Bennett, "Time Domain Inverse Scattering", IEEE Trans. on Ant. and Prop., Vol. AP-29, pp. 213-219, March 1981.

14. N.H. Farhat, T.H. Chu and C.L. Werner, "Tomographic and Projective Reconstruction of 3-D Image Detail in Inverse Scattering", Proc. of the 10th Int. Opt. Computing Conference on "Unconventional Imaging and Unconventional Transformation", Boston. IEEE Cat. No. 83CH1880-4. (1983)

4. LIST OF PUBLICATIONS

During the period of this report the following publications and presentations were made:

1. N.H. Farhat and C.K. Chan, "Three-Dimensional Imaging by Wave-Vector Diversity", Presented at the 8th Int. Symp. on Acoust. Imaging, Key Biscayne, Fla., 1978 and published in *Acoustical Imaging*, Vol. 8, A. Metherell (Ed.), pp. 499-516, Plenum Press, New York 1980.

2. C.K. Chan and N. Farhat, "Frequency Swept Tomographic Imaging of Three-Dimensional Perfectly Conducting Objects", IEEE Trans. on Ant. and Prop., Special Issue on Inverse Methods in Electromagnetics, Vol. AP-29, pp. 312-319, March 1981.

3. N.H. Farhat, "Holography, Wavelength Diversity, and Inverse Scattering", in *Optics in Four Dimensions*, M.A. Machado and L.M. Narducci Eds., Am. Inst. of Physics, New York (1981).

4. N.H. Farhat and C.Y. Ho, "The Virtual Fourier Transform and its Application in Three Dimensional Display", in *Optics in Four Dimensions*, M.A. Machado and L.M. Narducci Eds., Am. Inst. of Phys., New York, (1981).

5. N.H. Farhat, "Projection Theorems and Their Applications In 3-D Tomographic Image Reconstruction and Display", Poster Session paper presented at the Gordon Research Conference on Holography and Optical Data Processing, Plymouth, N.H., June 1982.

6. N.H. Farhat, "Tomographic and Projective Reconstruction of 3-D Image Detail in Inverse Scattering", Presented at the *1983 URSI Meeting*, Jan. (5-7), Boulder, Colorado.

7. N.H. Farhat, "Inverse Scattering Reconstructions From Incomplete Fourier Space Data", Presented at and published in the Technical Digest of the OSA/AFOSR 1983 Topical Meeting on *Signal Recovery and Synthesis with Incomplete Information and Partial Constraints*, Jan. 12-14, Lake Tahoe, Nev.

8. N.H. Farhat, C. Yi Ho, and Li Szu Chang, "Projection Theorems and their Applications in Multidimensional Signal Processing", Presented at the Conference on *Advances in Optical Signal Processing* at the SPIE LA/'83 Meeting, Jan. 1983, Also to be published in the Conference Proceeding.

9. N.H. Farhat, C.L. Werner and T.H. Chu, "Tomographic and Projective Reconstruction of 3-D Image Detail in Inverse Scattering", Proceedings of the 10th International Optical Computing Conference on "Unconventional Imaging and Unconventional Transformations", Boston April 1983. IEEE Cat. No. 83CH1880-4. (1983)

List of Publications - Continued

10. N.H. Farhat, D.L. Jaggard, T.H. Chu, D.B. Ge and S. Mankoff, "Microwave Tomographic and Projective Imaging of Dielectric Bodies", presented at the 1983 International IEEE/APS/URSI Meeting, May 23-26, Houston, TX.

11. N.H. Farhat and C.L. Werner, "An Automated Microwave Measurement Facility for Three Dimensional Tomographic Imaging by Wavelength Diversity", presented at the 1981 Int. IEEE AP-S Symp. and National Radio Science Meeting, L.A., June 1981.

12. N.H. Farhat, D.L. Jaggard, T.H. Chu, D.B. Ge and S. Mankoff, "Microwave Imaging of 3-D Dielectric Bodies", presented at the 3rd Annual Benjamin Franklin Symposium, Philadelphia, April 30, 1983.

5. LIST OF PARTICIPATING SCIENTIFIC PERSONNEL AND DEGREES AWARDED

Personnel

Lie-Szu Chang	-	Graduate Student
T.H. Chu	-	Graduate Student
N.H. Farhat	-	Principal Investigator
C. Yi Ho	-	Graduate Student
H. J. Lee*	-	Graduate Student
G. Shah*	-	Graduate Student
S. Tejima*	-	Graduate Student
C.L. Werner	-	Graduate Student

Also during the latter part of the period covered by this report our research effort was joined by Dr. Dwight L. Jaggard, who is an expert in the areas of inverse scattering and propagation in semi-periodic media.

Degrees Awarded

Ph.D.:

C.Yi Ho, "Real-Time Three-Dimensional Image Reconstruction and Display" (1982).

T.H. Chu**, "Optimal Methodologies in Inverse Scattering" (1983).

---

* Participating student not supported by grant.

** Recipient of the 1983 University of Pennsylvania Sigma Xi Best Dissertation Award.

M.Sc.:

S. Tejima, "Implicit Sampling and the Incoherent Optical Fourier Transform" (1980).

C.L. Werner, "An Automated Frequency Response and Radar Cross-Section Measurement Facility for Microwave Imaging" (1980).

H.J. Lee, "Broad-Band Microstrip Antennas" (1980).

T.H. Chu, "Signal Processing in Microwave Holography" (1980).

Lie-Szu Chang, "Optical Fourier Transform Utilizing Incoherent Light" (1983).

6. APPENDICES

APPENDIX I

THREE DIMENSIONAL IMAGING BY WAVE-VECTOR DIVERSITY

(Paper presented at the 8th Int. Symp. on Acoust. Imaging, Key Byscayne, Fla. and published in *Acoustical Imaging*, Vol. 8, A.F. Metherell (Ed.), Plenum Publishing Corp., New York, 1980)

From: ACOUSTICAL IMAGING, Vol. 8
Edited by A.F. Metherell
(Plenum Publishing Corporation, 1980)

THREE DIMENSIONAL IMAGING BY WAVE-VECTOR DIVERSITY

N. H. FARHAT and C.K. CHAN

University of Pennsylvania

200 S. 33rd St., Philadelphia, PA., 19174

ABSTRACT

A method for the three dimensional imaging of objects by wave-vector diversity (frequency and viewing and/or illumination angle diversity) is analyzed using a Fourier Optics approach. The analysis is applicable to two classes of objects of practical interest namely weakly scattering objects and perfectly reflecting objects. It is shown that under frequency swept plane wave illumination the data collected by an array of receivers deployed in the far field of the object represents a 3-D data manifold that is within a quadratic phase factor equal to the 3-D Fourier transform of the object function. Methods for removal of the quadratic phase factor which otherwise can lead to image distortion are discussed. By invoking Fourier domain projection theorems we show that the distortion corrected 3-D data manifold can yield a reconstruction of the object slice by slice or all at once using integral holography. Similarities between wave-vector diversity imaging and possible "imaging" features in certain cetacean and in the bat are pointed out.

1. INTRODUCTION

The development of longwave (acoustic or microwave) holographic imaging systems possessing resolution and image quality approaching those of optical systems is hampered by three factors: (a) prohibitive cost and size of longwave imaging apertures, (b) inability to view a 3-D image as in optical holography and (c) degradation of image quality by speckle noise because of the low numerical apertures attainable with present techniques. For ex-

ample, a longwave imaging aperture operating at a wavelength of 3 cm should be about 3 km in size in order to achieve image resolution comparable to an ordinary photographic camera. In addition to inconvenient size, the cost of filling such a large aperture with suitable coherent sensors is clearly prohibitive. Furthermore, recall that in conventional longwave holography when optical image retrival is utilized, it is necessary to store the longwave hologram data (fringe pattern) in an optical transparency suitable for processing on the optical bench using laser light. In order to avoid longitudinal distortion* of the reconstructed image, the size of the optical hologram replica must be m ($= \lambda_{long}/\lambda_{laser}$) times smaller than the longwave recording aperture. For the example cited earlier, this means an optical hologram replica of less than a millimeter in size. It is certainly not possible to view a virtual 3-D image through such a minute hologram even with optical aids since these tend to introduce their own longitudinal distortion. As a result, longwave holographers have long learned to forgo 3-D imagery and settled instead for 2-D imagery obtained by projecting the reconstructed real image on a screen. This permits lowering of the reduction factor m and consequently lowering of the resolution requirements of the photographic film. This permits in turn the use of highly convenient Polaroid transparency film for preparation of the optical hologram replica. Because of the small size (measured in wavelength) of longwave apertures attainable in practice and the above method of viewing the real image, speckle noise is always present leading to degradation in image quality.

In this paper we describe and analyze an imaging method that utilizes wave-vector diversity (frequency and viewing and/or illumination angle diversity) that circumvents the limitations discussed above. It is worthwhile to point out that our studies of wave-vector diversity imaging (or frequency swept imaging) are motivated to a large extent by evidence of super-resolved "imaging" capabilities by frequency sweeping in certain cetacean and in the bat which are known to use frequency swept signals in their "sonar". We first present the theoretical principles of the method. Fourier-domain projection theorems are discussed next and utilized to illustrate the ability of the method to provide 3-D image information. This is followed by a presentation of the results of a computer simulation. Finally the features of wave-vector diversity imaging are summarized and the similarities to "imaging" procedures in the dolphin and in the bat are pointed out.

*Longitudinal distortion causes for example the image of a sphere to appear elongated in the range direction like a very long ellipsoid.

2. ANALYTICAL CONSIDERATION

In this section we present a Fourier-Optics analysis of wave-vector diversity imaging first of a two dimensional object in which there is no restriction on the object orientation relative to the transmitter and the receiver. This is followed by extension to three dimensional objects.

Consider an isolated planar object of finite extent with reflectivity $D(\bar{\rho}_o)$, where $\bar{\rho}_o$ is a two dimensional position vector in the object plane (x_o,y_o). The object is illuminated as shown in Figure 1(a) by a coherent plane wave of unit-amplitude and of wave vector $\bar{k}_i = k\,\bar{l}_{ki}$ produced by a distant transmitter located at $\bar{R}_T$. The wavefield scattered by the object is monitored at a distant receiver at $\bar{R}_R$ lying in the far field region of the object. The position vectors $\bar{\rho}_o$, $\bar{R}_T$ and $\bar{R}_R$ are measured from the origin of a cartesean coordinate system (x_o,y_o,z_o) centered on the object. The object is assumed to be nondispersive i.e., D is independent of k. However, when the object is dispersive such that $D(\bar{\rho}_o,k) = D_1(\rho_1)D_2(k)$ and $D_2(k)$ is known, the analysis presented here can easily be modified to account for such object dispersion by correcting the data collected as k is changed for $D_2(k)$.

Referring to Figure 1(a) and ignoring polarization effects, the field amplitude at $\bar{R}_T$ caused by the object scattered wavefield may be expressed as,

$$\psi(k,\bar{R}_R) = \frac{jk}{2\pi} \int D(\bar{\rho}_o) e^{-j\bar{k}_i \cdot \bar{r}_T} \frac{e^{-jk\, r_R}}{r_R} \, d\bar{\rho}_o \qquad (1)$$

where $d\bar{\rho}_o$ is an abbreviation for $dx_o dy_o$ and the integration is carried out over the extent of the object. Noting that $\bar{r}_T = \bar{\rho}_o - \bar{R}_T$, $\bar{R}_T = -R_T \bar{l}_{k_i}$ and using the usual approximations valid here: $r_R \simeq R_R + \rho_o^2/2R_R - \bar{l}_R \cdot \bar{\rho}_o$ for the exponential in (1) and $r_R \simeq R_R$ for the denominator in (1) where $\bar{l}_R = \bar{R}_R/R_R$ and $\bar{l}_{k_i} = \bar{k}_i/k$ are unit vectors in the $\bar{R}_R$ and $\bar{k}_i$ directions respectively, one can write eq. (1) as,

$$\psi(k, \bar{R}_R) = \frac{jk}{2\pi R_R} e^{-jk(R_T + R_R)} \int D(\bar{\rho}_o)\, e^{-j\,\bar{p} \cdot \bar{\rho}_o} \, d\bar{\rho}_o, \qquad (2)$$

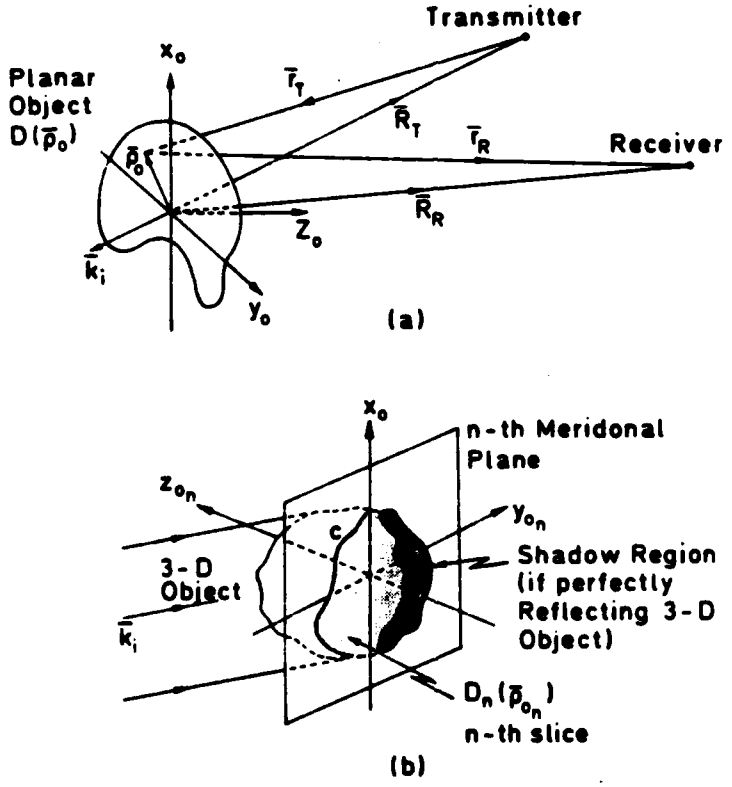

Fig. 1. Geometry for Wave-Vector Diversity Imaging of (a) a two dimensional object and (b) three dimensional object showing a meridonal slice.

where we have used the fact that the observation point is in the far field of the object so that exp $(-j\, k\rho^2/2R_R)$ under the integral sign can be replaced by unity. In eq. (2), $\bar{p} = k\,(\bar{l}_{k_i} - \bar{l}_R) \triangleq p_x\,\bar{l}_x + p_y\,\bar{l}_y + p_z\,\bar{l}_z$ is a three dimensional vector whose length and orientation depend on the wavenumber k and the angular positions of the transmitter and the receiver. For each receiver and/or transmitter present, $\bar{p}$ indicates the position vector for data storage. An array of receivers for example would yield therefore as k is changed (frequency diversity)or as $\bar{k}$ $(=k\bar{l}_{k_i})$ is charged (wave-vector diversity) a 3-D data manifold. The projection of this 3-D data manifold on the object plane yields $\psi(k,\bar{R}_T)$ because $\bar{p}\cdot\bar{\rho}_o = \bar{p}_t \cdot \bar{\rho}_o = p_x x_o + p_y y_o$ where $p_x = k(\bar{l}_{k_i} - \bar{l}_R)_x$ and $p_y = k(l_{k_i} - l_R)_y$ are the cartesian components of the projection $\bar{p}_t$ of $\bar{p}$ on the object plane. Accordingly eq. (2) can be expressed as,

$$\psi(k,R_R) = \frac{jk}{2\pi R_R}\, e^{-jk(R_T + R_R)} \int D(x_o,y_o)\, e^{-j(p_x x_o + p_y y_o)}\, dx_o dy_o \qquad (3)$$

Because of the finite extent of the object, infinite limits can be assumed and the integral in (3) is recognized as the two dimensional Fourier transform $\tilde{D}(p_x, p_y)$ of $D(x_o, y_o)$. It is seen to be dependent on the object reflectivity function, the angular positions of the transmitter and the receiver, and on the values assumed by the wavenumber k but is entirely independent of range. Data containing $\tilde{D}$ can thus be collected by varying these parameters. The range information is contained solely in the factor $F = k \exp[-jk(R_T + R_R)]/2\pi R_R$ preceeding the integral. The field observed at R_T has thus been separated into two terms one of which, $\tilde{D}$, contains the lateral object information and the other, F, contains the range information. The presence of F in eq (3) hinders the imaging process since it complicates data acquisition and if not removed, gives rise to image distortion because R_R is generally not the same for all receivers. To retrieve an image of the object via a 2-D Fourier transform of eq. (3) (what can be carried out optically), the factor F must first be eliminated. This operation yields $\tilde{D}$ over a two dimensional region in the p_x, p_y plane. The size of this region, which determines the resolution of the retrieved image[1,2] depends on the angular positions of the transmitter and the receiver and on the values assumed by k, i.e. the width and position of the spectral window employed. The later dependence on k implies super-resolution

imaging capability because of the frequency synthesized dimension of the 3-D data manifold generated. Because of the dependence of resolution on the relative positions of the object, the transmitter, and receiver (or receiver array), the impulse response is clearly spatially variant. In fact a receiver situated at $\bar{R}_T$ for which $\bar{p}$ is normal to the object plane can not collect any lateral object information because for this condition ($\bar{p} \cdot \bar{\rho}_o = 0$) the integrals in (2) and (3) yield a constant.

Such a receiver is located in the direction of specular reflection from the object where the diffraction pattern is stationary i.e. does not change with k. In this case the observed field is solely proportional to F containing thus range information only. Obviously this case can easily be avoided through the use of more than one receiver which is required anyway when 2-D or 3-D objects resolution is sought.

Several methods for the elimination of F from the collected data appear possible. These include: (a) By furnishing a target derived reference (TDR) to the receivers by means of Porter's method (3) (b) By optical filtering (4), (c) By high speed analog-to-digital conversion and storage of the signals detected by receivers that are furnished with a common reference signal derived from or phase-locked to the transmitter. In this later case, digital correction for F can then be performed using apriori knowledge (obtained by other independent means) of R_R for each receiver. The most attractive of these, the TDR method, is currently under experimental study.

The analysis presented here can be extended to three dimensional objects by viewing a 3-D object as a collection of thin meridonal slices (see Fig. 1 (b)) each of which represents a two dimensional object of the type analyzed here. With the n-th slice we associate a cartesean coordinate system x_o, y_{o_n}, z_{o_n} that differ from other slices by rotation about the common x_o axis. Since the vectors $\bar{p}$, $\bar{R}_T$ and $\bar{R}_R$ are the same in all n-coordinate systems, eq (3) holds. $\psi_n(k,\bar{R}_T)$ is then obtained from projection of the three dimensional data manifold collected for the 3-D object on the x_o, y_{on} plane associated with the n-th slice. An image for each slice can then be obtained as described before. An inherent assumption in this argument is that all slices are illuminated by the same plane wave. This is a reasonable approximation when the 3-D object is weakly scattering and the Born approximation is applicable or when the 3-D object is perfectly reflecting and does not give rise to multiple reflections between its parts. In the later case the two dimensional meriodnal slices D_n (ρ_{o_n}) deteriorate into contours, such as C in Fig. 1(b) defined by the intersection of the meridonal planes with the illuminated portion of the surface of the object.

Accordingly we can write for the n-th meridonal slice or contour,

$$\psi_n(k) = F \int D_n(\bar{\rho}_{o_n}) \; e^{-j\bar{p}.\bar{\rho}_{o_n}} \, d\bar{\rho}_{o_n} \tag{4}$$

We can regard $D_n(\bar{\rho}_{o_n})$ as the n-th meridonal slice or contour of a three dimensional object of reflectivity $U(\bar{r})$ where $\bar{r}$ is a three dimensional position vector in object space. This means that $D_n(\bar{\rho}_{o_n}) = U(\bar{r})\,\delta(z_{o_n})$ where δ is the Dirac delta "function". Consequently eq. (4) becomes,

$$\psi_n(k) = F \int U(\bar{r})\,\delta\,(z_{o_n})\, e^{-j\bar{p}.\bar{\rho}_{o_n}} \, d\bar{\rho}_{o_n}$$

$$= F \int U(\bar{r})\,\delta\,(z_{o_n})\, e^{-j\bar{p}.\bar{r}} \, d\bar{r} \tag{5}$$

where $d\bar{r}$ designates an element of volume in object space and where the last equation is obtained by virtue of the sifting property of the delta function.

Summing up the data from all slices or contours of the object we obtain,

$$\sum_n \psi_n = F \int U(\bar{r})\, e^{-j\bar{p}.\bar{r}} \, dr = \psi(\bar{p}) \tag{6}$$

because

$$\sum_n U(\bar{r})\,\delta\,(z_{o_n}) = U(\bar{r}).$$

Assuming that the Factor F in eq. (6) is eliminated as before by TDR or by other means, equation (6) reduces to

$$\psi(\bar{p}) = \int U(\bar{r})\, e^{-j\bar{p}.\bar{r}} \, d\bar{r} \tag{7}$$

The phase or range corrected data $\psi(\bar{p})$ obtained for example by the TDR method is therefore the 3-D Fourier transform of the object reflectivity $U(\bar{r})$. An alternate formulation to that given above of super-resolved wave-vector diversity e.m. imaging of 3-D

perfectly conducting objects is possible by extending Bojarski [3] and Lewis' [4] formulation of the inverse scattering problem to the bistatic case, along lines that are somewhat different than those given by Raz [5].

3. THE FOURIER DOMAIN PROJECTION THEOREMS

The preceeding discussion establishes the existence of a direct 3-D Fourier transform relationship between the object reflectivity $U(\bar{r})$ and the phase (or range) corrected $\bar{p}$ space data $\psi(\bar{p})$ collected by a coherent array of receivers forming an imaging aperture. Image retrieval from the 3-D data $\psi(\bar{p})$ can be carried out digitally using the fast Fourier transform. This requires digital data storage and processing. Due to the inherent two dimensionality of computer displays, the digitally reconstructed image can be presented to the viewer in cross-sections or in perspective. Direct coherent optical processing of the 3-D data $\psi(\bar{p})$ is not feasible because the coherent Fourier transforming property of the convergent lens is confined to 2-D input formats. A hybrid (opto-digital) approach based on the Fourier domain projection theorem can circumvent this difficulty. The motivations for utilization of optical methods are lower cost and high capacity for data storage together with a prospect for real-time operation and true three dimensional display.

The underlying principle for hybrid data processing is the Fourier domain projection theorem. Spatial domain and dual Fourier domain projection theorems have been utilized respectively in astronomy [8] and in x-ray crystallography and electron microscopy [9]. In this section we will review the Fourier domain projection theorem then explain its utilization in deriving 3-D image information from $\psi(\bar{p})$.

Let $\Psi(p)$ and $U(r)$ be three dimensional Fourier transform pairs i.e., rewriting eq. (7)

$$\psi(\bar{p}) = \int_v U(\bar{r}) e^{-j\bar{p}\cdot\bar{r}} d\bar{r} \tag{8}$$

where $\bar{r} = x_o\bar{1}_x + y_o\bar{1}_y + z_o\bar{1}_z$ and $\bar{p} = p_x\bar{1}_x + p_y\bar{1}_y + p_z\bar{1}_z$ are position vectors in object space and Fourier space respectively. In the volume integral (8) $d\bar{r}$ designates the element of volume $dx_o dy_o dz_o$ in object space.

The projection of $\psi(\bar{p})$ on the p_x-p_y plane is

$$\psi_{proj.}(p_x,p_y) = \int \psi(p_x,p_y,p_z,) dp_z \tag{9}$$

Substituting (8) in (9),

$$\psi_{proj.}(p_x,p_y) = \int_v U(x_o,y_o,z_o) \left(\int e^{-j(p_x x_o + p_y y_o + p_z z_o)} dp_z \right) dx_o dy_o dz_o \tag{10}$$

If the $\bar{p}$ space basis is sufficiently large the integration of the exponential e^{-jpz_o} with respect to p_z yields approximately $\delta(z_o)$ and equation (10) becomes,

$$\psi_{proj.}(p_x,p_y) = \int_v U(x_o,y_o,z_o)\delta(z_o)e^{-j(p_x x_o + p_y y_o)} dx_o dy_o dz_o$$

$$= \int_{x_o,y_o} \int D(x_o,y_o)e^{-j(p_x x_o + p_y y_o)} dx_o d_y.$$

$$= \int D(\bar{\rho}_o)e^{-j\bar{p}\cdot\bar{\rho}_o} d\bar{p}_o \tag{11}$$

where $D(x_o,y_o) = D(\bar{\rho}_o)$ is a the slice through the object $U(\bar{r})$ through the x_o,y_o plane.

Equation (11) indicates that the projection of the 3-D Fourier domain data on a given plane is the 2-D Fourier transform of the object central cross-section parallel to that plane. It follows from eq. (11) by the inverse transform,

$$D(x_o,y_o) = \int \psi_{proj.}(p_x,p_y)\, e^{\,j(p_x x_o + p_y y_o)}\, dp_x dp_y \tag{12}$$

which is the required theorem. According to this theorem, the projection of the 3-D transform data on any plane yields a 2-D data manifold from which a central cross-sectional outline of the illuminated portion of the object parallel to that plane can be obtained via a two dimensional Fourier transform which can be carried out optically. Photographic transparency records of the Fourier domain projections are suitable for use as input to an optical bench utilizing laser illumination to execute an instantaneous optical Fourier transform with the aid of a simple convergent lens. This leads to optical reconstruction of the corresponding cross-section of the object.

True 3-D image reconstruction is possible if one can view all projection holograms simultaneously. The most logical way to pro-

ceed in this regard is to combine all projection holograms into a single composite hologram which can reconstruct when viewed by an observor all cross-sectional outlines of the illuminated portion of the reflecting object simultaneously with correct angular ordering so that an impression of viewing a true 3-D image is created. One potential method of carrying this out is multiplex or integral holography [10].

Through the use of what we call *Weighted Fourier Projection Theorem* to be described next, it should be possible to reconstruct parallel slices of a 3-D object from the 3-D data manifold $\psi(\bar{p})$.

Let $G_\alpha(p_x,p_y)$ be the weighted projection of $\psi(\bar{p})$ defined by,

$$G_\alpha(p_x,p_y) = \int_{p_z} \psi(p_x,p_y,p_z)\, e^{j\alpha p_z}\, dp_z \tag{13}$$

Substituting for ψ from eq. (8) yields,

$$G_\alpha(p_x,p_y) = \int_{p_z} e^{j\,\alpha p_z} \int_{x_o,y_o,z_o} U(x_o,y_o,z_o)$$

$$e^{-j(p_x x_o + p_y y_o + p_z z_o)}\, dx_o dy_o dz_o dp_z \tag{14}$$

Carrying out the integration with respect to p_z first assuming the extent of the $\bar{p}$ space data to be sufficiently large, the integral with respect to P_z may be approximated by $\delta(z_o-\alpha)$ Equation (14) can be reduced then to,

$$G_\alpha(p_x,p_y) = \int_{x_o}\int_{y_o} U(x_o,y_o,z_o=\alpha)e^{-j(p_x x_o + p_y y_o)}\, dx_o dy_o \tag{15}$$

which says that $G_\alpha(p_x,p_y)$ and $U(x_o,y_o,z_o=\alpha)$ are two dimensional Fourier transform pairs. The weighted Fourier domain projection theorem follows from the inverse transform

$$U(x_o,y_o,z_o=\alpha) = \int_{p_x}\int_{p_y} G\,(p_x,p_y)e^{j(p_x x_o + p_y y_o)} dp_x dp_y \tag{16}$$

Accordingly parallel slices of the object can be reconstructed slice by slice by changing the parameter α.

In practice one expects that digital storage of the corrected 3-D data manifold $\psi(\bar{p})$ produced by a thinned receiver array is more convenient than optical storage. The projections $\psi_{proj}\ (p_x,p_y)$ and the weighted projections $G_\alpha(p_x,p_y)$ can therefore be carried out digitally. Two dimensional Fourier transform of these projections carried out either digitally or optically (and hence the hybrid nature) permits recovery of the 3-D image information slice by slice.

4. COMPUTER SIMULATION

Computer simulation of wave-vector diversity imaging of two 1m diameter perfectly reflecting spheres was undertaken to verify the method. The simulated geometry is shown in Fig. 2(a) where a circular array of 50 coherent receivers is assumed to be in the far field region of the object. The choice of the object was influenced by the ready availability in the literature of series formula for the field scattered from a perfectly reflecting sphere under plane wave illumination (12). The direction of illumination was assumed to be fixed. Wave-vector diversity was realized by sweeping the illumination wavelength between 7.5 cm and 15 cm (i.e. case of frequency swept imaging). The corrected (TDR) data $\psi(\bar{p})$ collected by the elements of the receiver array was stored in the computer in the proper format specified by the values of $\bar{p} = k\ (\bar{l}_{k_i} - \bar{l}_R)$ assumed for each receiver. The projection of the stored $\psi(\bar{p})$ on the plane of the array was displayed on the computer CRT display and photographed to yield the projection hologram shown in Fig. 2(b). The corresponding optically retrieved image is shown in Fig. 2(c). A central cross-sectional outline image of the two spheres that is parallel to the projection plane is clearly delineated as two adjacent circles of equal diameter as predicted by theory.

To evaluate the feasibility of reconstruction by parallel slices, the weighted Fourier domain projection theorem was applied to the stored data $\psi(\bar{p})$ for the preceeding example.

Preliminary photographs for the images retrieved from weighted projections for values of α equal to zero cm (central slice as in Fig. 2(c)), 30 cm and 40 cm are shown in Fig. 3. Although the quality of these preliminary images is not good they clearly illustrate the ability to reconstruct in parallel slices by means of the weighted Fourier domain projection theorem.

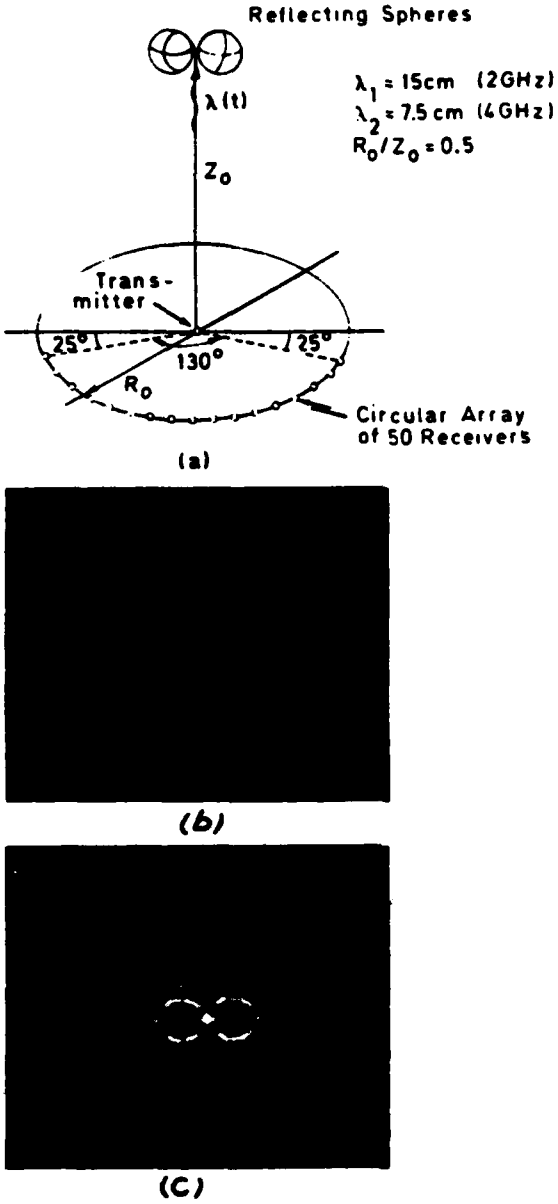

Fig. 2. Computer Simulation of Wave-vector Diversity Imaging, (a) Geometry, (b) Projection Hologram, (c) Retrieved Central Cross-sectional Image.

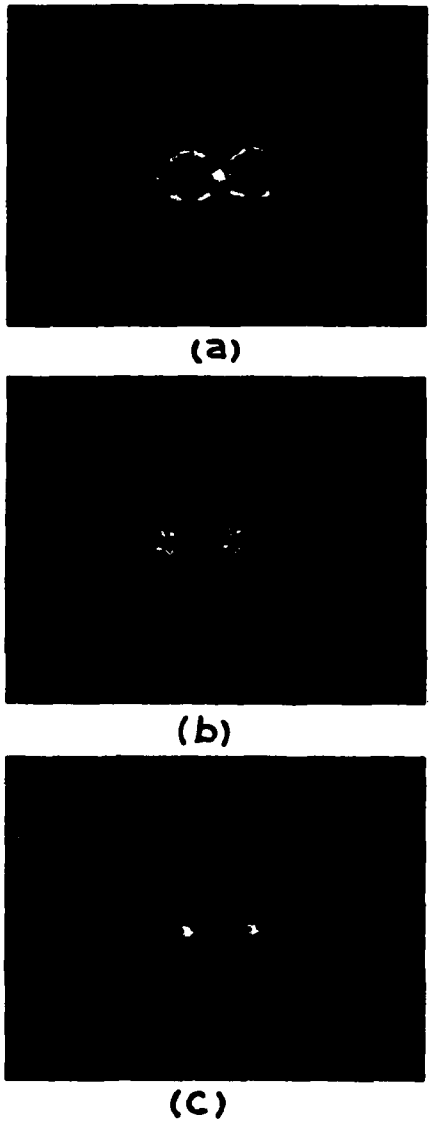

Fig. 3. 3-D Image Retrieval by Parallel Slices for Values of α = 0 cm (a), 30 cm (b) and 40 cm (c).

5. CONCLUSIONS

We have presented the principles of a long-wave imaging method in which wave-vector diversity, or frequency diversity (when the direction of object illumination is fixed), is employed to enhance the amount of object information captured by a broad-band coherent receiving array deployed in the far field of the object. The main features of the method whose basic principles have also been verified by computer simulation are:

(a) the data collected by a thinned coherent array of receivers intercepting the wavefield scattered from a distant 3-D reflecting object, as the frequency of its illumination and/or its direction of incidence is changed, can be stored as a 3-D data manifold in $\underline{p}$ space from which an image of the object can be retrieved by means of a 3-D Fourier Transform. The size and shape of the 3-D data manifold, and therefore the resolution, depend on the relative position of the object the transmitter (illuminator) and the receiving array and on the spectral width of the illumination utilized.

(b) the data collected must be corrected for a quadratic phase term before it is stored in a 3-D manifold and an undistorted image of the 3-D reflecting object reconstructed through the 3-D Fourier transform operation. A bothersome range-azimuth ambiguity is also avoided through elimination of this quadratic phase term.

(c) one method of achieving this correction is through the use of a TDR (Target Derived Reference) by means of which the object or target is made to act as a point scatterer by illuminating it with a sufficiently low frequency signal that is a subharmonic of the imaging frequencies utilized. Harmonic mixing of the amplified and limited signals produced by the reference spherical wavefront generated by the object at the receiving array elements with those produced by the imaging wavefronts scattered from the object should in principle yield the required phase corrected data. The use of a TDR has many additional advantages.

These include:

(i) Elimination of the need for a central local oscillator for the coherent receiving array.

(ii) Because the target derived reference source moves with the target there is greater tolerance to target motion during data acquisition.

(iii) Because TDR results in a recording configuration similar to that of a lensless Fourier Transform hologram, the resolution requirements from the recording device are greatly

relaxed. In longwave holography this fact is translated into a significant reduction of the number of receiving elements in the recording aperture. In addition the use of TDR allows us to place all the resolving power of the recording aperture on the target. This means that high resolution images of distant isolated targets should be feasible with array apertures consisting of tens of elements. The ability to synthesize a 2-D receiving aperture with a Wells array (11) consisting of two orthogonal linear arrays one of transmitters and the other of receivers provides further means of reducing the number of stations needed for data acquisition without sacrifice in resolution.

(iv) Greater immunity to phase fluctuations arising from turbulance and inhomogenieties in the propagation medium because both the reference and imaging signals arriving at each receiving element of the aperture travel roughly over the same path.

(v) TDR eliminates the range azimuth ambiguity and excessive bandwidth problems that arise in frequency swept imaging when the reference signal for the array aperture is derived instead from the illumination source or a centrally located local oscillator phase locked to it.

(d) Because the dimensions of the 3-D data manifold $\psi(\bar{p})$ in $\bar{p}$ space are dependent, in addition to geometry, on the spectral range of the illumination, super-resolution (i.e. resolution beyond the classical limit of the available physical aperture) is achieved. This aperture synthesis by wave-vector or frequency diversity helps cut down array cost (since a thinned array can be used) and size.

(e) Fourier domain projection theorems enable the generation of two dimensional holograms from projections (or weighted projections) of the corrected 3-D data manifold $\psi(\bar{p})$ permitting thereby optical image retrieval of the 3-D object in meridonal slices parallel to the projection planes one at a time (or in parallel slices one at a time).

(f) True 3-D image presentation could be possible by combining a set of distinct projection holograms, using multiplex or integral holography techniques, into a single composite hologram which can reconstruct all corresponding cross-sectional outlines of the illuminated portion of the object simultaneously yielding thus a viewable true-3D image.

(g) Unlike conventional Longwave holography no wavelength scaling is required here to avoid longitudinal distortion in optical reconstruction.

(h) Because of the broad-band nature of the illumination and

the aperture synthesis by frequency diversity, reduction of speckle noise in the image is expected.

(i) In the Frequency Swept mode of wave-vector diversity imaging (i.e. when $\bar{l}_{k_i}$ = const.), the collected data at each receiver represents a frequency response of the object. Assuming the scattering process is linear, this frequency response is related to the impulse response of the object by a Fourier transform (2), (13). This suggests that when impulse illumination is utilized, instead of frequency swept illumination, a 3-D data manifold $\psi(\bar{p})$ may be generated by Fourier transforming the impulse response at each receiver, correcting the data for the Factor F, and storing the result in accordance to the corresponding $\bar{p}$ for each receiver. The resulting corrected $\psi(\bar{p})$ can then be employed as described in this paper to yield 3-D image information. Impulse illumination is desirable in certain instances of rapid target motion but may be more difficult to implement than frequency swept illumination.

It is difficult to conclude without noting some extremely interesting similarities between wave-vector diversity (or frequency diversity) imaging discussed here and certain features of the sonar system in mammals such as bottle-nosed Dolphins, whales and bats. These features have been deduced or hypothesized by several workers (14)-(17) from observations of the remarkable acoustical behaviour, activity during echo-location, and anatomical studies of these mammals especially the Dolphin. Some of the more pertinent features which we only list here are:

(a) All signals emitted are of broad-band nature. They are either in the form of relatively long chirps (whistles), impulse like pings or clicks of less than 1msec duration and frequency content extending up to 100 kHz, or low frequency barks rich in higher harmonics.

(b) Ability to detect signals buried in noise indicating possible coherent or corellation processing.

(c) Evidence of the presence of a sensor array in the melon surface with sensitivity in the 15-100 kHz which might be utilized for reception of acoustic echos in addition to sensing velocity and temperature. The lens-shaped fatty body of the mellon, which is essentially acoustically transparent, might also be utilized as a variable focus acoustic lens for focusing of emitted sound on selected targets.

(d) Evidence of super-resolution capabilities i.e., resolution exceeding the classical limit of any possible available physical recording aperture, such as the melon even when assumed to be operating at the higher frequency range of sound emissions.

6. ACKNOWLEDGMENTS

This work was sponsored in part by the Army Research Office - Durham under Grant No. DAAG29-76-G-0230 and by Air Force Office of Scientific Research, Air Force Systems Command, USAF under Grant No. AFSOR-77-3256A.

REFERENCES

1. N.H. Farhat, "Frequency Synthesized Imaging Apertures," Proc. 1976 Optical Computing Conference, IEEE Cat. No. 76CH1100-7C, pp. 19-24.

2. N.H. Farhat, "Principles of Broad-band Coherent Imaging", J. Opt. Soc. Am., Vol. 67, Aug. 1977, pp. 1015-1021.

3. R.P. Porter, "A Radar Imaging System Using the Object to Provide the Reference Signal", Proc. IEEE (letters), Vol. 59, February, 1971, pp. 307-308.

4. N. Farhat, "Reply to Comments on Computer Simulation of Frequency Swept Imaging", Proc. IEEE (letters), Vol. 65, pp. 1223-1224, Aug. 1977.

5. N.N. Bojarski, "Inverse Scattering", Final Report to Contract B00019-73-C-0316 Naval Air Syst. Command, February 1974.

6. R.M. Lewis, "Physical Optics Inverse Diffraction", IEEE Trans. on Ant. and Prop., Vol. AP-17, May 1969, pp. 308-314.

7. S. Rosenbaum-Raz, "On Scatterer Reconstruction from Far-Field Data", IEEE Trans, on Ant. and Prop., Vol. AP-24, January 1976, pp. 66-70.

8. R.N. Bracewell and S.J. Wernecke, "Image Reconstruction Over a Finite Field of View", J. Opt. Soc. Am., Vol. 65, November 1975, pp. 1342-1346. See Also: R.N. Bracewell, "Strip Integration in Radio Astronomy", Australian J. Phys. Vol. 9, 1956, pp. 198-217.

9. G.W. Stroke and Maurice Halioua, "Three-Dimensional Reconstruction in X-Ray Crytallography and Electron Microscopy By Reduction to Two-Dimensional Holographic Implementation", Trans. Amer. Crytallographic Assoc., Vol. 12, 1976, pp. 27-41.

10. D.L. Vickers, "The Integral Hologram as a Scientific Tool", Lawrence Livermore Laboratory Report UCID-17035, February, 1976, See Also: "White-Light Holographic Displays", Laser Focus, Vol. 13, July 1977.

11. W.H. Wells, "Acoustical Imaging with Linear Transducer Arrays", in Acoustical Holography, Vol. 2, A.F. Metherell and L. Larmore (Eds.), Plenum Press, New York, 1970. Also See: C.N. Nilsen and D.N. Swingler, "Quasi-Real-Time Inertialess Microwave Holography", Proc. IEEE (letters), Vol. 65, March 1977, pp. 491-492.

12. R.F. Harrington, Time Harmonic Electromagnetic Fields, McGraw Hill, New York, 1961, pp. 292-298.

13. E.M. Kennaugh and L. Moffatt, "Transient and Impulse Response Approximations", Proc. IEEE, Vol. 53, August 1965, pp. 893-901.

14. J. Cunningham Lilly, The Mind of the Dolphin, Avon Books, New York, 1967.

15. J.J. Dreher, "Acoustical Holographic Model of Cetacean Echo-Location", in Acoustical Holography, Vol. 1., A.F. Metherell, H.M.A. El-Sum and L. Larmore (Eds.), Plenum Press, New York, 1969, pp. 127-137.

16. W.N. Kellogg, "Auditory Perception of Submerged Objects by Porpoises", J. Acoust. Soc. Am., Vol. 31, January 1959, pp. 1-6.

17. W.E. Evans and J.H. Prescott, "Observations of the Sound Production Capabilities of the Bottlenose Porpoise: A Study of Whistles and Clicks", Zoologica, Vol. 47, 1962, pp. 121-128.

APPENDIX II

HOLOGRAPHY, WAVE-LENGTH DIVERSITY AND INVERSE SCATTERING

(Paper published in *Optics in Four Dimensions*, M.A. Machado and L.M. Narducci (Eds.), Am. Inst. of Phys., New York, 1981)

Published in Optics in Four Dimensions.
M.A. Machado and L. M. Narducci (Eds.). Am. Inst. of Physics., NY 1981

HOLOGRAPHY, WAVE-LENGTH DIVERSITY AND INVERSE SCATTERING

N.H. FARHAT
University of Pennsylvania
The Moore School Graduate Research Center
Philadelphia, PA 19104

ABSTRACT

The use of wavelength diversity to enhance the performance of thinned coherent imaging apertures is discussed. It is shown that wavelength diversity lensless Fourier transform recording arrangements that utilize a reference point source in the vicinity of the object can be used to access the three-dimensional Fourier space of non-dispersive perfectly reflecting or weakly scattering objects. Hybrid (opto-digital) computing applied to the acquired 3-D Fourier space data is shown to yield tomographic reconstruction of 3-D image detail either in parallel or meridional (central) slices. Because of an inherent ability of converting spectral degrees of freedom into spatial 3-D image detail true super-resolution is achieved together with suppression of coherent noise. The similarity of our key equations to those of inverse scattering theory is pointed out and the feasibility of using other forms of broadband radiation such as impulsive, noise and thermal is discussed. Finally, the possibility of utilizing wavelength diversity imaging in microscopy and telescopy is discussed.

INTRODUCTION

A frequently encountered question in the science of image formation is how to make an available aperture collect more information about the scene or object being imaged in order to enhance its resolving power beyond the classical Rayleigh limit. This process is known as super-resolution and is relevant to all imaging systems whether holographic or conventional. There are five known methods for achieving super-resolution. These include: weighting or apodization of the aperture data[1,2]; analytic continuation of the wavefield measured over the aperture[3,4]; use of evanescent wave illumination[5]; maximum entropy method[6]; and use of the time channel[7]. Weighting and analytical continuation techniques are known to become rapidly ineffective as the signal to noise ratio of the collected data decreases. Maximum entropy techniques are known to be more robust, as far as noise is concerned but involve usually extensive computation. Illumination with evanescent waves is practical in limited situations where full control of the recording arrangement exists as in microscopy, for example.

This leaves the time channel approach in which one can collect in time more information about the object through the available recording aperture by altering the object aspect relative to the aperture by means of rotation or linear motion[8,9,28] or by altering the parameters of the illumination such as directions of incidence, wavelength and/or polarization as discussed in this paper. These latter operations are known to increase the degrees of freedom of the wavefields impinging on the recording aperture enhancing thereby their ability to convey information about the nature of the scattering object. Sophisticated imaging systems endeavor to convert the nonspatial degrees of freedom of the wavefield, e.g., angular, spectral and polarization to spatial image detail, enhancing thereby the resolution capability beyond the classical Rayleigh limit of the available physical aperture. Obviously such procedures involve more signal processing than that performed by conventional imaging with lens systems or holography.

In this paper we consider generalizing the holographic concept to include wavelength diversity as a means of enhancing resolution. A quick examination of the basic equations of holography reveals that the lensless Fourier transform hologram recording arrangement is amenable to this generalization. This conclusion is used then as a starting point for a Fourier optics formulation of wavelength diversity imaging of 3-D (three dimensional) nondispersive objects. The results show that measurement of the multiaspect or multistatic frequency (or wavelength) response of the 3-D object permits accessing its 3-D Fourier space. The resulting formulas are identical to those obtained from a multistatic generalization of inverse scattering[10,11,12] establishing thus a clear connection between holography and the inverse scattering imaging problem. The inclusion of wavelength diversity in holography is shown to have several important features: (a) the availability of the 3-D Fourier space data permits 3-D image retrieval tomographically in parallel or meridional (central) slices or cross-sectional outlines by the application of Fourier domain projection theorems; (b) suppression of coherent noise and speckle in the retrieved image; (c) removal of several longstanding constraints on longwave (microwave and acoustical) holography such as the impractically high cost of the apertures needed, the inability to view a true 3-D image as in optical holography because of a wavelength scaling problem, and minimization of the effects of resonances on the object.

WAVELENGTH DIVERSITY

We start by inquiring into the conditions under which the data from N holograms of the same nondispersive object recorded over the same aperture, each at a different wavelength, can be combined to yield a single image superior in quality to the image retrieved from any of the individual holograms.

One approach to answering the question posed above would be to determine the conditions under which the well known formulas[13] for the focusing condition, magnification and image location in holography can be made independent of wavelength. This quickly leads to the conclusion that wavelength independence can be met if a reference point source centered on the object is used and proper scaling of the individual holograms by the ratio of recording to the reconstruction wavelength is performed before superposition [15,24]. The former condition is required for recording a lensless Fourier transform hologram[14,29], where the presence of the reference point source in the object plane leads to the recording of a Fraunhofer diffraction pattern of the object rather than its Fresnel diffraction pattern because of the elimination in the recorded hologram of a quadratic phase term in the object wavefield. This is known to result in a highly desirable reduction in the resolution required from the hologram recording medium and is therefore of practical importance especially in nonoptical holography. More detail of the processing involved in combining the data in multi-wavelength hologram can be found elsewhere[15].

Additional insight into the process of attaining super-resolution by wavelength diversity is obtained by considering the concept of wavelength or frequency synthesized aperture [16-20]. The synthesis of a one dimensional aperture by wavelength diversity is based on the simple fact that the Fraunhofer or far field diffraction pattern of a nondispersive planar object changes its scale, i.e. it "breathes", but does not change its shape (functional dependence), as the wavelength is changed. A stationary array of broadband sensors capable of measuring the complex field variations deployed in this breathing diffraction pattern at suitably chosen locations would sense different parts of the diffraction pattern as the wavelength is altered, this allows collecting more information on the nature of the diffraction pattern, and therefore on the object that gave rise to it than if the wavelength was fixed (stationary diffraction pattern). Each stationary sensor in the array is thus able to collect, as the wavelength is changed, and the breathing diffraction pattern sweeps over it, the same set of data or information collected by mechanically scanning a sensor over the diffraction pattern when it is kept stationary by fixing the wavelength. Hence the term wavelength or frequency synthesized aperture.

The orientation and location of the wavelength synthesized aperture for any planar distribution of sensors deployed in the Fraunhofer diffraction pattern of a planar object and the retrieval of an image from the collected data has been treated earlier[16,17]. It was clear, however, that extension of the wavelength diversity concept to the case of 3-D objects is necessary before its generality and practical use could be established.

For this purpose we considered[20] as shown in Fig. 1(a) an isolated planar object of finite extent with reflectivity $D(\bar{\rho}_o)$, where $\bar{\rho}_o$ is a two dimensional position vector in the object plane (x_o, y_o). The object is illuminated by a coherent plane wave of unit-amplitude and of wave vector $\bar{k}_i = k\,\bar{I}_{k_i}$ produced for example by a distant source located at $\bar{R}_T$. The wavefield scattered by the object is monitored at a receiving point designated by the position vector $\bar{R}_R$ belonging to a recording aperture lying in the far field region of the object. The receiving point will henceforth be referred to as the receiver and the source point at the transmitter. The position vectors $\bar{\rho}_o$, $\bar{R}_T$ and $\bar{R}_R$ are measured from the origin of a cartesian coordinate system (x_o, y_o, z_o) centered in the object. The object is assumed to be nondispersive i.e., D is independent of k. However, when the object is dispersive such that $D(\bar{\rho}_o, k) = D_1(\bar{\rho}_1)D_2(k)$ and $D_2(k)$ is known, the analysis presented here can easily be modified to account for such object dispersion by correcting the collected data for $D_2(k)$ as k is varied.

Referring to Figure 1(a) and ignoring polarization effects, the field amplitude at $\bar{R}_R$ caused by the object scattered wavefield may be expressed as,

$$\psi(k,\bar{R}_R) = \frac{jk}{2\pi} \int D(\bar{\rho}_o) e^{-j\bar{k}_i \cdot \bar{r}_T} \frac{e^{-jk\, r_R}}{r_R} d\bar{\rho}_o \qquad (1)$$

where $d\bar{\rho}_o$ is an abbreviation for $dx_o dy_o$ and the integration is carried out over the extent of the object. Noting that $\bar{r}_T = \bar{\rho}_o - \bar{R}_T$, $\bar{R}_T = -R_T \bar{I}_{k_i}$ and using the usual approximations valid here: $r_R \simeq R_R + \rho_o^2/2R_R - \bar{I}_R \cdot \bar{\rho}_o$ for the exponential in (1) and $r_R \simeq R_R$ for the denominator in (1) where $\bar{I}_R = \bar{R}_R/R_R$ and $\bar{I}_{k_i} = \bar{k}_i/k$ are unit vectors in the $\bar{R}_R$ and $\bar{k}_i$ directions respectively, one can write eq. (1) as,

$$\psi(k, \bar{R}_R) = \frac{jk}{2\pi R_R} e^{-jk(R_T + R_R)} \int D(\bar{\rho}_o)\, e^{-j\,\bar{p} \cdot \bar{\rho}_o} d\bar{\rho}_o, \qquad (2)$$

In eq. (2) we have used the fact that the observation point is in the far field of the object, so that $\exp(-jk\,\rho_o^2/2R_R)$ under the integral sign can be replaced by unity. In addition, $\bar{p} = k\,(\bar{I}_{k_i} - \bar{I}_R) \triangleq p_x \bar{I}_x + p_y \bar{I}_y + p_z \bar{I}_z$ is a three dimensional vector whose length and orientation depend

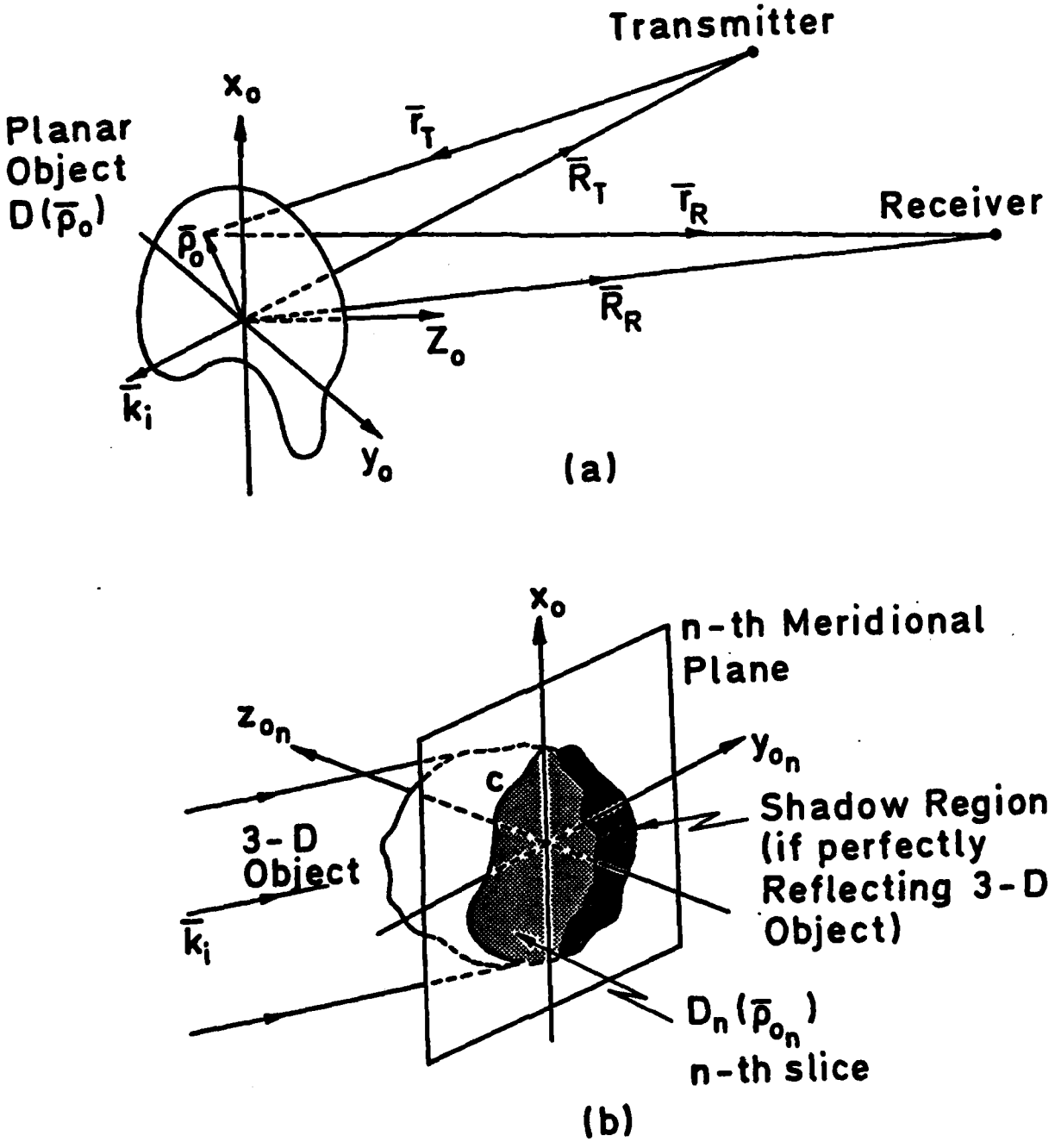

Fig. 1. Geometries for wavelength diversity imaging. (a) Two dimensional object, (b) Three dimensional object with the n-th meridional (central) slice and cross sectional outline c shown.

on the wavenumber k and the angular positions of the transmitter and the receiver. For each receiver and/or transmitter present, $\bar{\rho}$ indicates the position vector for data storage. An array of receivers for example would yield therefore a 3-D data manifold as k is varied (frequency diversity) or as $\bar{k}$ $(=k\bar{I}_{k_i})$ is varied (wave-vector diversity) The projection of this 3-D data manifold on the object plane yields $\psi(k,R_T)$ because $\bar{\rho} \cdot \bar{\rho}_o = \bar{\rho}_t \cdot \bar{\rho}_o = p_x x_o + p_y y_o$ where $p_x = k(\bar{I}_{k_i} - \bar{I}_R)_x$ and $p_y = k(\bar{I}_{k_i} - \bar{I}_R)_y$ are the cartesian components of the projection $\bar{\rho}_t$ of $\bar{\rho}$ on the object plane. Accordingly eq. (2) can be expressed as,

$$\psi(k, R_R) = \frac{jk}{2\pi R_R} e^{-jk(R_T + R_R)} \int D(x_o,y_o) e^{-j(p_x x_o + p_y y_o)} dx_o dy_o \quad (3)$$

Because of the finite extent of the object, the limits on the integral can be extended to infinity without altering the result. The integral in (3) is recognized then as the two dimensional Fourier transform $\tilde{D}(p_x,p_y)$ of $D(x_o,y_o)$. It is seen to be dependent on the object reflectivity function, the angular positions of the transmitter and the receiver and on the values assumed by the wavenumber k but is entirely independent of range. Information about D can thus be collected by varying these parameters. Note that the range information is contained solely in the factor $F = jk \exp[-jk(R_T + R_R)]/2\pi R_R$ preceeding the integral. The field observed at $\bar{R}_R$ has thus been separated into two factors one of which, the integral, $\tilde{D}$, contains the lateral object information and the other F, contains the range information. The presence of F in eq. (3) hinders the imaging process since it complicates data acquisition and if not removed, gives rise to image distortion because R_R is generally not the same for all receivers. To retrieve an image of the object via a 2-D Fourier transform of eq. (3), the factor F must first be eliminated. Holographic recording of the complex field amplitude given in (3) using a reference point source located at the center of the object will result in the elimination of the factor F and the recording of a Fourier transform hologram. This operation yields $\tilde{D}$ over a two dimensional region in the p_x,p_y plane. The size of this region, which determines the resolution of the retrieved image depends on the angular positions of the transmitter and the receiver and on the values assumed by k, i.e. the extent of the spectral window used. The latter dependence on k implies super-resolution imaging capability because of the frequency synthesized dimension of the 2-D data manifold that is generated. Because of the dependence of resolution on the relative positions of the object, the transmitter, and receiving aperture, the impulse response is clearly not invariant. In fact a receiver point situated at $\bar{R}_R$ for which $\bar{\rho}$ is normal to the object

plane can not collect any lateral object information because for this condition ($\bar{p} \cdot \bar{\rho}_o = 0$) the integrals in (2) and (3) yield a constant. Such receiving point is located in the direction of specular reflection from the object where the diffraction pattern is stationary i.e. does not change with k. In this case the observed field is solely proportional to F containing thus range information only. Obviously this case can easily be avoided through the use of more than one receiver which is required anyway when 2-D or 3-D object resolution is sought[20,21].

The analysis presented above can be extended to three dimensional objects by viewing a 3-D object as a collection of thin meridional or central slices as depicted in Fig. 1(b) each of which representing a two dimensional object of the type analyzed above. With the n-th slice we associate a cartesian coordinate system x_o, y_{o_n}, z_{o_n} that differs from other slices by rotation about the common x_o axis. Since the vectors $\bar{p}$, $\bar{R}_T$ and $\bar{R}_R$ are the same in all n-coordinate systems, eq. (3) holds. $\psi_n(k,\bar{R}_R)$ is then obtained from projection of the three dimensional data manifold collected for the 3-D object on the x_o, y_{on} plane associated with the n-th slice. An image for each slice can then be obtained as described before. An inherent assumption in this argument is that all slices are illuminated by the same plane wave. This is a reasonable approximation when the 3-D object is a weak scatterer and the Born approximation is applicable, or when the 3-D object is perfectly reflecting and does not give rise to multiple reflections between its parts. In the latter case the two dimensional meridional slices $D_n(\bar{\rho}_{o_n})$ deteriorate into contours, such as C in Fig. 1(b) defined by the intersection of the meridonal planes with the illuminated portion of the surface of the object. Accordingly we can write for the n-th meridional slice or contour,

$$\psi_n(k,R_R) = F \int D_n(\bar{\rho}_{o_n})\, e^{-j\bar{p}\cdot\bar{\rho}_{o_n}}\, d\bar{\rho}_{o_n} \qquad (4)$$

We can regard $D_n(\bar{\rho}_{o_n})$ as the n-th meridional slice or contour or a three dimensional object of reflectivity $U(\bar{r})$ where $\bar{r}$ is a three dimensional position vector in object space. This means that $D_n(\bar{\rho}_{o_n}) = U(\bar{r})\ \delta(z_{o_n})$ where δ is the Dirac delta "function". Consequently eq. (4) becomes,

$$\psi_n(k,R_R) = F \int U(\bar{r})\, \delta(z_{o_n})\, e^{-j\bar{p}.\bar{\rho}_{o_n}}\, d\bar{\rho}_{o_n}$$

$$= F \int U(\bar{r})\, \delta(z_{o_n})\, e^{-j\bar{p}.\bar{r}}\, d\bar{r} \qquad (5)$$

where $d\bar{r}$ designates an element of volume in object space and where the last equation is obtained by virtue of the sifting property of the delta function.

After summing up the data from all slices or contours of the object we obtain,

$$\sum_n \psi_n = F \int U(\bar{r})\, e^{-j\bar{p}.\bar{r}}\, d\bar{r} = \psi(\bar{p}) \qquad (6)$$

because

$$\sum_n U(\bar{r})\, \delta(z_{o_n}) = U(\bar{r}).$$

On assuming that the Factor F in eq. (6) is eliminated as before, equation (6) reduces to

$$\psi(\bar{p}) = \int U(\bar{r})\, e^{-j\bar{p}.\bar{r}}\, d\bar{r} \qquad (7)$$

which is the 3-D Fourier transform of the object reflectivity $U(\bar{r})$. Thus, wavelength diversity allows one to access the 3-D Fourier space of a nondispersive object and provides the basis for 3-D Lensless Fourier transform holography. An alternate formulation of super-resolved wave-vector diversity imaging of 3-D perfectly conducting objects is possible[22] by extending the analysis of the inverse scattering imaging problem[10,11] to the multistatic case, along lines that are similar to but somewhat different from those given by Raz[12]. The resulting scalar formulas are identical to (7) thus establishing the connection between the holographic and the inverse scattering approaches to the imaging problem.

THREE DIMENSIONAL IMAGE RETRIEVAL

The above considerations of multiwavelength holography have provided a means by which the 3-D Fourier space of the object can be accessed by employing snychronous detection. It is clear that once the 3-D Fourier space data is available, 3-D image detail can be retrieved by means of an inverse 3-D Fourier transform that can be carried out digitally. Alternately, holographic techniques

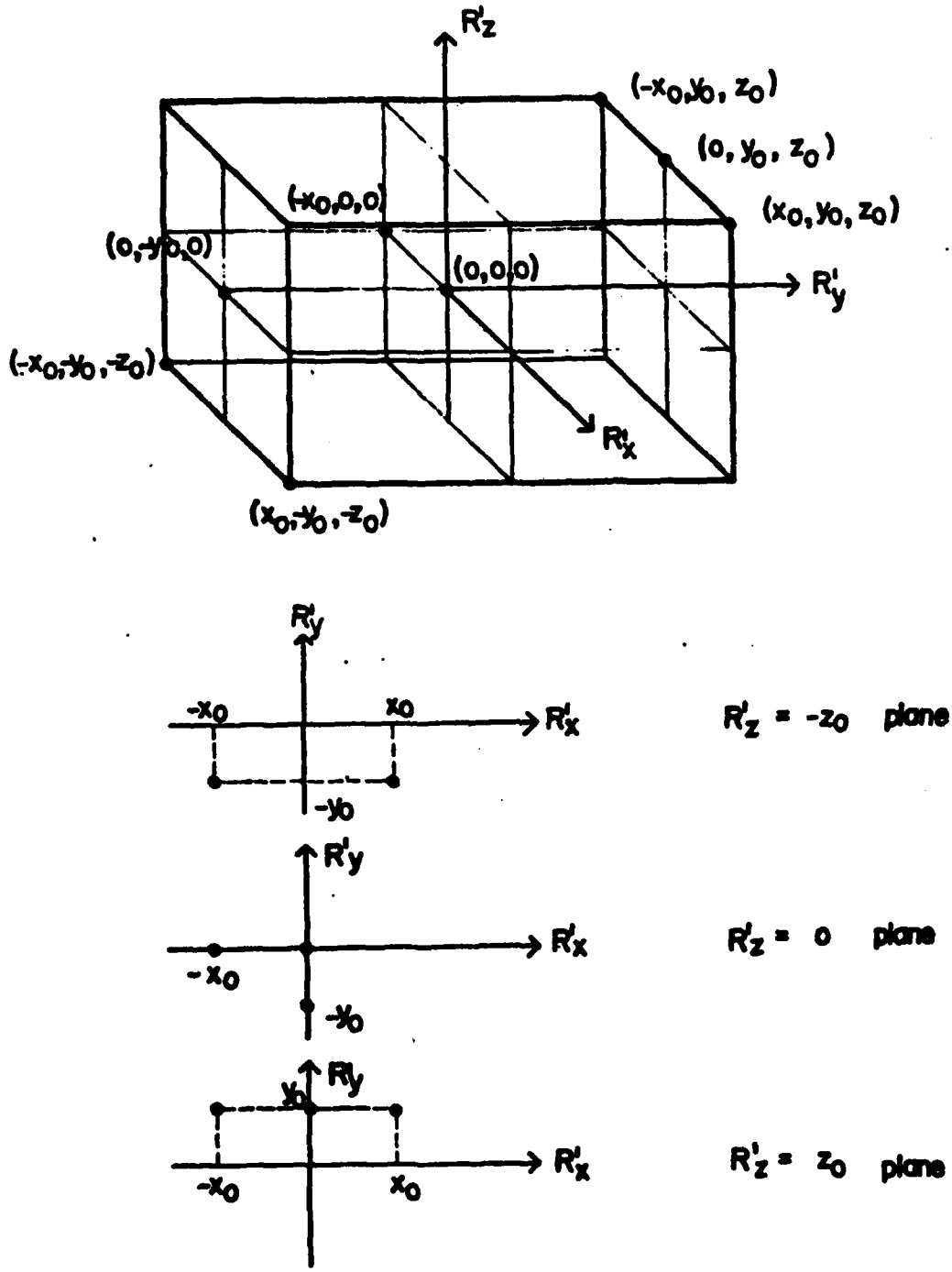

Fig. 2. 3-D object consisting of a set of eight point scatterers shown in isometric and R'_x-R'_y plane views at R'_z=$-z_0$,0,z_0. x_0=y_0=z_0 =100 cm.

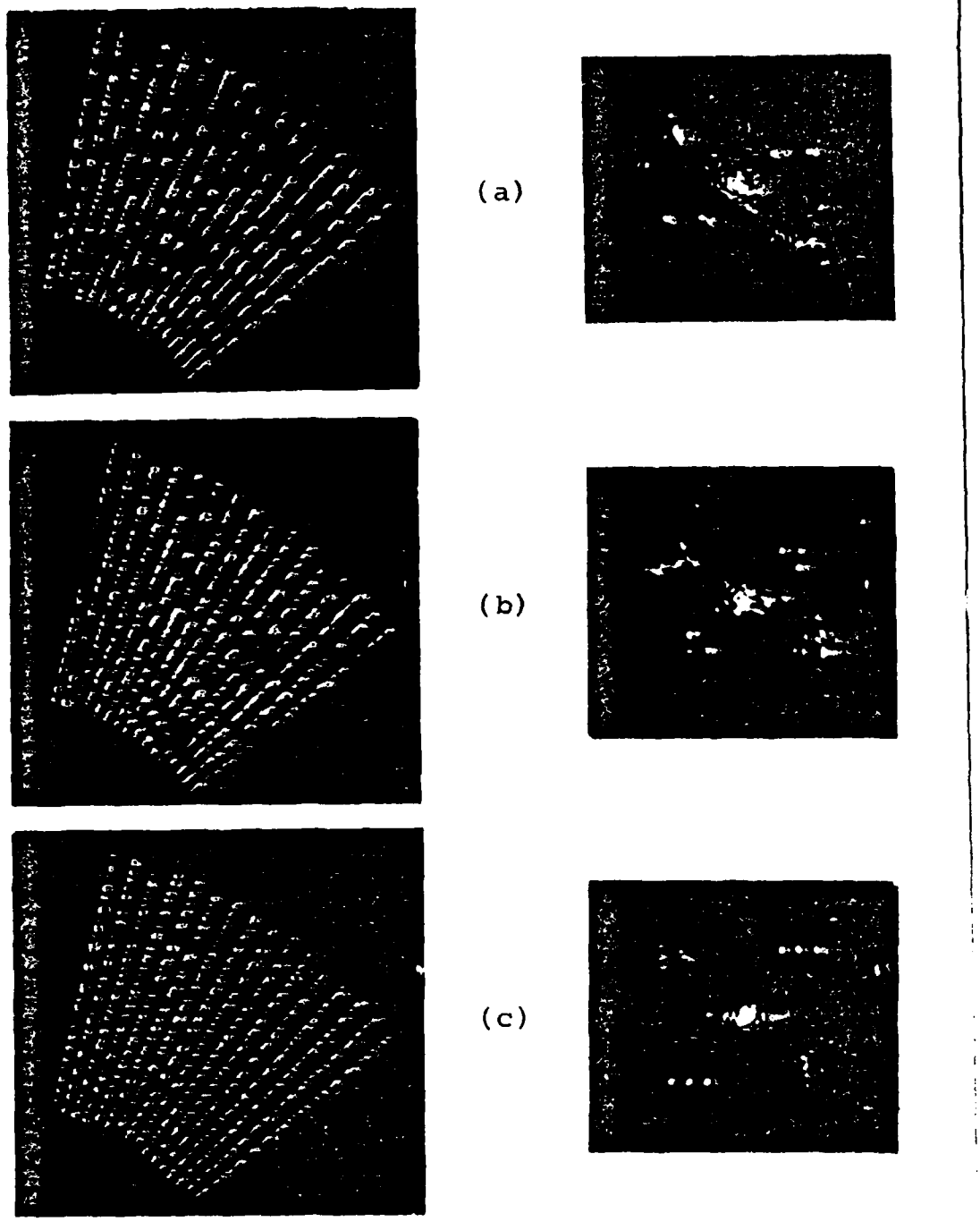

Fig. 3. Projection holograms and their optical reconstructions for the set of point scatterers in Fig. 2 at different R'_z planes. (a) Hologram and reconstructed image of scatterers at $R'_z=-z_o$ plane. (b) Hologram and image at $R'_z=0$ plane. (c) Hologram and image at $R'_z=z_o$ plane. $x_o=y_o=z_o=100$ cm.

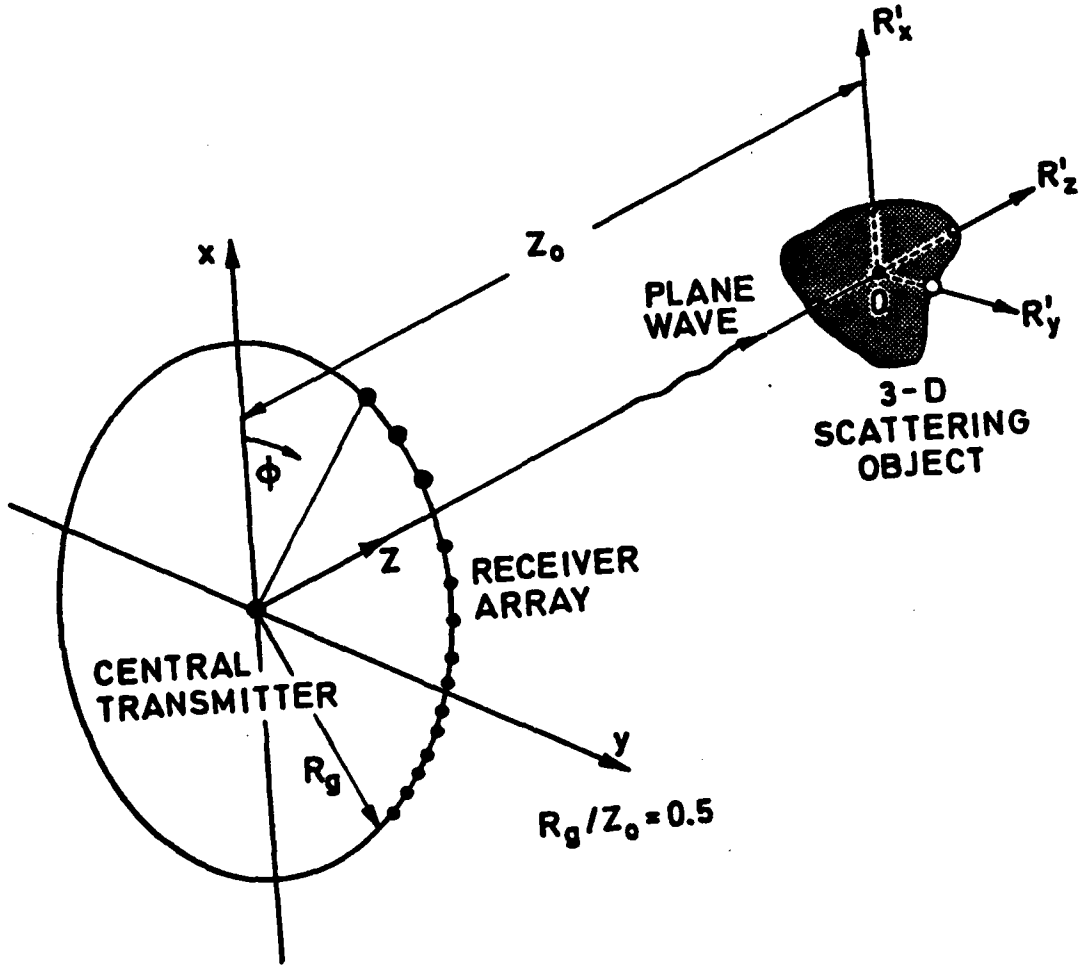

Fig. 4. Arrangement used in computer simulation of wavelength diversity imaging.

can be invoked again. Fourier domain projection theorems[23] that are dual to the spatial domain projection theorem[25,26] can be applied to the Fourier space data to produce a series of projection holograms from which 2-D images of meridional or parallel slices of the object can be retrieved on the optical bench[20]. This procedure does not involve any specific scaling of the size of the optical hologram transparency relative to the size of the original recording aperture by the ratio of the recording to the reconstruction wavelengths as in longwave holography there the scaling necessary for viewing a 3-D image free of longitudinal distortion ususally leads to an impractically minute equivalent hologram transparancy that cannot be readily viewed by an observer. The lateral and longitudinal resolutions in the retrieved image depend now on the dimensions of the volume in Fourier space accessed by wavelength diversity. This volume depends, in turn, on the wavelength range and on the recording geometry. Thus the longitudinal resolution does not deteriorate as rapidly with range as in conventional monochromatic imaging systems.

An example of computer simulations of frequency diversity holographic imaging of a 3-D object consisting of eight point scatterers distributed as shown in Fig. 2 is given in Fig. 3. Shown in Fig. 3 are three weighted Fourier domain projection holograms and the corresponding optically retrieved images for three equally spaced parallel slices of the object containing distinguishable 2-D distributions of scatterers. The simulated recording arrangement shown in Fig. 4 consisted of an array of 16 receivers equally distributed on an arc extending from $\phi = 40^{o}$ to $\phi = 77.5^{o}$ surrounding a central transmitter capable of providing plane wave illumination of the object. The results shown were obtained with microwave imaging in mind assuming a frequency sweep of (2-4)GHz. They clearly indicate a lateral and longitudinal resolution capability of the order of 25 cm. Wider sweep widths yield better resolution. For example a (1-18)GHz sweep would yield a 3-D resolution of the order of 1.5 cm.

DISCUSSION AND CONCLUSIONS

Seeking means by which the information content in a hologram can be increased, for example by wavelength diversity, we have arrived at a formulation of 3-D Lensless Fourier transform holography capable of furnishing 3-D image detail tomographically. This ability of producing 3-D images in slices from coherently detected wavefields enables us to regard the method also as coherent tomography. The Fourier space accessed in the above fashion by wavelength diversity can be viewed as a generalized 3-D hologram in which one dimension has been synthesized by wavelength diversity. Such a generalized hologram contains not only spatial amplitude and phase data as in conventional holography, but also spectral information. Consequently, it can yield better

resolution than the classical Rayleigh limit of the available aperture operating at the shortest wavelength of the spectral window used. This super-resolving property is further enhanced through an inherent suppression of the effects of object resonances and speckle in the retrieved image; the latter property is a consequence of the fact that frequency diversity tends to make the impulse response of the system unipolar and to resemble that of a non-coherent imaging system that is free of speckle and coherent noise artifacts[15]. Further enhancement of information content and resolution can be achieved by polarization diversity where the $\bar{p}$ space can be multiply accessed for different nonredundant polarizations of the illumination and the receivers and the resulting polarization diversity images added either coherently or non-coherently in order to achieve a degree of noise averaging as discussed elsewhere[15].

The removal of several longstanding constraints on conventional longwave (microwave and acoustic) holography attained through the use of wavelength diversity as described here leads to a new class of imaging systems capable of converting spectral degrees of freedom into 3-D image detail, and thus of furnishing true super-resolution. Wavelength diversity is applicable to the imaging of two classes of objects: perfectly reflecting objects of the type encountered in radar and sonar, and weakly scattering objects of low or known dispersion of the type encountered in biology and medicine. The practical application of the concepts presented here to optical wavefields is presently under consideration. The availability of tunable dye lasers and electronic imaging devices suggest interesting possibilities of three dimensional wavelength diversity microscopy. Here one can conceive of an arrangement in which a minute semitransparent object with homogeneous or known dispersion is transilluminated by a collimated coherent light beam from a tunable dye laser which can also be made to provide a coherent reference point source in the immediate vicinity of the object. The resulting reference and the object scattered wavefields are intercepted by the photocathode of an electronic imaging device of known spectral response such as a vidicon. Because of the minute size of the object, the photocathode can easily be situated in the far field of the object. Thus nearly a lensless Fourier transform hologram recording arrangement results. The spatial frequency content in the resulting hologram is therefore expected to be sufficiently low to be resolved by a high resolution electronic imaging device. By recording and digitally storing the resulting detected hologram fringe pattern as a function of dye laser wavelength one can gain access to the 3-D Fourier space of the object, since I_{k_i} and I_R are precisely known for the recording geometry.

A similar recording arrangement can be envisioned in the active coherent imaging of a distant reflecting object (active telescopy) where the object can be made to furnish a reference point source situated on its surface, such as a wavelength independent stationary glint point or an intentionally placed retroreflector. Because in such an arrangement the reference and the object wavefields travel over the same path, atmospheric effects are expected to be minimized. The generation of an

object derived reference geometry in longwave (microwave and acoustic) wavelength diversity imaging has been described elsewhere[20,27].

Finally it is worthwhile to note that since the scattering process is linear the multiaspect or multistatic frequency or wavelength response measurements referred to in this paper can be obtained also by measuring the multiaspect impulse response followed by a Fourier transformation of the individual impulse responses that have been measured[19]. This means that impulsive illumination can also be utilized. Because the impulse response of a linear system can be measured by using random noise excitation and by cross-correlating the output with the input[19], the possibility also emerges of using random noise (white light) illumination and cross-correlation detection rechniques as a means for accessing the 3-D Fourier space of the object.

ACKNOWLEDGEMENT

The research presented in this paper was sponsored in part by the U.S. Air Force Office of Scientific Research, Air Force Systems Command, USAF under grant No. AFOSR-77-3256A and in part by U.S. Army Research Office, Durham under grant No. DAAG-76-G-0230.

REFERENCES

1. Schelkunoff, S.A., Bell Syst. Tech. J., 22, 80, (1943).

2. Anderson, A.P. and J.C. Bennet, Proc. IEE (letters), 64, 376, (1976).

3. DiFrancia, G.T., J. Opt. Soc. Am., 45, 497, (1955).

4. DiFrancia, G.T., J. Opt. Soc. Am., 59, 799, (1969).

5. Nassenstein, H., Opt. Comm., 2, 231, (1970).

6. Wernecke, S.J. and L. D'Addario, IEEE Trans. on Computers, C-26, 351, (1977).

7. Lukosz, W., J. Opt. Soc. Am., 56, 1463, (1966).

8. Leith, E.N., Advances in Holography, 2, N. Farhat (Ed,), (M. Decker, New York. 1976).

9. Lukosz, W., J. Opt. Soc. Am., 57, 932, (1967).

10. Bojarski, N.N., Final Report, contract B000-19-73-C-0316, Naval Air Syst. Command, (1974).

11. Lewis, R.M., IEEE Trans. on Ant. and Prop., AP-17, 308, (1969).

12. Raz, S.R., IEEE Trans. on Ant. and Prop., AP-24, 66, (1976).

13. Meier, R.W., J. Opt. Soc. Am., 55, 987, (1965).

14. Stroke, G.W., Appl. Phys. Letters, 6, 272, (1965). Also in: An Introduction to Coherent Optics and Holography, 2nd Edition, (Academic Press, New York, 1969), 114.

15. Farhat, N.H. and C.K. Chan, in Optica Hoy Y Manăna, J. Bescos et. al. (eds.), (Sociedad Espanola De Optica, Madrid, 1978), 399.

16. Farhat, N.H., Ultrasonics Symposium Proceedings, IEEE Cat. No. 75 CHO 944-4SU, (1975).

17. Farhat, N.H., Proc. International Optical Computing Conference, IEEE Cat. No. 76-CH 1100-7C, (1976).

18. Farhat, N.H., Proc. IEEE (letters), 64, 379, (1976).

19. Farhat, N.H., J. Opt. Soc. Am., 67, 1015, (1977).

20. Farhat, N.H. and C.K. Chan, in Acoustical Imaging, A. Metherell (ed.), (Plenum, New York. 1980), 499.

21. Waters, W.M., Proc. IEEE (letters), 66, 609, (1978).

22. Chan C.K., Analytical and numerical studies of frequency swept imagery, Ph.D. Dissertation, Univ. of Pennsylvania, Philadelphia, (1978).

23. Stroke, G.W. and M. Halioua, Trans. Amer. Crystallographic Assoc., 12, 27, (1976).

24. Farhat, N.H., Univ. of Pennsylvania Report No. F1 Annual Report, AFOSR Grant No. 77-3256, July (1978).

25. Bracewell, R.N. and S.J. Wernecke, J. Opt. Soc. Am., 65, 1342, (1975).

26. Bracewell, R.N., Australian Journal of Physicas, 9, 198, (1956).

27. Farhat, N.H., C.K. Chan and T.H. Chu, Proc. AP-S/URSI, Symposium, Quebec, Canada (1980).

28. Stroke, G.W., in Applications of Holography, E.S. Barrakette, W.E. Kock, T. Ose, J. Tsuyiuchi and G.W. Stroke, (Eds.),(Plenum Press, New York, 1971), 35.

29. Ojeida-Castenada and S. Guel Sandoval, App. Optics, 18, 3350, (1979).

APPENDIX III

THE VIRTUAL FOURIER TRANSFORM AND ITS APPLICATION IN THREE DIMENSIONAL DISPLAY

(Paper published in *Optics in Four Dimensions* M.A. Machado and L.M. Narducci (Eds.), Am. Inst. of Phys., New York, 1981)

Published in Optics in Four Dimensions.
M.A. Machado and L.M. Narducci (Eds.), Am. Inst. of Phys., New York 1981

THE VIRTUAL FOURIER TRANSFORM AND ITS APPLICATION IN THREE DIMENSIONAL DISPLAY

N.H. Farhat and C.Y. Ho
University of Pennsylvania
The Moore School Graduate Research Center
Philadelphia, PA 19104

ABSTRACT

In contrast to the well known and widely used instantaneous Fourier transforming property of the convergent lens in coherent (laser) light, the "Virtual Fourier Transform" (VFT) capability of the divergent lens is less widely known or used despite many advantages. We will review the principle of the VFT and discuss its advantages in certain applications. In particular a method for viewing the virtual Fourier transform of a two dimensional function with the naked eye using an ordinary point source will be presented. A scheme for three-dimensional image display based on a "Fourier domain projection theorem" utilizing varifocal VFT is described and a discussion of the properties of the displayed image given.

INTRODUCTION

Several sophisticated three dimensional (3-D) imaging techniques such as x-ray tomography[1], electron microscopy[2], crystallography[2], wave-vector diversity imaging and inverse scattering[3], involve measurements that give access to a finite volume in the 3-D Fourier space of a 3-D object function. A 3-D image of the original object can then be reconstructed by computing the inverse 3-D Fourier transform. The retrieved iamge normally represents the spatial distribution of a relevant parameter of the object such as absorption, reflectivity, scattering potential, etc.

Obviously, the required inverse transform can be performed digitally. Digital techniques however often preclude real-time operation particularly when the object being imaged is not simple but contains considerable resolvable intricate detail. More importantly, because of the inherent two dimensionality of CRT computer displays, direct true 3-D image display is not possible. Present day computer graphic displays are capable of displaying 3-D image detail either in separage cross-sections or slices, or in a computed perspective (isometric) view of the object, or in some instances stereoscopically where an illusion of a 3-D scene is created in the mind of the observer who is required usually to use special viewing glasses[4,5].

Hybrid (opto-digital) computing techniques offer an alternate approach to 3-D image retrieval from 3-D Fourier space data. They furnish as shown in this paper the ability to display true 3-D image detail. The approach is based on "Fourier Domain Projection Theorems"[2,3] that are dual to "Spatial or Object Domain Projection Theorems" used in radio-astronomy[6,7] and tomography[1]. These theorems permit the reconstruction of 3-D image detail tomographically* i.e. in slices from 2-D projections of the 3-D Fourier space data[2,3]. Although the required 2-D Fourier transform can be carried out digitally, the emphasis in this paper is on coherent optical techniques for performing the 2-D Fourier transform with particular attention to implementations that permit the execution of the necessary 2-D optical transforms of the various projection hologram sequentially in real-time. Specific attention is given to a technique that utilizes the virtual Fourier transform which permits the viewing of a virtual 3-D image in real-time.

FOURIER DOMAIN PROJECTION THEOREMS

There are two Fourier domain projection theorems. One leads to tomographic object reconstruction in parallel slcies and is called the "weighted Fourier domain projection theorem", the other leads to tomographic object reconstruction in meridonal or central slices and can therefore be called the "meridonal or central slice Fourier domain projection theorem".

We begin by considering a 3-D object function $f(\bar{r})$ with $\bar{r} = xI_x + yI_y + zI_z$ being a position vector in object space. Let $F(\bar{w})$ be the 3-D Fourier transform of $f(\bar{r})$ defined by,

$$F(\bar{w}) = \int f(\bar{r})\, e^{-j\bar{w}.\bar{r}}\, d\bar{r} \qquad (1)$$

where $d\bar{r} = dx\, dy\, dz$ and $\bar{w} = w_x I_x + w_y I_y + w_z I_z$ is a position vector in the Fourier or spatial frequency domain.

Consider next the projection of $F(\bar{w})$ on w_x, w_y plane defined by,

$$F_p(w_x,w_y) = \int_{w_z} F(w)\, dw_z \,. \qquad (2)$$

and combining eq. (1) and (2),

$$F_p(w_x,w_y) = \int_{w_z} \{\iiint_{xyz} f(x,y,z) e^{-j(w_x x + w_y y + w_z z)}\, dxdydz\} dw_z \qquad (3)$$

---

*From the Greek work Tomos meaning slice.

Integrating with respect to w_z first and assuming that the volume in $\bar{w}$ space occupied by $F(\bar{w})$ is sufficiently large we obtain,

$$F_p(w_x,w_y) = \int_x \int_y \int_z f(x,y,z)\, \delta(z) e^{-j(w_x x + w_y y)}\, dxdydz \qquad (4)$$

$$= \int_x \int_y f(x,y,o)\, e^{-j(w_x x + w_y y)}\, dxdy \qquad (5)$$

The 2-D Fourier domain projection $F_p(w_x,w_y)$ and the central slice $f(x,y,o)$ through the object form thus a Fourier transform pair. This may be symbolically expressed as,

$$F_p(w_x,w_y) \leftrightarrow f(x,y,o) \qquad (6)$$

Other parallel slices through the object at $z = z_n$, z_n being a constant describing the z coordinate of the n-th parallel slice, can in a similar manner be related to "weighted" Fourier domain projections of $F(\bar{w})$ defined by,

$$F_{p,n}(w_x,w_y) = \int_{w_z} F(w) e^{jz_n w_z}\, dw_z \qquad (7)$$

Making use of eq. (1) and again performing the integration with respect to w_z first we obtain,

$$F_{p,n}(w_x,w_y) \leftrightarrow f(x,y,z_n) \qquad (8)$$

which indicates that the weighted projection $F_{p,n}(w_x,w_y)$ and the n-th parallel object slice $f(x,y,z_n)$ form a Fourier transform pair. Equation (6) is seen to be a special case of eq. (8) when $z_n = o$.

Given the 3-D Fourier space data manifold $F(\bar{w})$ one can digitally compute and display a set of "weighted projection holograms" $F_{p,n}(w_x,w_y)$. A corresponding set of images of parallel slices or cross-sectional outlines of the 3-D object can then be retrieved via 2-D Fourier transform operations which can most conveniently be carried out optically from photographic transparency records of the weighted projection holograms displayed by the computer.

Returning to eqs. (1) and (2) one can also show that projections of $F(\bar{w})$ on arbitrarily oriented planes other than the w_x, w_y plane chosen for eq. (2), yields "meridonal projection holograms" that are 2-D Fourier transforms of corresponding merdional (central) slices of the object. This is the "meridonal Fourier domain projection theorem. It furnishes the basis for angular multiplexing of the resulting meridonal projection holograms into a single composite hologram which can be used to form a 3-D iamge of the object in a manner similar to that in integral holography[8] which is increasingly being referred to as Cross holography*.

THE VIRTUAL FOURIER TRANSFORM

In contrast to the well known spatial Fourier transforming property[9] of the convergent lens widely used in coherent optical computing, the complementary virtual Fourier transform capability of a divergent lens[10] is less widely known or used despite many attractive features. This is surprising since the power spectrum associated with the VFT is a phenomenon that is frequently observed in daily life when one happens to look at a distant point source such as a street light through a fine mesh screen or the fine fabric of transparent curtain material. The spectrum of the screen transmittance appears then as a virtual image in the plane of the point source.

The VFT concept of the divergent lens is easily derived from the Fourier transform expression of the convergent lens. Figure 1 illustrate the well known process of forming a real Fourier transform with a convergent lens. The object transparency, with complex transmittance $t(x_o,y_o)$, is placed at a distance d in front of a convergent lens of focal length F and illuminated with a normally incidnet collimated laser beam. The complex field amplitude of the wavefield in the back focal plane, the transform plane, is given by the well known formula

$$T(x,y) = \frac{j}{\lambda F} e^{-j\frac{k}{2F}[(1-\frac{d}{F})(x^2+y^2)]} \times \iint_{-\infty}^{\infty} t(x_o,y_o)\, e^{j\frac{k}{F}(x\,x_o + y\,y_o)}\, dx_o dy_o \qquad (1)$$

in which the integral is recognized as the two dimensional Fourier transform of the object transmittance. $T(x,y)$ becomes the exact Fourier transform of $t(x_o,y_o)$ when $d = F$ that is when the object transparency is placed in the Front focal plane of the lens. The power spectrum associated with the transform is real and can be projected on a screen placed in the back focal plane. It is also well known that a scaled version of the transform can be obtained in the back focal plane by placing the object tranparency in the converging laser beam to the right of the lens[9].

*Named after Lloyd Cross the originator of integral holography.

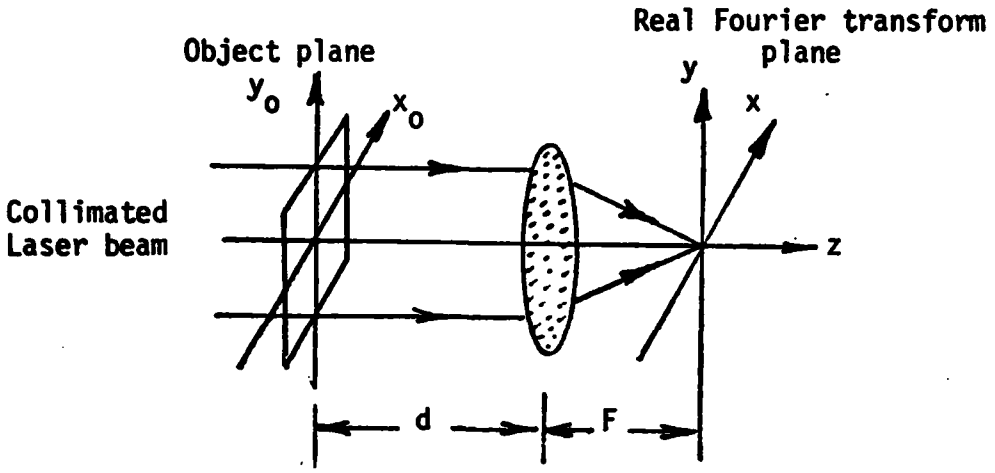

Fig. 1. Real Fourier transform formed with a convergent lens

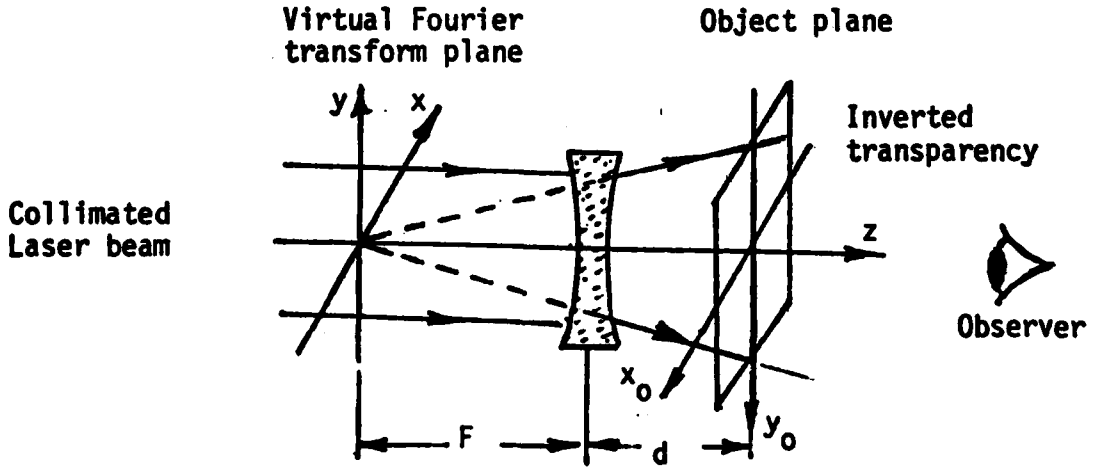

Fig. 2. Virtual Fourier transform formed with a divergent lens

Noting that eq. (1) does not change when we replace d by -d, F by -F, x_0 and y_0 by $-x_0$ and $-y_0$ respectively, we can arrive at the complementary VFT arrangement illustrated in Fig. 2. An inverted transparency $t(x_0,y_0)$ is placed now in the divergent coherent beam to the right of the divergent lens (of focal length -F) and a VFT given by eq. (1) is observed in the virtual focal plane of the lens. The same VFT can be seen by removing the divergent lens and replacing the laser beam with a point source placed at the origin of the VFT plane as depicted in Fig. 3. Thus a simple way of viewing the power spectrum associated with the VFT of a given diffracting screen (which is usually a Fourier transform hologram or a projection hologram of the type described above) is to hold the screen close to the eye and look through it at a distant bright point source. The point source used need not be derived from a laser. In fact it is preferable for safety purposes to use an LED or a spectrally filtered minute white light source such as a "grain-of-wheat" subminiature incandescent lamp or a miniature Christmas tree decorating lamp covered by a color or interference filter. This has the added advantage of furnishing a measure of control over the coherence properties of the wavefield impinging on the screen providing thereby a means for reducing coherent noise in the observed VFT and also, as will be discussed below, a means for coherent or noncoherent superposition of VFT's. As the distance of the point source from the diffracting screen is decreased in order to make it compatible with typical laboratory or optical bench dimensions, the size of the observed VFT decreased because of the change in the curvature of the wavefield illuminating the diffracting screen. To compensate for this effect it is necessary to reduce the size of the diffracting screen or transparency often to such a scale where viewing the VFT throught the small available aperture becomes difficult. To overcome this limitation the displacement property of the Fourier transform can be utilized. A composite transparency containing an ordered or random array of reduced replicas of the transmittance function $t(x_0,y_0)$ arranged side by side as illustrated in Fig. 4 is prepared. When such a composite transparency is viewed with the point source, the VFT's formed by the individual elements will overlap in the virtual Fourier plane. The VFT's are identical except for Linear phase dependence on x,y which depends in each VFT on the central position of each element in the composite transparency. This leads to a desirable noise averaging effect and the appearance of fine checkered texture in the image detail. All this leads to an enhancement of the quality of the observed power spectrum. Both coherent and noncoherent superposition of the overlapping VFT's is possible using this scheme by varying the coherence area of the wavefield illuminating the composite transparency. When the coherence area is roughly equal to the size of the individual elements of the composite transparency noncoherent superposition results, while a coherence area equal or greater than the size of the composite transparency would yield coherent superposition.

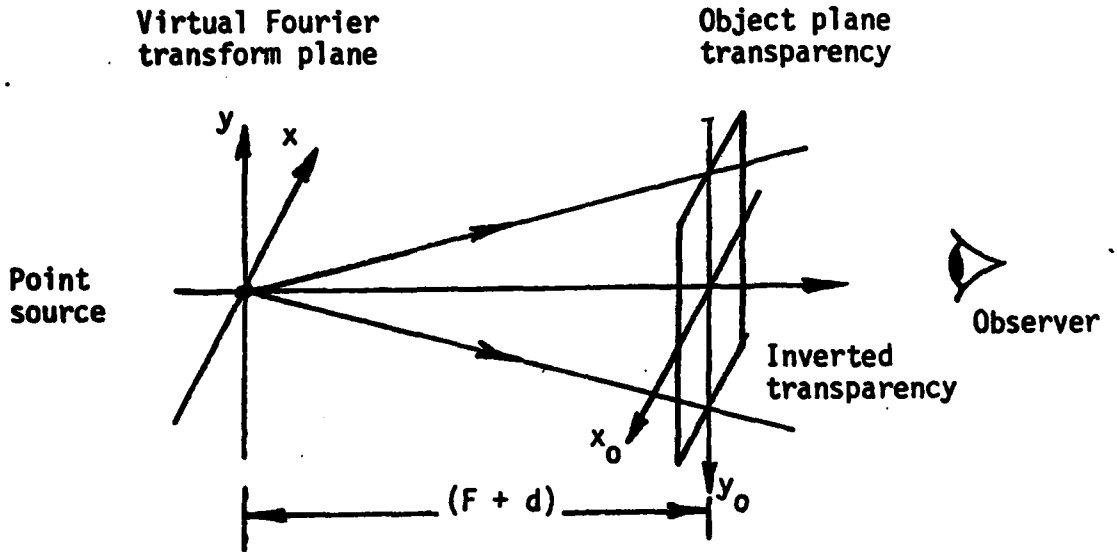

Fig. 3. Arrangement for viewing a virtual Fourier transform with a point source

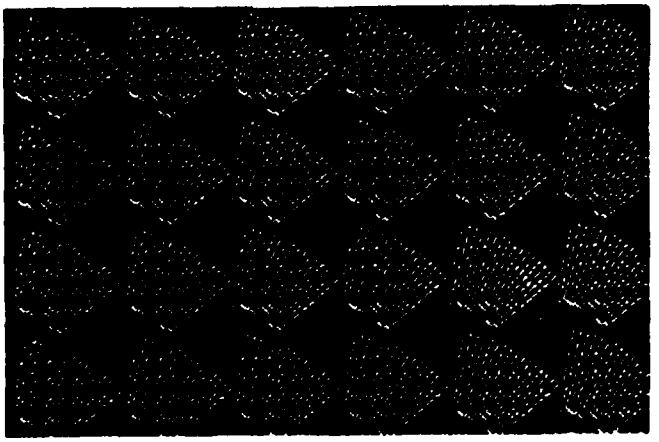

Fig. 4. A composite screen consisting of an ordered array of identical Fourier transform projection holograms.

THREE DIMENSIONAL DISPLAY

The VFT concept and the "weighted Fourier domain projection theorem" discussed above can be combined in an attractive scheme for the reconstruction and display of a 3-D image from a series of weighted projection holograms corresponding to different parallel slices through the object. The scheme is based on viewing a series of weighted projection holograms sequentially in the proper order of the occurance of their corresponding slices in the original object while displacing the point source axially for one hologram to next by an axial increment proportional to the spacings bwtween adjacent object slices. In this fashion the reconstructed virtual images of the various slices are seen in depth at different VFT planes that are determined by the positions of the axially incremented point source. Repeated rapid execution of this procedure by displacing the point source back and forth leads the observer to see a virtual 3-D image tomographically in parallel slices or sections as he looks through the series of projection holograms passed rapidly, as in a motion picture film, infront of his eyes.

More specifically the scheme is based on preparing a series of N weighted Fourier domain projection holograms from the 3-D Fourier domain data $F(\bar{w})$ of a given object $f(\bar{r})$ as described in the preceeding sections. Each of the projection holograms would correspond to a different parallel slice through the object. A composite transparency similar to that shown in Fig. 4 is formed for each projection hologram. In fact Fig. 4 is an example of a computer generated composite hologram containing an array of identical weighted projection holograms corresponding to one slice of the test object shown in Fig. 5. The test object chosen consisted of eight point scatterers arranged as shown. The 3-D Fourier space of this test object was accessed in a computer simulation of wavelength diversity imaging as described in a companion paper in this volume*. The resulting computer generated Fourier space data manifold $F(\bar{w})$ was used to compute three weighted projection holograms corresponding to the three planes R_z'=1m,0,1m of Fig. 5 containing the three different distributions of point scatterers. A composite array such as that of Fig. 4 was formed and displayed by the computer for each of the three projection holograms, each was photographed yielding a set of three projection hologram composite transparencies. Copies of these were then mounted on a rotating wheel as shown in Fig. 6 (a) and viewed with an axially scanned point source. Four sets of transparency copies of these three composite projection holograms were mounted in the order 1,2,3,2,1,2 ... on the periphery of a rotating wheel as shown in Fig. 6 (a). The wheel is driven by a computer controlled stepper motor. The axially scanned point source was produced by scanning a focused laser beam back and forth on a length of fine nylon thread with the aid of a deflecting mirror mounted on the shaft of a second computer controlled stepper motor as shown in Fig. 6 (b). The laser and optical bench arrangement for forming the scanned focused beam appear in the background of Fig. 6 (a). The computer controlled steppers enable precise positioning of the secondary point source on the scattering thread in synchronism with the hologram

*See paper entitled "Holography, Wavelength Diversity Inverse Scattering" in this volume.

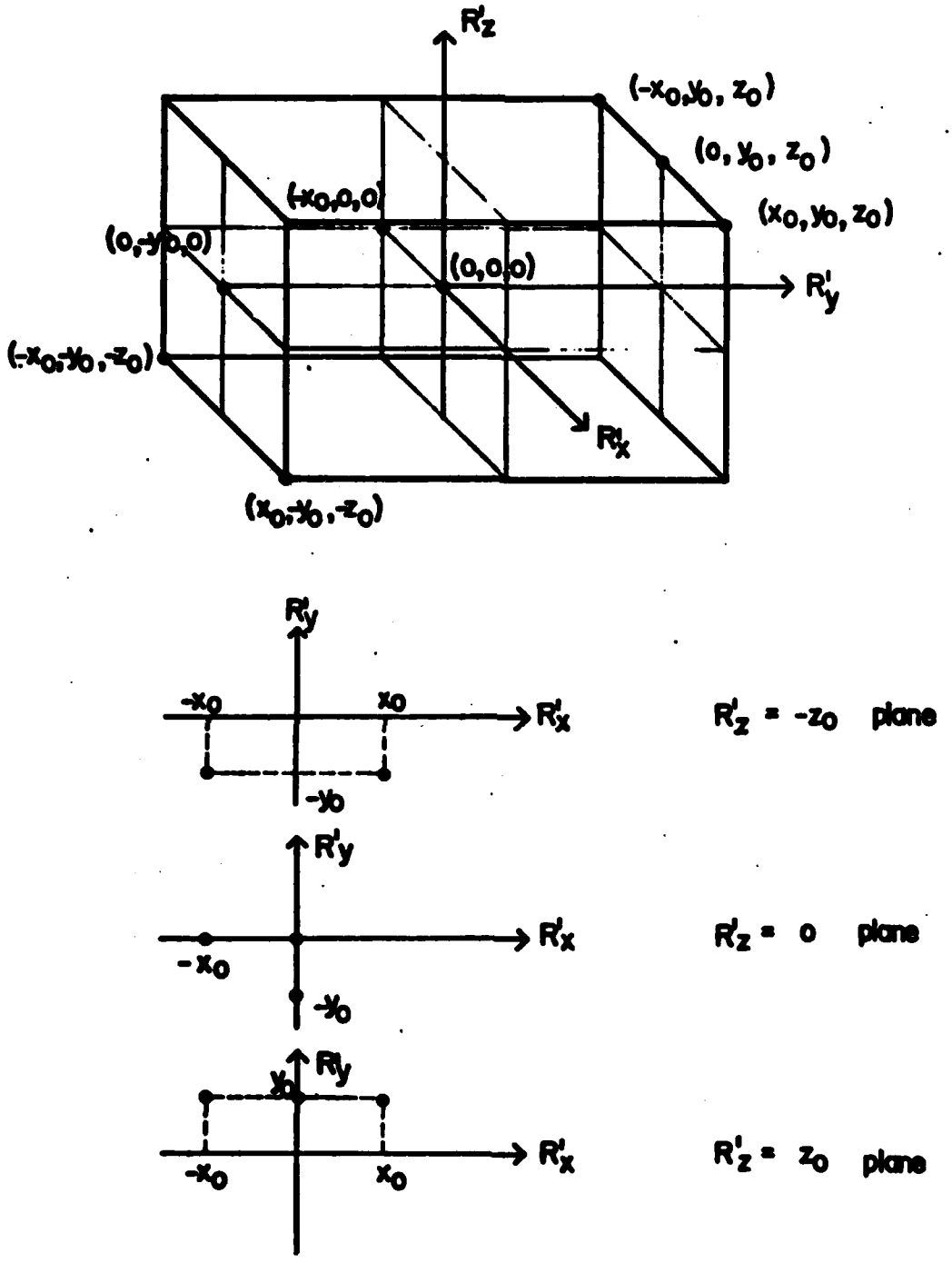

Fig. 5. A three-dimensional test object consisting of a set of eight point scatterers shown in isometric and R'_x-R'_x plane views at R'_z=$-z_0$,0,z_0. x_0=y_0=z_0=100 cm.

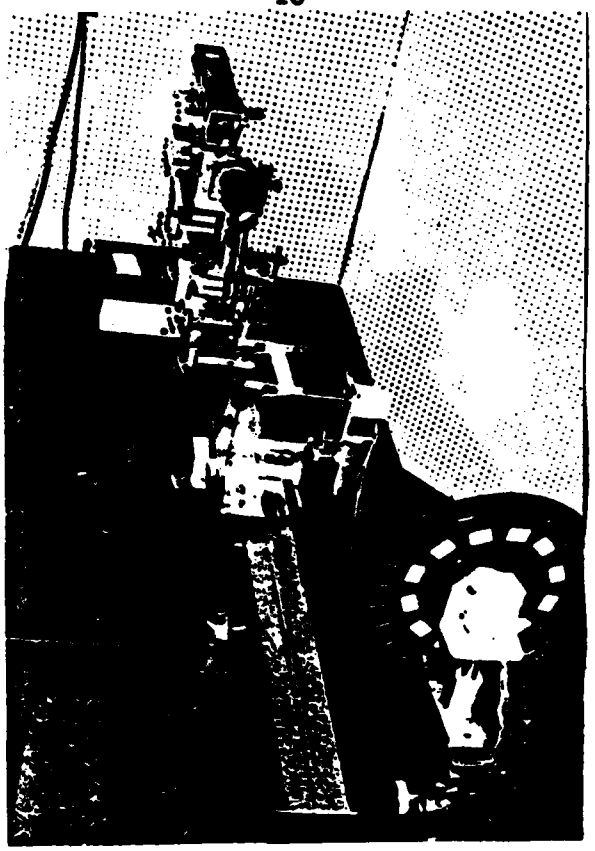

(a)

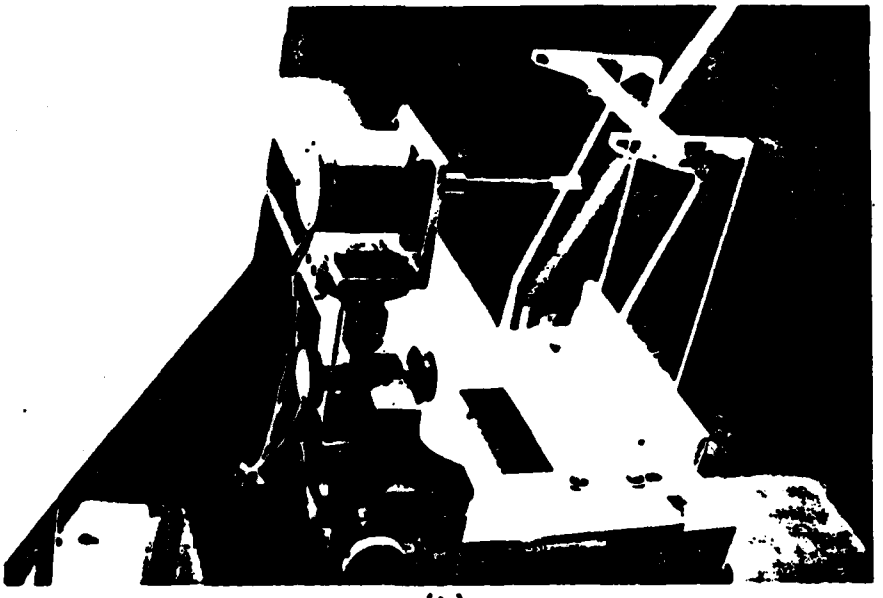

(b)

Fig. 6. Quasi real-time three-dimensional image reconstruction and tomographic display in successive slices from a series of projection holograms mounted on rotating wheel seen in fore-front of (a); Detail of laser scanner used to produce linearly scanned point source is shown in (b).

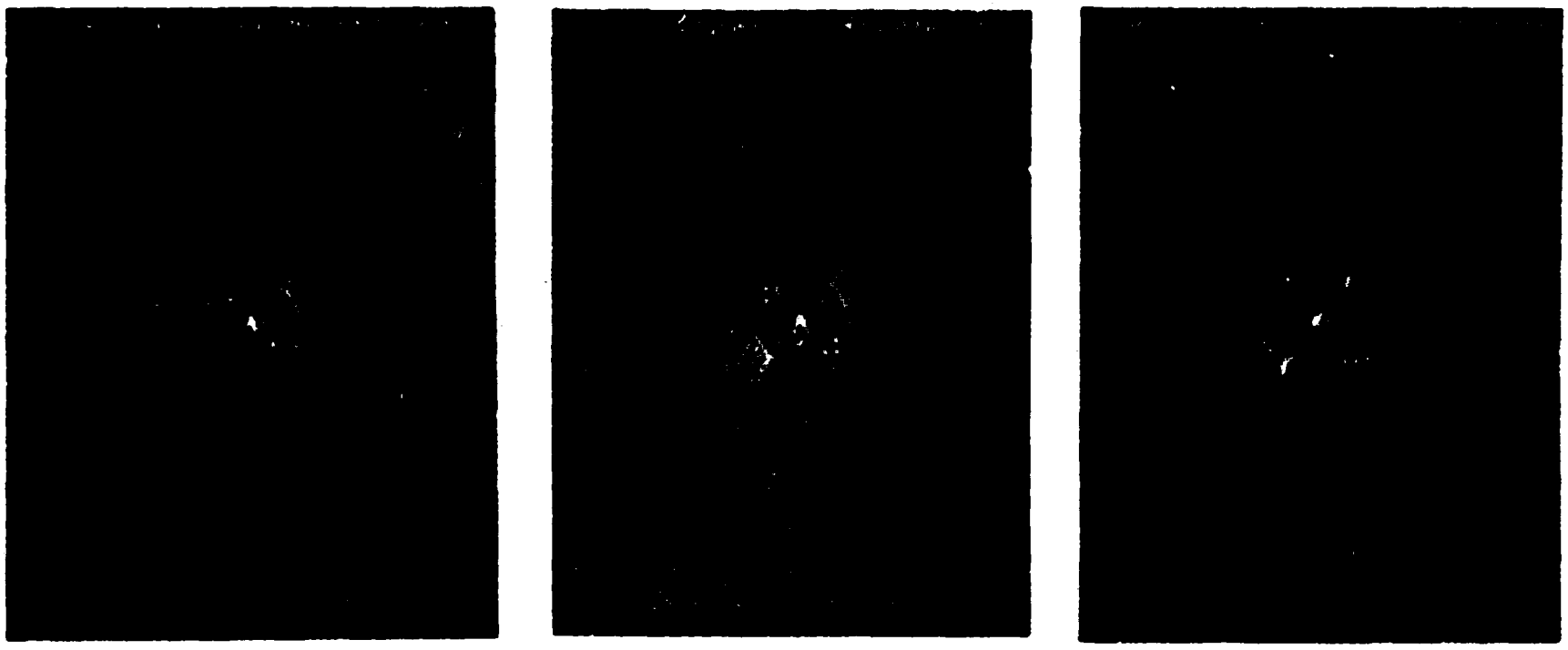

(a) (b) (c)

Fig. 7. Photographs of three slices of the virtual 3-D image of the test object of Fig. 5 obtained by photographing the VFT's formed from corresponding Fourier domain projection holograms.

being viewed so that the VFT are formed in their proper planes. A viewer looking at the axially displaced point source through each transparency mounted on the wheel as it passes infront of his eye will see a 3-D virtual image. Photographs of the three virtual images seen by an observer in this fashion are shown in Fig. 7. An opto-digital scheme for rapid real-time implementation of the procedure realized above is shown in Fig. 8. This scheme, presently under study, utilizes a rapid recyclable spatial light modulator (SLM) such as the Itek PROM in order to form VFT's of the projection holograms displayed by the computer in real-time.

CONCLUSIONS

We have presented the basic principles of tomographic 3-D image display based on Fourier domain projection theorems. One possible implementation of the principle using the virtual Fourier transform and a series Fourier domain projection holograms has been described. There are several advantages for using the VFT rather than the real Fourier transform (RFT), the most important of which is the ease with which the position of the VFT plane can be moved axially by simply moving the position of the reconstruction point source. The VFT approach was adopted in the present study because it is much easier to move a point source rapidly than to move the display screen needed in the RFT approach. Furthermore focusing in the VFT approach is carried out by the observer while in the RFT approach it must be performed by the system. Other attractive features of the VFT are:

(a) Simplicity - enables direct viewing of the power spectrum of a transparency or a hologram with a variety of simple point sources.

(b) The scale of the observed VFT can be easily altered by changing the distance between the projection hologram transparency and the reconstruction point source.

(c) Lower speckle noise and therefore higher reconstructed image quality can be attained by using nonlaser point sources in the reconstruction such as LED or miniature spectrally filtered incandescent lamps. Further reduction in speckle noise occurs when an array of the projection hologram rather than a single hologram is used and when the hologram is slightly vibrated or is in motion because of a noise averaging effect.

(d) Coherent and noncoherent superposition of VFT's is possible by altering the coherence area of the reconstruction wavelfield.

(e) Because of the Fourier transform nature of the projection holograms utilized, the resolution requirements from the storage medium (photographic film or the CRT/SLM system of Fig. 8) are much lower than would be needed in the recording of a Fresnel hologram of the object as a means of 3-D image display. The 3-D image detail contained in the single Fresnel hologram is now distributed over a series of lower resolution projection holograms which are used to form the 3-D image sequentially in time in individual slices.

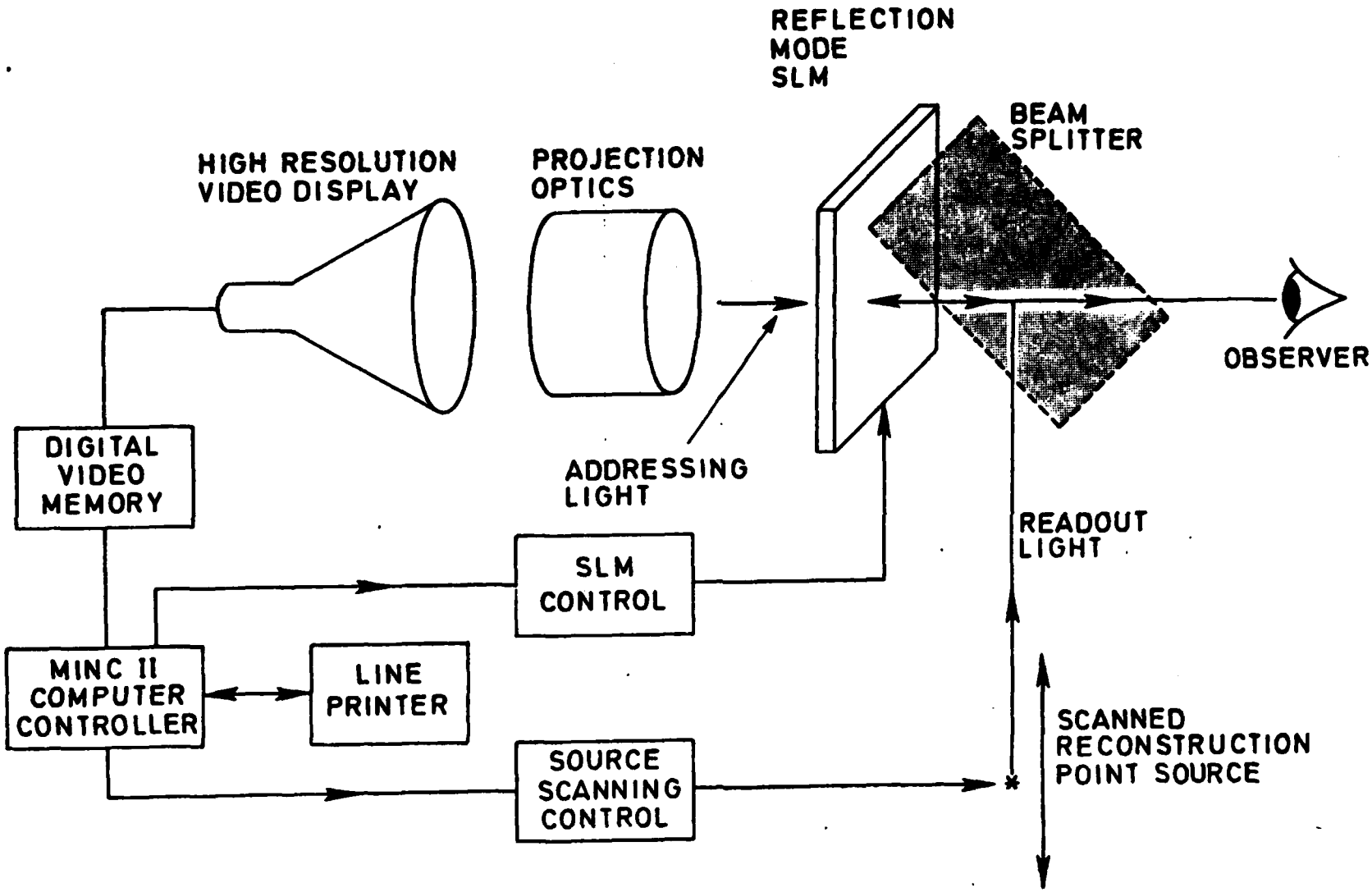

Fig. 8. Opto-digital scheme for the reconstruction and display of 3-D images using a recyclable spatial light modulator and a point source to view the VFT in real-time.

(f) Because 3-D image reconstruction is tomographic (in separate slices) there is no interference between the wavefields forming the various slices.

(g) Permits other forms of 3-D image display involving spatial or angular multiplexing in a fashion similar to integral holography.

ACKNOWLEDGEMENT

Research work reported here was supported by the U.S. Army Research Office under Grant No. DAAG29-80-K-0024 and by the U.S. Air Force Office of Scientific Research, Air Force Systems Command, under Grant No. AFOSR-77-3256-D.

REFERENCES

1. H.H. Barret and M.Y. Chiu, Optica Hoy Y Manãna, J. Bescos et.al., (eds.) 136, (Proc. of ICO-11, Sociedad Española De Optica, 1978).

2. N.H. Farhat and C.K. Chan, Acoustical Imaging, 8, 499, A. Metherel (ed.), (Plenum Press, New York, 1980).

3. G.W. Stroke and M. Halioua, Trans. Amer. Crystallographic Assoc., 12, 27, (1976).

4. T. Okoshi, Three-Dimensional Imaging Techniques, (Academic Press, New York, 1976).

5. T. Okoshi, Proc. IEEE, 68, 548, (1980).

6. R.N. Bracewell, Australian Journal of Physics, 9, 148, (1956).

7. R.N. Bracewell and S.J. Wernecke, J. Opt. Soc. Am., 65, 1342,(1975).

8. D.L. Vickers, Lawerence Livermore Laboratory Report, No. UCID-17035, (February 1976).

9. J.W. Goodman, Introduction to Fourier Optics, 83, (McGraw Hill, New York, 1968).

10. J. Knapp and M.F. Becker, App. Optics, 17, 1669, (1976).

APPENDIX IV

FREQUENCY SWEPT TOMOGRAPHIC IMAGING OF THREE-DIMENSIONAL PERFECTLY CONDUCTING OBJECTS

(Paper published in IEEE Trans. on Ant. and Prop. Vol. AP-29 - Special Issue on Inverse Methods in Electromagnetics, March 1981)

Frequency Swept Tomographic Imaging of Three-Dimensional Perfectly Conducting Objects

CHI K. CHAN, MEMBER, IEEE, AND NABIL H. FARHAT, FELLOW, IEEE

Abstract—The use of frequency swept or frequency diversity techniques to achieve superresolution in the imaging of three-dimensional perfectly conducting objects is studied and demonstrated by computer simulations. The frequency swept imaging concept is found to be a generalization of the inverse scattering theory. By invoking Fourier domain projection theorems, it is demonstrated analytically that images of separate slices of three-dimensional targets can be obtained, thus establishing the feasibility of a tomographic radar. Computer simulation results that verify these theories for extended and composite point scattering objects are presented.

I. INTRODUCTION

ONE OF THE MAIN design objectives of a microwave imaging system is to have good image resolution. It would be highly desirable if the microwave resolution can approach that of an optical imaging system. Such high resolution coupled with the excellent penetration of microwaves through dielectrics, inclement weather, and low-loss materials can lead to important advances in radar, nondestructive testing, and certain types of medical imaging with ultrasound substituting for microwaves. The attainment of high resolution by conventional means is, however, not an easy task because of practical limitations stemming from the fact that microwaves are more than 10^5 times longer than optical wavelengths. It is easy to show using the well-known classical Rayleigh criterion for estimating the two-point resolution of an imaging system that in order to make a microwave imaging system operating, for example, at 15 GHz attain the same angular resolution as a 5-cm diameter optical aperture operating at a mean wavelength of 0.5 μm, the recording aperture for the microwave imaging system has to be 2 km in size. The number of coherent receivers needed to adequately sample the object scattered field over such an aperture would be prohibitively large rendering the whole idea economically unattractive even if technically feasible.

Because of the rapid growth of microwave remote sensing in both military surveillance and civilian applications such as geological exploration and all-weather radar systems for aircrafts, there is a constant demand for improvement of image resolution. Towards this goal, different attempts have been made to try and achieve a resolution better than that predicted by the Rayleigh resolution criterion as applied to the available recording aperture. The basic idea normally involved is to extend the effective area of the physical recording aperture through clever mathematical data processing techniques or data acquisition schemes. In this fashion, by synthesizing an effective receiving aperture larger than the actual physical aperture of the imaging system, resolution better than the classical resolution limit of the available physical aperture, or in other words, superresolution, is achieved. However, most of these methods are either extremely sensitive to noise or are only applicable in tightly controlled environments [1]-[10]. The term superresolution is customarily associated with analytic continuation methods where the complex field amplitude recorded over a specified aperture is utilized to compute the values of the field outside the aperture boundary. In this way, one can progressively determine the complex field amplitude over an area larger than the physical aperture available and achieve thereby higher resolution than that determined by the data recorded over only the physical aperture. It is in this sense that the term superresolution is used in this paper. We record the field over a given finite aperture at several frequencies or over a given frequency range, then sort out the data to synthesize a larger size aperture that gives rise to a superresolved image; i.e., an image of higher resolution than that obtained with the original monochromatic physical aperture. A most practical and effective method in achieving superresolution, in the authors' opinion, is through the utilization of the "time channel" whereby one collects in time more information about the scattering object or equivalently synthesizes added dimensions to the available recording aperture [11]. The well-known principle of the synthetic aperture radar (SAR) and the frequency swept imaging (FSI) principle described in this paper represent two examples that utilize the time channel to increase the amount of information collected and thereby also resolution. In the SAR example a time derived two-dimensional aperture is synthesized by either motion of the monostatic transmitter-receiver pair [12], [13], [35] or motion of the target [14] and by sweeping of the ground swath with the illuminating pulse. In FSI, the linear FM or chirp signal produced by a transmitter is used to synthesize added dimension to the recording aperture. No motion of either transmitter-receiver or target is necessary for this imaging scheme. These methods are much more practical in achieving superresolution than the techniques mentioned earlier because additional data are not extrapolated but are actually gathered by relative motion between the object, the transmitter, receiver, or as in FSI, by frequency sweeping or frequency diversity.

The concept of synthesizing an imaging aperture by frequency sweeping was analyzed by Farhat [15] and also studied later by Jain [16]. It was found that by sweeping the frequency of the incident illumination, a one-dimen-

Manuscript received September 26, 1979; revised November 24, 1980. This work was supported in part by the Air Force Office of Scientific Research, Air Force Systems Command under Grant AFOSR-77-3256A and in part by the Army Research Office under Grant DAAG29-76-G-0230. This paper is based on portions of a dissertation submitted to the University of Pennsylvania in partial fulfillment of the requirements for the Ph.D. degree.

C. K. Chan was with The Moore School Graduate Research Center, University of Pennsylvania, Philadelphia, PA 19104. He is now with the Lincoln Laboratory, Massachusetts Institute of Technology, Lexington, MA 02173.

N. H. Farhat is with The Moore School Graduate Research Center, University of Pennsylvania, Philadelphia, PA 19104.

0018-926X/81/0300-0312$00.75

sional aperture can, under certain circumstances, be synthesized with a single coherent receiver. In the case of a linear array of receivers, a two-dimensional recording aperture can be generated [17]. Direct extension of the FSI concept to the imaging of three-dimensional objects is not straightforward because of the limitations of the Fresnel Kirchhoff diffraction integral formulation to one- and two-dimensional distributions. An approximate Fourier optics approach is possible, however [32]. Here a more precise formulation is developed.

It was shown in 1969 by Bojarski and Lewis [18], [19] that a three-dimensional Fourier transform relationship exists between the shape of a three-dimensional perfectly conducting object and its backscattered far field. It was found that by recording the monostatic backscattered far field at different frequencies and target aspect angles, the three-dimensional shape of the object can be retrieved.

In this paper, we will show that the extension of the FSI concept to three-dimensional objects is a multistatic generalization of the work of Bojarski and Lewis which was also studied by Raz [20]. It will also be shown that by chirping the transmitted signal and receiving the target echoes by a two-dimensional receiver array, a space-time signal containing the three-dimensional far-field spectrum of the target is recorded. By using the Fourier transform property between the three-dimensional object and its far-field images of slices of the three-dimensional object can be reconstructed. The concepts discussed are verified for both extended and point objects employing computer generated data and hybrid (digital/optical) data processing in the image reconstruction. Although the discussion refers specifically to frequency swept techniques, it will be clear that other frequency diversity techniques such as frequency stepping or simultaneous multifrequency illumination and reception with channelized receivers are equally applicable.

II. THE THEORY OF FREQUENCY SWEPT IMAGING

It is well-known [19], [21], [22] that in the physical optics approximation the scattered far field for a perfectly conducting object illuminated by a plane monochromatic wave is given by

$$E_s(P_0) = \frac{jE_0}{4\pi R} e^{-jk(R+R_t)} \iint_{S_{III}} \bar{n} \cdot \bar{p} e^{j\bar{p}\cdot\bar{R}'} \, da' \tag{1}$$

where $\bar{p} = \bar{k}_0 - \bar{k}$ and, as shown in Fig. 1, $(R + R_t)$ is the round trip distance between the transmitter, scatterer, and the receiver. $\bar{k}$ is the incident wave vector along the line from transmitter to center of scatterer, $\bar{k}_0$ is the "scattering" wave vector in the direction of the observer along the line from the center of the scatterer to the receiver at P_0 which is located in the far field of the object. S_{III} is the illuminated surface of the scatterer, $\bar{n}$ is the outward normal, and da' is the differential surface element. The result in (1) shows that for the case of plane monochromatic incident illumination, the scattered far field recorded by the receiver can be expressed in two parts: 1) the exponential term $e^{-jk(R+R_t)}$ which accounts for the propagation time delay from the transmitter to the center of the scattering object and back to the receiver; and 2) the integral which is characteristic of the scattering body.

When the incident illumination is nonmonochromatic or broad-band, e.g., linear FM, i.e.,

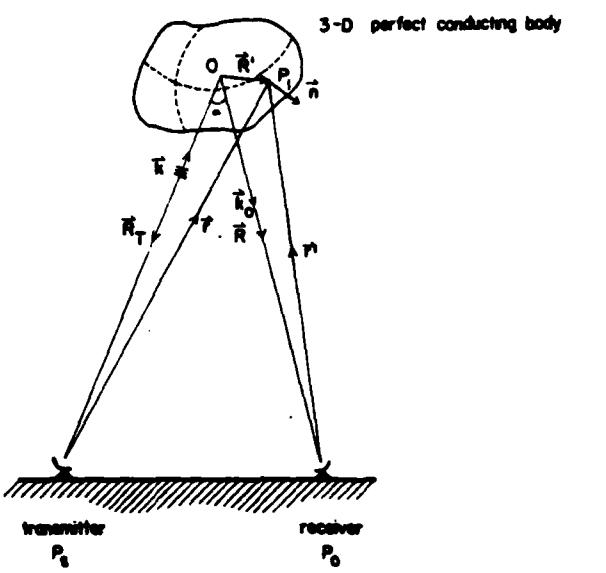

Fig. 1. Scattering geometry. Incident plane wave with wave vector $\bar{k}$ is scattered by three-dimensional perfectly conducting object. Scattered far field is recorded by receiver at location $\bar{R}$.

$$E_i = E_0 e^{j(\omega_1 t + \frac{1}{2}\gamma t^2)} \tag{2}$$

the scattered far field is given by [5]

$$E_s(\bar{R}, t) = -j \frac{E_i\left(t - \dfrac{R + R_t}{c}\right)}{4\pi R} \iint_{S_{III}} \bar{n} \cdot \bar{p}(t) e^{j\bar{p}(t)\cdot\bar{R}'} \, da' \tag{3}$$

where

$$\bar{p}(t) = k(t)(\bar{l}_m - \bar{l}_k) \tag{4}$$

and $k(t) = k_1(1 + \gamma t)$ is the time dependent wavenumber for the linear FM transmitted wave, with γ being the chirp rate $\bar{l}_m$ and $\bar{l}_k$ are unit vectors in the direction of $\bar{k}_0$ and $\bar{k}$, respectively.

Equation (3) shows that when the incident illumination is a chirp waveform, the scattered far field recorded by a receiver is also a chirp but time delayed by the propagation time and modulated by a time dependent integral that is dependent on the structure of the scatterer and the directions of illumination and observation. Comparing (1) and (3) reveals the similarity between the two cases. The difference in the FSI case is that by illuminating the three-dimensional perfect conductor with a time dependent wave form (chirp), the recorded scattered far field that characterizes the scatterer is also time dependent. It is this time dependent integral in (4) which gives rise to the image of the scatterer.

III. FREQUENCY SWEPT IMAGING AND INVERSE SCATTERING

In this section, the relationship between bistatic FSI and the inverse scattering imaging problem is discussed. It is

found that FSI is a multistatic generalization of the work of Bojarski and Lewis [18], [19].

The surface integral in (3) can be defined as $\rho[\bar{p}(t)]$ as follows:

$$\rho[\bar{p}(t)] = -\frac{j}{2\sqrt{\pi}} \iint_{S_{ill}} \vec{n} \cdot \bar{p}(t) e^{j\bar{p}(t)\cdot\bar{R}'}\, da' \tag{5}$$

where $\rho[\bar{p}(t)]$ is a function of the directions of the incident illumination (i_k) and the receiver (i_m) and the nature of the illuminated surface of the object. The quantity $\vec{n}\cdot\bar{p}$ can be regarded as a scattering strength of a surface element into $\bar{p}$ space. Equation (3) can now be written as

$$E_s(\bar{R}, t) = \frac{E_t\left(t - \dfrac{R + R_t}{c}\right)}{2\sqrt{\pi}R} \rho[\bar{p}(t)]. \tag{6}$$

Following a reasoning similar to that in Raz [20] with $\bar{p}$ now being a function of time t, it can be shown [33] that $\rho[\bar{p}(t)]$ is related to the characteristic function $O(\bar{R}')$ of the target by

$$\int_{\substack{\text{whole}\\ \bar{R}'\text{ space}}} O(\bar{R}') e^{j\bar{p}(t)\cdot\bar{R}'}\, d^3R'$$

$$= \frac{2\sqrt{\pi}}{|\bar{p}(t)|^2} \{\rho[\bar{p}(t)] + \rho^*[-\bar{p}(t)]\} \tag{7}$$

where

$$O(R') = \begin{cases} 1, & \bar{R}' \text{ in } V' \\ 0, & \bar{R}' \text{ not in } V' \end{cases} \tag{8}$$

with V' being the shaped volume of the object.

We define

$$\Gamma[\bar{p}(t)] = \int_{\substack{\text{whole}\\ \bar{R}'\text{ space}}} O(\bar{R}') e^{j\bar{p}(t)\cdot\bar{R}'}\, d^3R'. \tag{9}$$

It is evident that $\Gamma[\bar{p}(t)]$ is a three-dimensional spatial Fourier transform of the characteristic function $O(\bar{R}')$. In terms of $\rho[\bar{p}(t)]$ which can be derived from the measured data as indicated in (6),

$$\Gamma[\bar{p}(t)] = \frac{2\sqrt{\pi}}{|\bar{p}(t)|^2} \{\rho[\bar{p}(T)] + \rho^*[-\bar{p}(t)]\} \tag{10}$$

$$= \frac{\sqrt{\pi}}{k^2(t)(1 + \cos\alpha)} \{\rho[\bar{p}(t)] + \rho^*[-\bar{p}(t)]\} \tag{11}$$

where α is the angle between the transmitter the center of the scatterer and the receiver as shown in Fig. 1. We note from (4) that although $\bar{p}(t)$ is a function of time t, it can be treated as an independent variable permitting the rewriting of (9) in the form

$$\Gamma(\bar{p}) = \int_{\substack{\text{whole}\\ \bar{R}'\text{ space}}} O(\bar{R}') e^{j\bar{p}\cdot\bar{R}'}\, d^3R'. \tag{12}$$

The three-dimensional shape of the scatterer can therefore be reconstructed by inverse Fourier transforming $\Gamma(\bar{p})$, i.e.,

$$O(\bar{R}') = \int_{\substack{\text{whole}\\ \bar{p}-\text{space}}} \Gamma(\bar{p}) e^{-j\bar{p}\cdot\bar{R}'}\, d^3p \tag{13}$$

where d^3p is an element of volume in $\bar{p}$ space.

When $\Gamma(\bar{p})$ is only measured in a finite portion of $\bar{p}$ space, a sampling function $H(\bar{p})$ can be defined as

$$H(\bar{p}) = \begin{cases} 1, & \text{where } \Gamma \text{ is measured} \\ 0, & \text{elsewhere.} \end{cases} \tag{14}$$

In this situation a diffraction limited characteristic function $O_d(\bar{R}')$, or three-dimensional "image" is expressed as

$$O_d(\bar{R}') = \int_{\substack{\text{whole}\\ \bar{p}\text{ space}}} \Gamma(\bar{p}) H(\bar{p}) e^{-j\bar{p}\cdot\bar{R}'}\, d^3p \tag{15}$$

$$= O(\bar{R}') \circledast h(\bar{R}') \tag{16}$$

where $\circledast$ denotes a three-dimensional convolution operation and $h(\bar{R}')$ is the three-dimensional Fourier transform of the sampling function $H(\bar{P})$.

For radar imaging applications, where it is impractical to illuminate the front and back side of the target as required above and in [8], Lewis [20] suggested treating the scattering object as symmetrical about the contour dividing its illuminated and dark regions. In this situation,

$$\rho[-\bar{p}(t)] = \rho[\bar{p}(t)] \tag{17}$$

and (21) is reduced to

$$\Gamma[\bar{p}(t)] = \frac{2\sqrt{\pi}}{k^2(t)(1 + \cos\alpha)} \operatorname{Re}\{\rho[\bar{p}(t)]\}. \tag{18}$$

Now we are in a position to determine which part of the $\bar{p}$ space is accessed by the data $\Gamma(\bar{p})$ recorded by means of the geometry of Fig. 1 when the incident illumination is a linear FM. From the definition of $\bar{p}(t)$ in (4) i.e., $\bar{p}(t) = k(t)(i_m - i_k)$, it is evident that for a fixed transmitter and receiver position, $|\bar{p}(t)|$ is linearly proportional to $k(t)$, the incident wavenumber. As the imaging chirp frequency increases, the wavenumber varies linearly from $k(T = 0) = k_1$ to $k(t = T) = k_2 = k_1(1 + \gamma T)$ and the vector $\bar{p}(t)$ assumes the values on a straight line from $\bar{p}(0) = k_1(i_m - i_k)$ to $\bar{p}(t) = k_2(i_m - i_k)$ in the direction $(i_m - i_k)$. Fig. 2 shows the position of this $\bar{p}$ space scan line when for convenience the center of the three-dimensional scatterer is chosen to coincide with the center of the three-dimensional $\bar{p}$ space. Figs. 3 and 4 show that when there are more than one receiver, $\Gamma(\bar{p})$ data is recorded along a group of $\bar{p}$ space scan lines each having a different directional vector $(i_m - i_k)$ depending on receiver position.

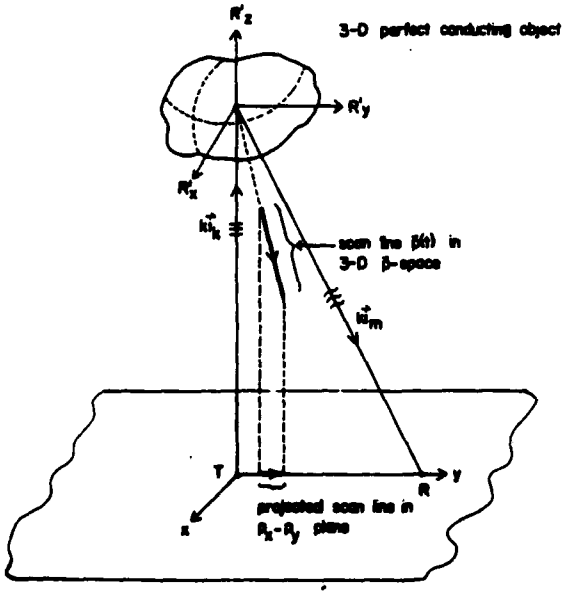

Fig. 2. Scan line $\bar{p}(t)$ in three-dimensional $\bar{p}$ space produced by FSI with receiver located at R and three-dimensional scatterer directly above transmitter T.

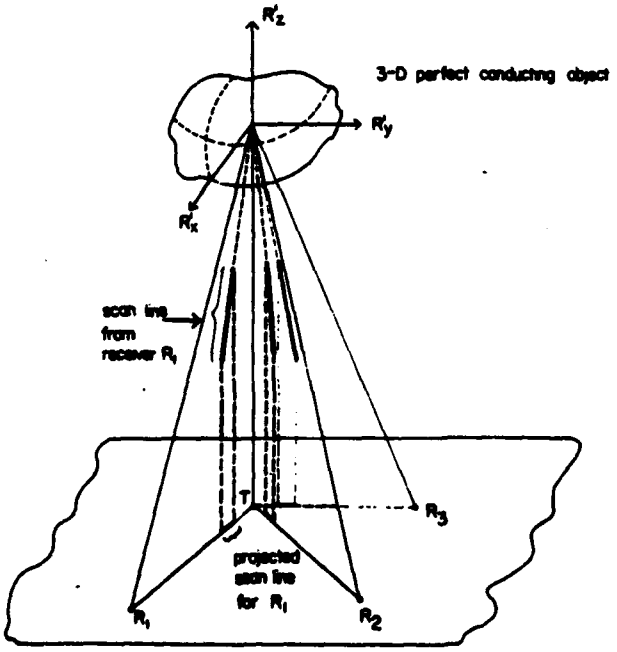

Fig. 3. $\bar{p}$-space scan lines generated from three receivers.

The result of this section shows graphically that frequency diversity techniques employing a two-dimensional array of receivers and one or more transmitters allow accessing a finite sampled volume in the three-dimensional Fourier space ($\bar{p}$ space) of the object. Inverse Fourier transformation of the acquired set of data $\Gamma(\bar{p})$ according to (15) should yield a three-dimensional diffraction limited image of $O(\bar{R})$ of the scattering perfectly conducting three-dimensional object.

In practice the acquisition of the three-dimensional data manifold $\Gamma(\bar{p})$ of (18) would involve coherent detection of the scattered field $E_s(\bar{R}, t)$ of (6) at each receiver location and correcting the measurement for the unequal phase shifts due

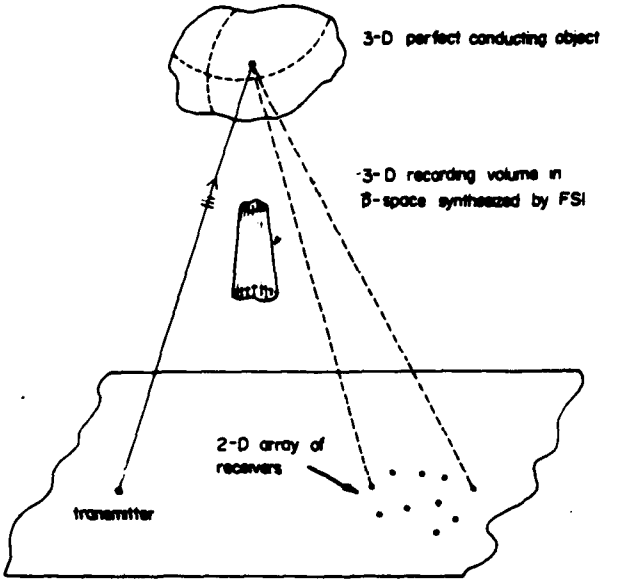

Fig. 4. Three dimensional $\bar{p}$ space accessed by frequency sweeping and two-dimensional array of receivers.

to propagation between the center of the object and each receiver. One convenient way of removing this range dependent phase in practice is to apply a target derived reference technique [34] suggested by Porter.

The three-dimensional resolution of the image $O_d(\bar{R}')$ depends on the three-dimensional extent of the $\bar{p}$ space data used in the three-dimensional inverse Fourier transform operation [33]. Specifically, resolution $\Delta R_z'$ in the R_z' direction depends roughly on Δp_z, the extent of H in the p_z direction as

$$\Delta R_z' = \frac{2\pi}{\Delta p_z} = \frac{2\pi}{[p_z(T) - p_z(0)]}. \tag{19}$$

Using the geometry in Figs. 1 and 2, it can easily be shown that $\Delta R_z'$ can be reduced to

$$\Delta R_z' = \frac{\lambda_2}{2\left(1 - \frac{\lambda_2}{\lambda_1}\right)\cos^2\left(\frac{\alpha}{2}\right)} \tag{20}$$

where λ_1, λ_2 are the longest and shortest wavelengths, of the transmitted chirp and α is the angle between the transmitter, the center of the target, and a receiver.

The resolutions in the R_x' and R_y' directions, however, depend roughly on the size of the area projected by the set of $\bar{p}$ lines defining H onto the p_x, p_y plane; i.e.,

$$\Delta R_x' = \frac{2\pi}{\Delta p_x} \qquad \Delta R_y' = \frac{2\pi}{\Delta p_y} \tag{21}$$

where Δp_x, Δp_y are the extents of p_x, p_y plane spanned by the projected $\bar{p}$ space data lines of the array of receivers. For the example of a single receiver situated along either the x or y axis, $\Delta p_{x,y} \cong (k_2 - k_1)\sin\alpha$. Thus

$$\Delta R_{x,y}' = \frac{2\pi}{\Delta p_{x,y}} = \left(\frac{1}{1 - \lambda_2/\lambda_1}\right)\left(\frac{1}{\sin\alpha}\right). \tag{22}$$

Equations (20) and (22) are general and applicable to the geometry of a circular array of receivers surrounding a central transmitter which is the geometry chosen in the simulation examples that will be described in Section VI of this paper.

If the echo, or specifically the object frequency response recorded by each receiver, is also sampled in time, then the three-dimensional $\bar{p}$ space data will only be recorded for a discrete grid of points in three-dimensional $\bar{p}$ space. Aliasing can be avoided if the Nyquist criterion is satisfied in each direction, i.e., if the target orthogonal dimensions or maximum extents are x_0, y_0, z_0, the number of sample points in each direction has to be

$$N_x \geq \frac{x_0}{\Delta R_x'} \qquad N_y \geq \frac{y_0}{\Delta R_y'} \qquad N_z \geq \frac{z_0}{\Delta R_z'}. \tag{23}$$

IV. FOURIER DOMAIN PROJECTION THEOREMS

It is shown in the previous sections that a three-dimensional Fourier transform operation applied to the recorded $\bar{p}$ space data should produce an image of the three-dimensional perfectly conducting scatterer. In practice, this three-dimensional image retrieval operation can be carried out digitally using fast Fourier transform (FFT) algorithms. However, even with the speed of the FFT, a three-dimensional FFT computation could be time consuming which could preclude real-time image reconstruction that is highly desirable in many instances. This leads to the question of whether or not coherent optical processing of the three-dimensional $\bar{p}$ space data is feasible. Since optical processing is carried out in parallel at the speed of light instead of a sequential fashion as in digital computers, a huge reduction of processing time can be expected. However, direct coherent optical processing of three-dimensional data is not feasible because of the inherent two-dimensional Fourier transform property of converging lenses [5], thus a scheme has to be developed to reduce the three-dimensional $\bar{p}$ space data to two-dimensional format before optical processing can be applied. The principle that allows a reduction of three-dimensional $\bar{p}$ space data to the two-dimensional format needed for image reconstruction is based on *Fourier domain projection theorems* (FDPT) [24], [26], [28]–[31]. In this section, the FDPT is outlined and extended to a *weighted* FDPT. It is shown that these theorems can be applied to the FSI problem to reconstruct images of three-dimenaional objects *tomographically*[1] slice by slice.

Let $O(\bar{R}')$ and $\Gamma(\bar{p})$ be the three-dimensional Fourier transform pairs as described in (12) and (13). Defining a projection of $\Gamma(\bar{p})$ onto the $p_x - p_y$ plane as

$$\Gamma_{\text{proj}}(p_x, p_y) = \int_{-\infty}^{\infty} \Gamma(\bar{p})\, dp_z \tag{24}$$

and $O_{\text{proj}}(R_x', R_y')$ as the two-dimensional transform of $\Gamma_{\text{proj}}(p_x, p_y)$, we obtain,

$$O_{\text{proj}}(R_x', R_y') = \int\int_{-\infty}^{\infty} \Gamma_{\text{proj}}(p_x, p_y) \cdot e^{-j(p_x R_x' + p_y R_y')}\, dp_x\, dp_y \tag{25}$$

$$= \int\int\int_{-\infty}^{\infty} \Gamma(\bar{p}) e^{-j(p_x R_x' + p_y R_y')} \cdot dp_x\, dp_y\, dp_z \tag{26}$$

$$= O(R_x', R_y', R_z' = 0). \tag{27}$$

[1] Tomography comes from the Greek word *tomos* meaning slice.

Equation (27) shows that by projecting the three-dimensional $\bar{p}$ space data onto a given plane, the two-dimensional transform of the projected data, which we refer to as a *projection hologram*, gives an image of a central cross sectional slice of the object parallel to that plane. In the case of perfectly reflecting objects, the slice is actually a cross sectional outline of the object. If $\Gamma(\bar{p})$ is multiplied by a weighting function of the form $e^{-j\beta p_z}$ before performing the projection, i.e.,

$$\Gamma_{\beta,\text{proj}}(p_x, p_y) = \int_{-\infty}^{\infty} \Gamma(\bar{p}) e^{-j\beta p_z}\, dp_z, \tag{28}$$

then it can readily be shown that the two-dimensional inverse transform of $\Gamma_{\beta,\text{proj}}(p_x, p_y)$ gives

$$O_{\beta,\text{proj}}(R_x', R_y') = O(R_x', R_y', R_z' = \beta). \tag{29}$$

It is evident from (27) that by multiplying $\Gamma(\bar{p})$ with an exponential weighting factor before performing the projection operation, cross sectional outlines of $O(\bar{R}')$ can be obtained at planes other than $R_z = 0$ that are selected through the parameter β. Since this weighting function is introduced after the recording of the scattered data, parallel slices of the three-dimensional object $O(\bar{R})$ can be reconstructed slice by slice by changing the parameter β.

V. COMPUTER SIMULATION RESULTS FOR FSI

In this section computer simulation examples are presented to demonstrate the FSI theories developed in the previous sections. Both extended and point scatterer objects are considered in the simulations. For the examples presented, the receivers are positioned along an arc of a circle with the transmitter situated at the center of the circle. This geometry is chosen because of its practical potential and for the simplicity in positioning of the intensity modulated projected scan lines of the resulting projection holograms on the computer display. The simulated far field recorded by each receiver generates a scan line of data in the three-dimensional $\bar{p}$ space. These scan lines are projected onto the p_x, p_y plane in accordance to the weighted FDPT. Optical two-dimensional Fourier transforms of the resulting weighted projection holograms are carried out, and optical images of various slices of the three-dimensional objects are recorded in the image plane. Since far-field data for a perfectly conducting sphere can be calculated exactly for different aspect angles and frequencies using the Mie series formulation [21], spheres were good candidates for use as three-dimensional extended objects in the simulation.

The simulation geometry of FSI of two adjoining perfectly conducting spheres is shown in Fig. 5. The two spheres are assumed each to be one meter in diameter, and each is offset by a distance of 50 cm from the R_x' axis. Fifty receivers forming an arc from $\phi = 25°$ to $155°$ with $2.5°$ angular spacing is assumed. The ratio of Z_0/Rg is 2, thus $\alpha = \tan(Rg/Z_0) = 26.6°$.

The frequency sweep display was limited by the resolution capability of the computer display and covered a 2–4-GHz range consisting of 100 equally spaced frequency points. The scattered far field recorded by each receiver is assumed to be a superposition of the field of two independent spheres. This assumption is valid under the Born approximation, i.e., when multiple scattering between the two spheres can be ignored. Using (20) and (22), the resolutions are approximately $\Delta R_z' = 7.7$ cm and $\Delta R_x' = \Delta R_y' = 33.5$ cm.

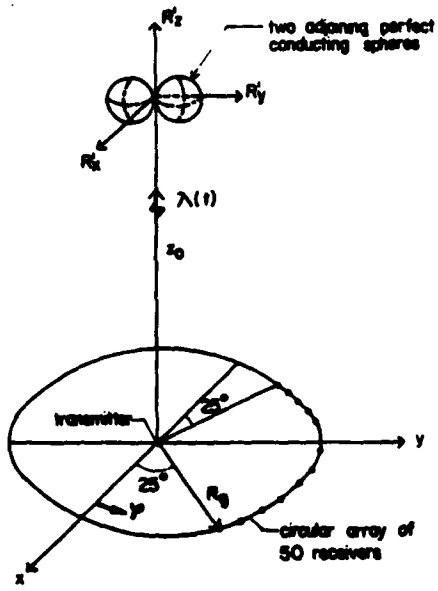

Fig. 5. Geometry used in FSI of object consisting of two perfectly conducting spheres.

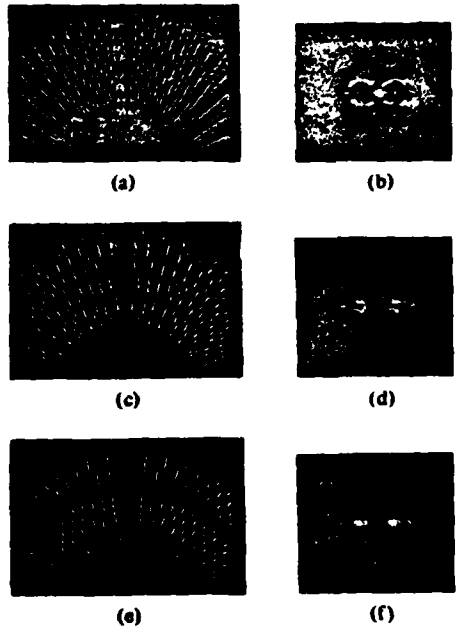

Fig. 6. Projection holograms (left) of object consisting of two adjoining spheres and optical reconstruction of corresponding central cross sectional slices through two spheres (right).

Fig. 6 shows the simulation results for a β equal to 0, 30, and 40 cm; this is equivalent to producing images of slices through the two spheres at parallel planes equal to $R_z' = 0$, 30, and 40 cm, respectively. The weighted projected holograms for the three cases are shown in Fig. 6(a), (c), and (e), and the corresponding optical reconstructions using the optical bench arrangement shown in Fig. 7 are presented in Fig. 6(b), (d), and (f). These reconstructions clearly illustrate the ability to retrieve images of parallel cross sectional outlines of a three-dimensional scatterer from the same set of $\bar{p}$ space data utilizing the weighted Fourier domain projection theorem.

In a second example shown in Fig. 8, an object consisting of a set of scatterers each of which is too small to be resolved by the imaging system was assumed. The geometry for this simulation example is identical to that of Fig. 5 except that the number of receivers in this case is reduced to 16 equally spaced along an arc from $\phi = 40^\circ$ to $\phi = 77.5^\circ$ with 25° angular spacing between adjacent receivers. The value of $\Gamma(\bar{p})$ for the test object of Fig. 8 as obtained from (28) is

$$\Gamma(\bar{p}) = 1 + e^{-jp_x x_0} + e^{-jp_y y_0} + e^{j(p_y y_0 + p_z z_0)} \cdot (1 + 2\cos p_x x_0) + 2e^{-j(p_y y_0 + p_z z_0)} \cos p_x x_0. \tag{30}$$

$\Gamma(\bar{p})$ is multiplied by a phase term $e^{-j\beta p_z}$ with $\beta = -z_0$, 0, z_0, respectively, before the projection operations is performed to generate the weighted projection holograms shown to the left in Fig. 9(a), (b), (c), respectively.

Optically reconstructed images of this set of holograms clearly show that slices of the objects at different parallel planes perpendicular to the direction of projection can be imaged individually using the weighted Fourier domain projection theorem. When the reconstructed images in Fig. 9 are compared to the geometry of the object in Fig. 8, it becomes evident that the relative locations of the scatterers in different R_z' planes are also preserved in the reconstruction. The bright regions in the left upper and right lower portions of the images are results of diffraction by spokelike sampling format in the projection holograms in Fig. 9. Unlike the previous example, an appropriate spatial carrier has been included in each projection hologram to separate each image from its conjugate and from the zero order light. The presence of both a primary and a conjugate image in each reconstruction is a well-known consequence of the optical Fourier transform when the input function, the hologram transmittance, is positive real [5]. Such a spatial carrier was not included in the projection holograms for two spheres in the preceeding example, and as a result the primary and conjugate images of the circles were on-axis and superimposed. Because of object symmetry, however, this superposition was acceptable.

VI. CONCLUSION

This work was initiated to study the possibility of extending the concept of frequency sweeping to the imaging of three-dimensional objects. It was found that a three-dimensional Fourier transform relationship exists between the shape of a three-dimensional perfect conducting object and its scattered far field. By recording this scattered field at different aspect angles and frequencies by means of arrays of coherent receivers and transmitters, the processed data can be inverse transformed to obtain a three-dimensional image of the object. This result turned out to be a generalization of Bojarski's and Lewis' formulation of inverse scattering to the multistatic case. For stationary objects, the scattered field at different aspect angles can be recorded by just one transmitter and an array of receivers, whereas in the monostatic T/R (transmitter/receiver) configuration considered by Bojarski and Lewis, an array of monostatic T/R's has to be used to record the backscattered field in order to obtain the same amount of information. In the case of nonstationary

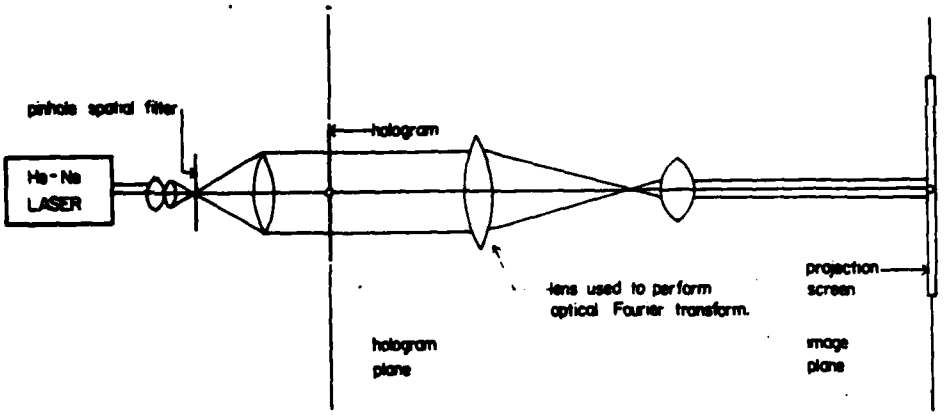

Fig. 7. Optical bench configuration.

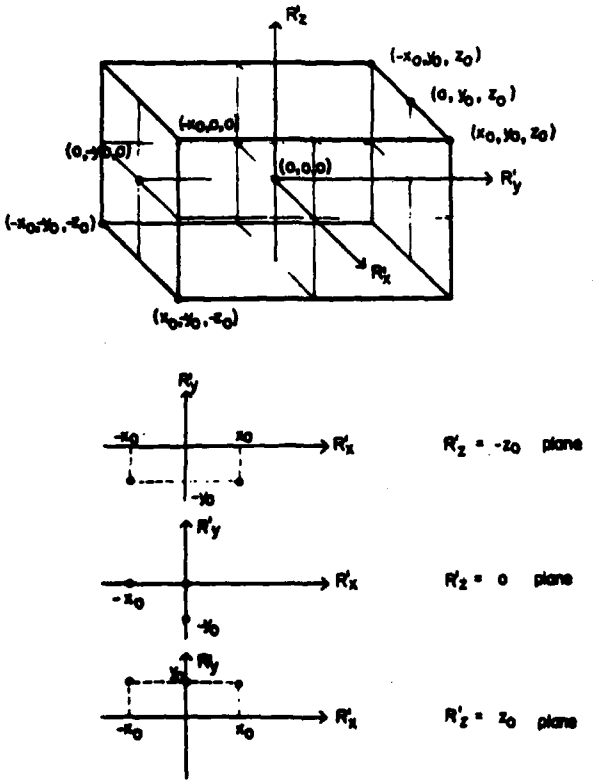

Fig. 8. Three-dimensional object consisting of set of eight point scatterers shown in isometric and $R_x' - R_y'$ plane of views at $R_z' = -z_0, 0, z_0$. $x_0 = y_0 = z_0 = 100$ cm.

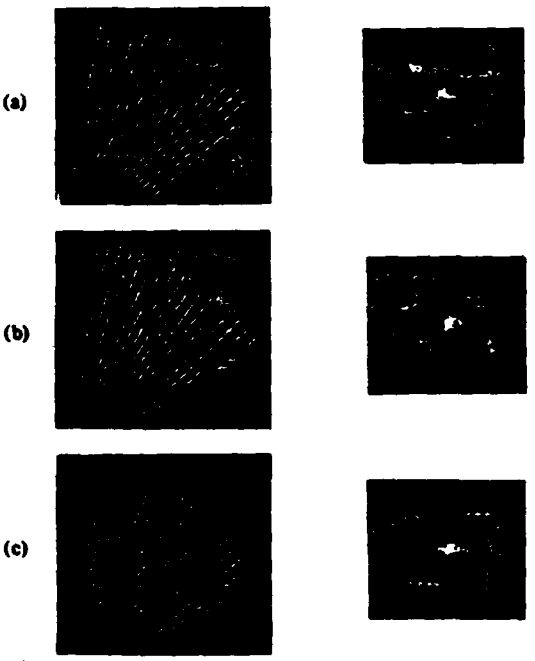

Fig. 9. Projection holograms and their optical reconstruction for set of point scatterers in Fig. 8 at different R_z' planes. (a) Hologram and reconstructed image of scatterers at $R_z' = -z_0$ plane. (b) Hologram and image at $R_z' = 0$ plane. (c) Hologram and image at $R_z' = z_0$ plane. $x_0 = y_0 = z_0 = 100$ cm.

objects, although a monostatic T/R can collect scattered field at different aspect angles as a result of object motion or rotation, more information can be collected in a shorter time if a multistatic geometry consisting of one (or more) transmitters and an array of receivers is employed. By utilizing the Fourier domain projection theorem and the weighted Fourier domain projection theorem, it was shown that coherent optical systems can be used to reconstruct images of separate slices of a distant object establishing thus for the first time the feasibility of a tomographic radar.

Computer simulations were performed to verify the frequency swept imaging theory and the Fourier domain projection theorems for both continuous extended objects and objects consisting of several point scatterer. The optically reconstructed images from these simulations clearly demonstrate the validity of the concepts developed in this paper and establish the feasibility of superresolved three-dimensional imaging by means of broad-band cost-effective apertures. The concepts developed are applicable to all methods by which the multiaspect frequency responce (namely, $\Gamma(\bar{p})$ in (18)) can be measured either directly by frequency diversity as discussed in this paper or indirectly via the impulse response or correlation measurement with noise illumination [11]. The choice of any of these approaches will depend on the imaging application, ease of implementation, and the ease with which the data recorded at each receiver can be corrected for propagation delay between transmitter, object, and the particular receiver as with the target derived reference method referred to in this paper.

REFERENCES

[1] S. A. Schelkunoff, "A mathematical theory of linear arrays," *Bell Syst. Tech. J.*, vol. 22, pp. 80–107, 1943.

[2] D. Slepian and H. O. Pollak, "Prolate spheroidal wave functions, Fourier analysis and uncertainty—I," *Bell Syst. Tech. J.*, vol. 40, pp. 43–64, 1961.

[3] C. W. Barnes, "Object resolution in diffraction limited imaging systems," *J. Opt. Soc. Amer.*, vol. 56, pp. 575–578, May 1966.

[4] C. K. Rushforth and R. W. Harris, "Resolution, restoration and noise," *J. Opt. Soc. Amer.*, vol. 58, pp. 539–545, Apr. 1968.

[5] J. W. Goodman, *Introduction to Fourier Optics*. New York: McGraw-Hill, 1968.

[6] A. P. Anderson and J. C. Bennet, "Feasibility of enhanced microwave image resolution using a super-directive aperture," *Proc. IEEE* (Lett.), vol. 64, pp. 376–378, Mar. 1976.

[7] H. Nassenstein, "Superresolution by diffraction of subwaves," *Opt. Commun.*, vol. 2, pp. 231–234, Oct. 1970.

[8] A. Bachl and W. Lukosz, "Experiments on superresolution imaging of a reduced object field," *J. Opt. Soc. Amer.*, vol. 57, pp. 163–169, Feb. 1967.

[9] C. W. Chuang and D. L. Moffatt, "Natural resonance of radar targets via Prony's method and target discrimination," *IEEE Trans. Aerosp. Electron. Syst.*, vol. AES-12, pp. 583–589, Sept. 1976.

[10] E. M. Kennaugh and D. L. Moffatt, "Transient and impulse response approximations," *Proc. IEEE*, vol. 53, pp. 893–901, 1965.

[11] N. H. Farhat, "Principles of broad-band coherent imaging," *J. Opt. Soc. Amer.*, vol. 67, pp. 1015–1021, Aug. 1977.

[12] R. Harger, *Synthetic Aperture Radar Systems: Theory and Design*. New York: Academic, 1970.

[13] J. J. Kovaly, *Synthetic Aperture Radar*. Dedham, MA: Aertech House, 1976.

[14] N. H. Farhat, "High resolution microwave holography and imaging of remote moving objects," *Opt. Eng.*, vol. 14, pp. 499–505, Sept.–Oct. 1975.

[15] ——, "Frequency synthesized imaging apertures," in *Proc. 1976 Optical Computing Conf.*, IEEE Cat. 76, CH1100-76., pp. 19–24.

[16] A. Jain, "Electronic imaging and scanning," *Appl. Opt.*, vol. 16, pp. 550–553, Mar. 1977.

[17] D. C. K. Chan *et al.*, "New results in computer simulated frequency swept imaging," *Proc. IEEE* (Lett.), pp. 1214–1215, Aug. 1977.

[18] N. Bojarski, "Inverse scattering," Naval Air Command Final Rep., Rep. N000 19-73-C-0312F, Feb. 1974.

[19] R. M. Lewis, "Physical optics inverse diffraction," *IEEE Trans. Antennas Propagat.*, vol. AP-17, pp. 308–314, May 1969.

[20] S. R. Raz, "On scatterer reconstruction from far-field data," *IEEE Trans. Antennas Propagat.*, pp. 66–70, Jan. 1976.

[21] R. F. Harrington, *Time-Harmonic Electromagnetic Fields*. New York: McGraw-Hill, 1961.

[22] ——, "On scattering by large conducting bodies," *IRE Trans. Antennas Propagat.*, pp. 150–153, Apr. 1957.

[23] G. Wade, "Acoustic echo computer tomography," presented at the 8th Symp. Acoustical Imaging, Key Biscayne, FL, May 1978.

[24] R. N. Bracewell, "Strip integration in radio astronomy," *Aust. J. Phys.*, vol. 9, pp. 198–217, 1956.

[25] ——, "Inversion of fan-beam scans in radio astronomy," *Astrophys. J.*, vol. 150, pp. 427–434, Nov. 1967.

[26] R. A. Crowther *et al.*, "The reconstruction of a three dimensional structure from projections and its applications to electron microscopy," *Proc. Roy. Soc. Lond.*, A.317, pp. 319–340, 1970.

[27] G. Devey and P. Wells, "Ultrasound in medical diagnosis," *Sci. Amer.*, pp. 98–112, May 1978.

[28] W. Swindell and H. Barrett, "Computerized tomography: Taking sectional X-rays," *Phys. Today*, pp. 32–41, Dec. 1977.

[29] G. W. Stroke *et al.*, "Image improvement and three dimensional reconstruction using holographic image processing," *Proc. IEEE*, vol. 65, pp. 39–62, Jan. 1977.

[30] G. W. Stroke and M. Halioua, "Three dimensional reconstruction in X-ray crystallography and electron microscopy by reduction to two dimensional holographic implementation," *Trans. Amer. Crystallograph. Assoc.*, vol. 12, pp. 27–41, 1976.

[31] G. W. Stroke *et al.*, "Imaging of atoms: Three dimensional molecular structure reconstructions using opto-digital computing," *Proc. IEEE* (Lett.), vol. 65, pp. 589–591, Apr. 1977.

[32] N. H. Farhat and C. K. Chan, "Three dimensional imaging by wave-vector diversity," presented at 8th Symp. Acoustical Imaging, Key Biscayne, FL, May 1978. Published in *Acoustical Imaging*, vol. 8, A. Metherell, Ed. New York: Plenum, 1979.

[33] C. K. Chan, "Analytical and numerical studies of frequency swept imaging," Ph.D. thesis, *Univ. Pennsylvania*, Dec. 1978.

[34] R. P. Porter, "A radar imaging system using the object to provide the reference signal," *Proc. IEEE* (Lett.), vol. 59, pp. 307–308, Feb. 1971.

[35] G. Graf, "High resolution imaging of radar targets with microwaves," in *Military Microwaves Conf. Proc.* Microwave Exhibitors and Publishers, 1978, pp. 295–302.

Chi K. Chan (S'77–M'78) was born in Hong Kong on January 17, 1951. He received the S.B. and S.M. degrees from the Massachusetts Institute of Technology, Cambridge, in 1974 and the Ph.D. degree from the University of Pennsylvania, Philadelphia, in 1978.

In 1978 he joined M.I.T.'s Lincoln Laboratory where his current research work includes synthetic aperture radar imaging and digital signal processing.

Dr. Chan is a member of Etta Kappa Nu, Tau Beta Pi, and Sigma Xi.

Nabil H. Farhat (S'58–M'63–SM'75–F'81) received the B.Sc. degree in 1957 from the Technion-Israel Institute of Technology, Haifa, the M.Sc. degree in 1959 from the University of Tennessee, Knoxville, and the Ph.D. degree in 1963 from the University of Pennsylvania, Philadelphia, all in electrical engineering.

In 1964 he joined the faculty of the Moore School of Electrical Engineering, University of Pennsylvania, where he is now Professor in Electrical Engineering and heads the Electro-Optics and Microwave-Optics Laboratory. His current research interests are in the areas of imaging radars, microwave holography, and electrooptics in which he has numerous publications. He is teaching courses in EM theory, electrooptics, and holography on both graduate and undergraduate levels. His past research included the study of the interaction of EM radiation with plasmas and solids in the context of laser output energy measurement and photodetachment of negative ions. He has been an RCA Consultant since 1969. He has served as Editor of *Advances in Holography* and is Associate Editor of *Acoustical Imaging and Holography*. He is currently engaged in the preparation of two texts: *An Introduction to Electro-Optics* and *Microwave Holography-Theory and Applications*. While Associate Professor, he was named to the Ennis Chair in Electrical Engineering. He is a recipient of the University of Pennsylvania Christian R. and Mary F. Lindback Foundation Award for distinguished teaching.

Dr. Farhat is a member of Sigma Xi, Eta Kappa Nu, the New York Academy of Science, the American Institute of Physics, the American Society for the Advancement of Science, and has served on the National Board of Directors of Eta Kappa Nu.

APPENDIX V

INVERSE SCATTERING RECONSTRUCTION FROM INCOMPLETE FOURIER-SPACE DATA

(Paper Presented at the 1983 OSA/AFOSR Winter Topical Meeting on Signal Recovery and Synthesis - Incline Village, Nevada and published in Conference Digest.)

Inverse Scattering Reconstructions From Incomplete Fourier Space Data

N.H. Farhat
University of Pennsylvania
Electro-Optics and Microwave-Optics Laboratory
The Moore School of Electrical Engineering
200 S. 33rd St., Philadelphia, Pa. 19104

ABSTRACT

We show that 3-D tomographic inverse scattering reconstruction of a scattering object is obtainable from data lying on a curved surface, rather than within a volume, of its accessed Fourier space as would ordinarily be required.

I. Introduction

It is known from inverse scattering theory [1]-[4], that multiaspect *monostatic* or *bistatic* coherent measurement of the far field scattered by a plane-wave illuminated conducting or non-dispersive object under conditions that satisfy the *physical optics* and Born approximations can be used to access the 3-D Fourier space $\Gamma(\bar{p})$ of the object *scattering function* $\gamma(\bar{r})$. Here $\bar{r}$ is a 3-D position vector in object space measured relative to a common origin in the object or its vicinity and $\bar{p} = k\,(\bar{l}_R - \bar{l}_i)$ is a 3-D position vector in Fourier space or $\bar{p}$-space with $\bar{l}_R$ and $\bar{l}_i$ being unit vectors in the directions of observation and incident illumination respectively and k is the wavenumber of illumination. The scattering function $\gamma(\bar{r})$ represents the 3-D geometrical distribution and strengths of those visible *scattering centers* or *differential scattering cross-sections* of the body that give rise to the measured field. Correction of the field measured in practice in this fashion for range-phase, clutter, and system response [5],[6] leads to accessing $\Gamma(\bar{p})$ over those values of $\bar{p}$ employed in the measurement. We will designate the measured data manifold by $\Gamma_m(\bar{p})$ and assume without further elaboration here that the values of $\bar{p}$ utilized always sample the $\bar{p}$-space in a manner satisfying the Nyquist criterion to avoid aliasing in the reconstruction. The size and shape of the accessed Fourier region depends on geometry and on the extent of the spectral and angular apertures utilized i.e., on the values k and $(\bar{l}_R, \bar{l}_i)$. It is possible then as shown by computer simulation in [3] and [4] to retrieve tomographically a *diffraction and noise limited* version $\gamma_d(\bar{r})$ of the object scattering function through application of the *Projection-Slice Theorem* derivable from the multi-dimensional Fourier transform [7]-[10].

The aim of this paper is to show that high resolution reconstruction of $\gamma_d(\bar{r})$ is possible by measuring $\Gamma_m(\bar{p})$ over a curved surface in $\bar{p}$-space rather than within a volume as would ordinarily be required for the retrieval of 3-D detail of $\gamma_d(\bar{r})$. Because, for a given fixed spectral range, the number of angular observation points needed to adequately sample the $\bar{p}$-space over a volume is considerably higher than the number needed to access the outer surface of the volume or a portion of it, a sizable reduction in the number of coherent sensors or receivers is achieved. In practice this translates into a proportionate reduction in the projected cost of high resolution wavelength diversity imaging apertures and would for example, open the way for cost-effective implementation of envisioned [11] giant *imaging radar networks*.

II. Theoretical Considerations

Let $H(\bar{p})$ be a Fourier space sampling function describing the values assumed by the vector $\bar{p} = k(\bar{l}_R - \bar{l}_i)$ during data acquisition. We can express then the Fourier space data manifold accessed by measurement as,

$$\Gamma_m(\bar{p}) = \Gamma(\bar{p})\, H(\bar{p}) \tag{1}$$

which can be regarded as a 3-D *Fourier transform hologram* of the scattering object. A diffraction and noise limited version $\gamma_d(\bar{r})$ of the object function $\gamma(\bar{r})$ can be obtained by Fourier inversion of eq. (1). That is (within a constant $1/(2\pi)^3$),

$$\gamma_d(\bar{r}) = \int \Gamma(\bar{p})H(\bar{p})\, e^{-j\bar{p}\cdot\bar{r}}\, d\bar{p} = \gamma(\bar{r}) *** h(\bar{r}) \tag{2}$$

where

$$h(\bar{r}) = \int H(\bar{p})\, e^{-j\bar{p}\cdot\bar{r}}\, d\bar{p} \tag{3}$$

is the 3-D *impulse response* or *point spread function* of the system and the triple asterisks denote a 3-D convolution. Clearly, because $H(\bar{p})$ (which can be now identified also as a 3-D *transfer function* of the system) is dependent on recording geometry through $\bar{p} = k(\bar{l}_R - \bar{l}_i)$, the impulse response here, in contrast to conventional monochromatic imaging systems, is *spatially variant*. A valid question then is the identification of favorable recording geometries for which a narrow $h(\bar{r})$ is realized for a wide range of object bearings utilizing a minimum number of observation and/or illuminating points i.e., $(\bar{l}_R, \bar{l}_i)$ values in order to keep to a minimum the number of broadband coherent receivers and transmitters employed in the recording geometry. To provide an answer to this question we apply the projection-slice theorem to eq. (3). There are two forms of this theorem. One states that a projection (central slice) in Fourier space and a central slice (projection) in object space are a Fourier transform pair. The second form establishes a similar relationship between parallel *weighted projections* and parallel slices in the two domains [3],[9]. In the context of this analysis, the first version means that the 2-D Fourier transform of the projection of $H(\bar{p})$ on an arbitrarily oriented plane in p-space is a central slice through $h(\bar{r})$ oriented parallel to the projection plane. This immediately suggests that desirable recording geometries are those for which the projection of their $H(\bar{p})$ in any direction cover always extended areas whose 2-D Fourier transform will necessarily be concentrated in a narrow region indicating an $h(\bar{r})$ with central slices exhibiting peak amplitudes of narrow extent. If all central slices of $h(\bar{r})$ possess peaks of narrow extent the 3-D impulse response $h(\bar{r})$ will consequently be narrow. With this condition established, we consider next the two bistatic recording geometries shown in Fig. 1. In one (a) a randomly or regularly sampled circular recording aperture of diameter D is used to access a truncated conical volume in p-space with the truncation being set by the initial and final values of the range of wavenumbers k utilized in the measurement. In the second geometry (b), a number of random or equally spaced sampling points or coherent receivers distributed in a circle of diameter D are employed to access an identically shaped hollow truncated cone. Both geometries assume a centrally located coherent transmitter or illuminator T. The sampling functions $H(\bar{p})$ realized in both cases will coincide over the sidewalls of the truncated cones. A brief study of the two cases reveals that the shape and extent of the areas covered by nearly all projections of the solid truncated cone and the hollow truncated

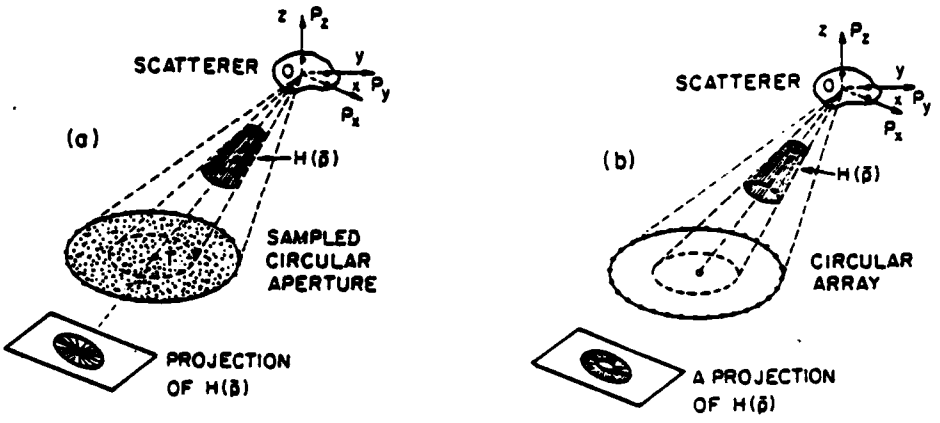

Fig. 1. Geometries for accessing the Fourier space of a 3-D scatterer. (a) with a sampled 2-D circular aperture, (b) with a circular array of sampling points.

cone are the same except for a few projections in those directions forming a small solid angle surrounding the OT Line where the hollow nature of $H(\bar{p})$ in (b) will be evidenced by a missing central region. This difference is illustrated by the two projection examples included in Fig. 1. However, because the outer boundaries of comparable projections of $H(\bar{p})$ in (a) and (b) are identical, the associated Fourier transforms representing the slices of $h(\bar{r})$ for both geometries are expected to possess central peaks of the same extent. The amplitude and shape of side-lobe structure in the outlying regions surrounding the central peaks will however differ somewhat because of the different number and distribution of data points in the comparable projections. It can be concluded therefore that the 3-D resolutions obtained with data accessed over a volume of $\bar{p}$-space and with data accessed over the outer surface of the volume are nearly the same. Verification of this conclusion is found in the results of a numerical simulation of microwave wavelength diversity imaging [3] which are presented in Fig. 2. A semi-circular array of sampling points consisting of 50 equally spaced receivers distributed over an arc of 130° as depicted in Fig. 2(a) is assumed. A 3-D test object consisting of two adjoining 1m diameter conducting spheres arranged as shown and centered at a distance R directly above the transmitter T is chosen. A spectral range of (2-4) GHz and a ratio of R/D =1 are assumed in computing $\Gamma_m(\bar{p})$. The far field scattered by the two spheres was computed using the Mie series formulation [12]. Weighted parallel projections in the direction p_z of the accessed $\bar{p}$-space data manifold lying on a truncated semi-conical surface represented by $H(p)$ in Fig. 2(a) were obtained by multiplying $\Gamma_m(\bar{p})$ by the complex factor $\exp j(\alpha p_z)$, $\alpha = 0$, -30cm, -40cm, before computing the projections. This yields three weighted projection holograms shown to the left in Fig. 2(b) that correspond from top to bottom to parallel horizontal slices through the object in Fig. 2(a) at $z = 0$, -30cm and -40cm. The optically retrieved images from these projection holograms are shown to the right in Fig. 2(b). These demonstrate clearly the 3-D tomographic imaging capability from the limited p-space data accessed by the geometry of Fig. 2(a).

III. Acknowledgement

This research was supported by the Army Research Office under contract DAAG-29-80-K-0024P02 and by the Air Force Office of Scientific Research, Air

Force Systems Command under grant AFOSR-81-0240B.

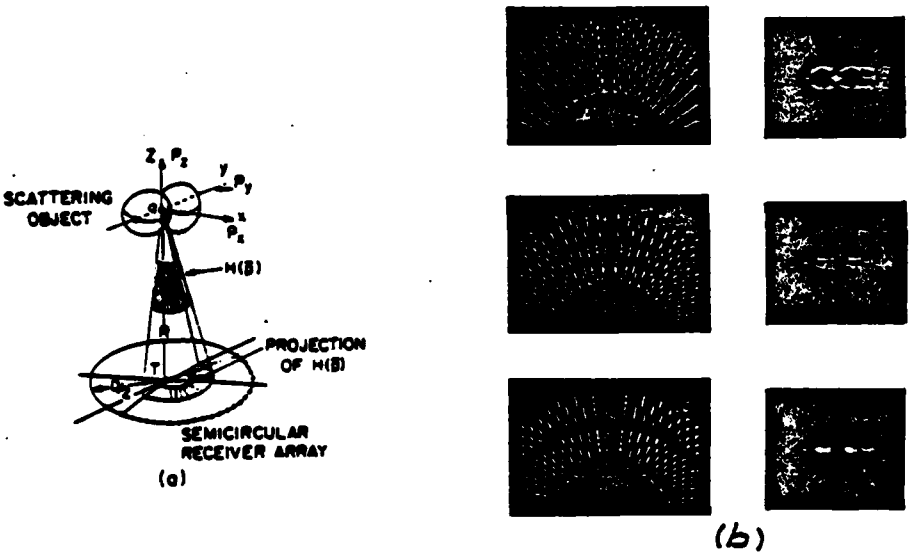

Fig. 2. Details of numerical simulation of 3-D tomographic image reconstruction from limited Fourier space data. (a) Recording geometry (b) Weighted projection holograms (left) and retrieved images of three slices through the illuminated portion of the two spheres.

References

1. N. Bojarski, Naval Air Command Final Report, N00019-73-C-0312F, Feb. 1974.
2. R.M. Lewis, IEEE Trans. on Ant. and Prop., Vol. AP-17, pp. 308-314, May 1969.
3. C.K. Chan and N. Farhat, IEEE Trans. on Ant. and Prop., Vol. AP-29, pp. 312-319, March 1981.
4. N.H. Farhat and C.K. Chan, "Three-Dimensional Imaging by Wave-Vector Diversity", Presented at the 8th Int. Symp. on Acoust. Imaging, Key Biscayne, Fla. 1978, and published in *Acoustical Imaging*, Vol. 8, A. Metherell (Ed.), pp. 499-516, Plenum Press, New York 1980.
5. N.H. Farhat and C.L. Werner, "An Automated Microwave Measurement Facility For Three-Dimensional Tomographic Imaging by Wavelength Diversity", Presented at the 1981 Intern. IEEE AP-S Symp./Nat. Radio Science Meeting, L.A., June 1981.
6. N.H. Farhat, C.L. Werner and T.H. Chu, "Microwave Projection Imaging With Near Optical Resolution", Submitted for publication, IEEE Trans. on Ant. and Propagation.
7. J. Radon, Ber. Saechs. Akad. Wiss. (Leipzig), Vol. 19, pp. 262-278, 1917.
8. R.N. Bracewell, Australian J. of Phys., Vol. 9, pp. 198-217, 1951.
9. G. Stroke and M. Halioua, Trans. Amer. Crystal. Assoc., Vol. 12, pp. 27-41, 1976.
10. H.H. Barrett and W. Swindle, *"Radiological Imaging:Theory and Image Formation, Detection and Processing,* Acad. Press, New York, 1982.
11. N.H. Farhat, W.I. Landauer and W.E. Wallace, "Computer Assisted Naval Applications of Holography", Computer Command and Control Co., Report No. 132-4, prepared for the Naval Analysis Program, Office of Naval Research, under contract N0014-69-C-0167, Feb. 1973.
12. R.F. Harrington, *"Time Harmonic Electromagnetic Fields,* McGraw-Hill, 1961.

APPENDIX VI

PROJECTION THEOREMS AND THEIR APPLICATION IN MULTIDIMENSIONAL SIGNAL PROCESSING

(Reprint of paper presented at the 1983 SPIE Technical Symposium on Advances in Optical Information Processing, L.A., Jan. 1983)

be presented at the 1983 SPIE LA/'83

Projection theorems and their application in multidimensional signal processing

N.H. Farhat, C. Yi Ho and Li Szu Chang

University of Pennsylvania, Electro-Optics and Microwave-Optics Laboratory
The Moore School of Electrical Engineering, Philadelphia, PA., 19104

Abstract

Several sophisticated imaging methods are based on measurements that lead to accessing a finite volume of the 3-D Fourier domain of an interrogated object and subsequent retrieval of 3-D image detail by 3-D Fourier inversion. Examples are found in *inverse scattering, integral holography, x-ray and radio-emission imaging, crystalography,* and *electron microscopy*. This paper examines a unified approach to all these methods, namely through reduction of dimensionality based on the *projection-slice* property of the multidimensional Fourier transform. We describe two hybrid (opto-digital) computing schemes, one employing coherent light and the other incoherent light, that can be used with these techniques to reconstruct and display true 3-D image detail tomographically. Reduction of dimensionality is shown to provide flexibility in hybrid (opto-electronic) computing by permitting trade-off between the degree of parallel and serial processing employed. It leads to new architectures capable of enhanced throughput and dynamic range and extends the domain of optical computing beyond one and two dimensional signals.

1. Introduction

Inverse methods involve inferring information about the geometrical and material properties of an object by remote probing with electromagnetic, acoustic, or particle beams. Several inverse methods for example in optics [1]-[8], microwaves [9]-[13], crystalography and electron microscopy [14], computerized axial tomography [15], ultrasonics [16] and integral holography [17] lead to accessing a finite volume in the 3-D Fourier space of the object and subsequent retrieval of 3-D image detail via 3-D Fourier inversion. The required 3-D Fourier transform can naturally be carried out digitally by means of a 3-D fast Fourier transform algorithm. This approach may not be fast enough for certain applications even with the fastest array processors available today especially when one is dealing with the large amounts of data associated with complicated objects. This can prevent real-time image reconstructions and display. Furthermore the inherent two dimensionality of present day computer displays precludes true 3-D image display limiting the presentation of 3-D image detail to perspectives, individual slices or cross-sectional outlines.

To overcome these limitations several techniques for 3-D display of television and computer generated signals have been proposed and demonstrated [18]-[20].

In this paper we consider a new approach to true 3-D image reconstruction and display. Two methods that employ hybrid (opto-digital) computing and do not require viewing aids are described. Both methods are based on reducing a 3-D Fourier space manifold into a series of 2-D *projection holograms* each corresponding to a different parallel slice of the object and on using the optical 2-D Fourier transform in a space-time multiplex scheme to retrieve rapidly and sequentially images of the various slices. The reconstructed slices are displayed on an oscillating screen in the proper sequence to form the 3-D image *tomographically*. One method employs coherent optical computing to perform the required 2-D Fourier transforms while a novel incoherent opto-electronic computing scheme based on spatial domain projections is employed in the other.

The processing of multi-dimensional signals by reduction of dimensionality via projection was first considered by Radon [21]. Since then projection methods have been employed in the processing of 2-D radio-astronomical data by Bracewell [22],[24] and in hybrid (opto-digital) processing of 3-D data by Stroke, Halioua, and co-workers [14],[16],[24] in the context of crystallography, electron microscopy and ultrasonics and by Farhat and Chan [12],[13] and Das and Boerner [41] in the context of 3-D microwave imaging and radar shape estimation.

Comprehensive treatments and applications of multidimensional signals processing via projections has been given by Mersareau and Oppenheim [25] in the context of digital signal processing and more recently by Barrett [26]-[28] and Farhat [29] in the context of optical data processing.

2. The projection-slice theorem

The principle underlying the two hybrid 3-D image reconstruction and display techniques discussed in this paper is the *projection-slice theorem* associated with the multidimensional Fourier transform [22],[23]. Given a multidimensional object function and its Fourier transform the projection-slice theorem states that a projection (slice) in Fourier space and a "parallel" slice (projection) in object space are a Fourier transform pair. In other words projections in object space correspond, in the Fourier transform sense, to "parallel" slices

in Fourier space taken in planes parallel to the projection planes and visa versa, i.e., projections in Fourier space correspond in the Fourier transform sense to "parallel" slices in object space.

There are two forms of the projection-slice theorem. One form deals with *meridional* or *central* slices and corresponding projections on planes parallel to them, while the second form deals with weighted parallel projections made always on the same plane and corresponding slices at different depth all parallel to the one projection plane.

A derivation of the two forms of the projection-slice theorem is given in Appendix I in terms of a 3-D object function $\gamma(\bar{r})$ and its 3-D Fourier transform $\Gamma(\bar{p})$ where $\bar{r}$ and $\bar{p}$ designate position vectors in object space and Fourier space respectively. The object characteristic function $\gamma(\bar{r})$ can represent the object attenuation function as in x-ray imaging, or surface reflectivity as in integral holography and microwave imaging of reflecting objects, or refractive index distribution or velocity distribution as in electromagnetic and acoustic inverse scattering. Thus for example in x-ray tomography, projections of the object function $\gamma(\bar{r})$ are obtained by transmission measurements of absorbed x-rays while in integral holography photographs of the object taken from different aspect angles represent the set of projections. The projection-slice theorem is invoked then to obtain either by digital or optical means central slices of the Fourier domain $\Gamma(\bar{p})$ extending over a finite region of the Fourier space of the object.

In inverse scattering, complex (amplitude and phase) measurements involving wave-vector diversity (i.e., angular and spectral diversity) are used to determine $\Gamma(\bar{p})$ directly over a finite volume of Fourier space [9]-[13].

Thus the measurements performed and the subsequent data preprocessing in all of these methods aim at accessing a finite volume of the 3-D Fourier space of the object represented by $\Gamma(\bar{p})$. Once $\Gamma(\bar{p})$ has been determined, 3-D image detail representing a finite resolution version of $\gamma(\bar{r})$ can be retrieved as pointed out earlier via a 3-D inverse Fourier transform. In the following section we will describe two hybrid techniques for tomographic image reconstruction and display of the 3-D object function $\gamma(\bar{r})$ in which the required 3-D inverse Fourier transform is carried out optically as a series of 2-D Fourier transforms of projection holograms employing either coherent light or incoherent light.

3. Tomographic image reconstruction and 3-D display

Both coherent and incoherent optical computing can be used to carry out sequentially and rapidly the 2-D Fourier transforms of a series of weighted projection holograms corresponding to parallel equally spaced slices or cross-sectional outlines of the object in order to visualize its 3-D image tomographically.

Coherent scheme:

One such scheme employing the virtual Fourier transform has been described earlier [30]. The disadvantage of this scheme was that only one observer at a time can view the displayed virtual 3-D image. To overcome this limitation the arrangement shown in Fig. 1 was considered. This arrangement makes use of the real optical Fourier transform to project the re-

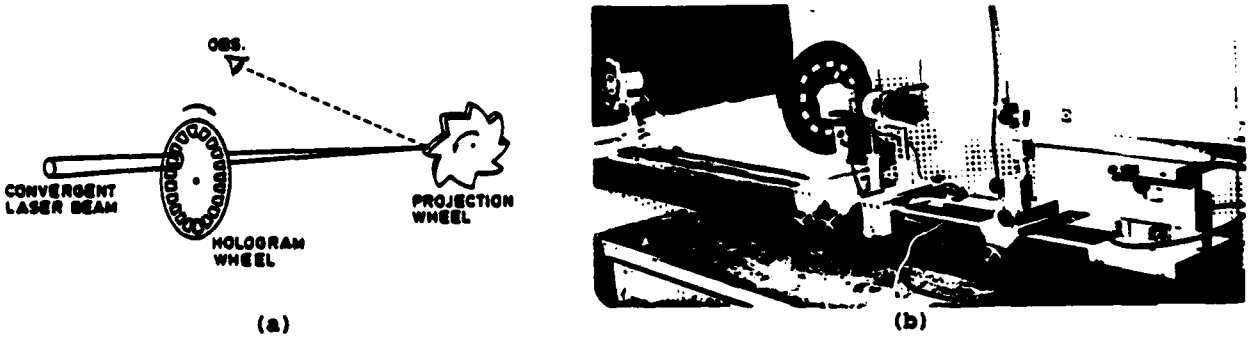

Fig. 1. Scheme for 3-D image reconstruction and display from a sequence of projection holograms. (a) Principle, (b) Pictorial view of system showing laser source to the right, hologram bearing wheel in the center and projection wheel to the left. Projection wheel is 25 cm in diameter and contains 24 windows for mounting the projection holograms.

constructed images of the various slices of the object rapidly and in proper sequence on an axially oscillating projection surface. The 3-D image reconstructed tomographically in this fashion can be viewed simultaneously by several observers from different directions. The arrangement consists of a convergent laser beam produced by a long focal length lens. The beam interrogates sequentially and rapidly a series of projection holograms mounted as shown on a rotating hologram bearing wheel. The axially oscillating projection surface is pro-

duced by rotating a suitably shaped projection wheel. The realization of a rapidly oscillating projection surface with this wheel is based on the eccentric rotation of a cylindrical surface. If a cylinder rotates eccentrically about an axis parallel to but displaced from the axis of the cylinder an observer will see the surface of the cylinder moving back and forth at the same rate of rotation. When a number, say eight, of such cylinders or cylindrical segments of the same radius are arranged together as shown in the projection wheel of Fig. 1(a) with their centers spaced evenly on the circumference of a circle centered on the axis of rotation, the same oscillating surface effect is observed but at eight times the rotation rate [31]. This permits the achievement of higher rates of projection surface displacement using reasonable rotation speeds that can be furnished by ordinary stepper motors. A pictorial view of the projection wheel used is shown in Fig. 2. Both the hologram bearing wheel and the projection wheel are driven by computer controlled stepper motors to maintain synchronization. Examples of the true 3-D image reconstruction and display achievable with this arrangement are shown in Fig. 3. Photographs of two views of the displayed 3-D image

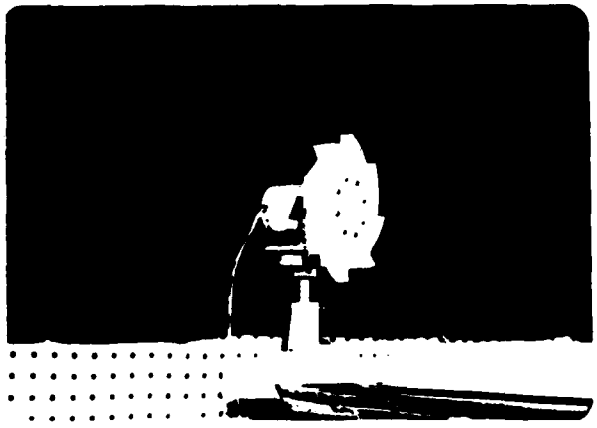

Fig. 2. Pictorial view of projection wheel used to realize an axially oscillating projection screen. A volumetric display region of 1.8 cm x 1.8 cm x 1.8 cm is provided.

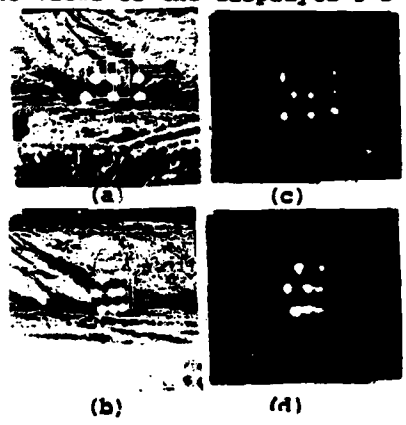

Fig. 3. Two views (a) and (b) of the tomographically reconstructed 3-D image of an eight point test object and identical corresponding views (c) and (d) of a model of the test object.

taken from two different aspect angles are shown in (a) and (b). The projection holograms used in the experiment were those of the eight point scatterer test object used in our earlier work [30]. Two identical views of a model of the test object are shown in (c) and (d) of Fig. 3 for comparison.

Incoherent scheme:

The second optical 3-D image reconstruction and display scheme studied is based on performing the required 2-D Fourier transforms directly on weighted projection holograms displayed in spatially incoherent light. This approach enables direct 2-D Fourier transformation of the CRT computer displays of weighted projection holograms corresponding to the different slices of the object. Being opto-electronic in nature the scheme permits displaying the image slices obtained by Fourier inversion in rapid succession on a second CRT display. A 3-D tomographic display of the displayed image slices can be realized employing a projection lens and the oscillating projection screen idea used in the preceeding scheme.

Several methods for incoherent 2-D Fourier transformation appear in the literature. These include shadow casting techniques using a two Fresnel zone masks as a Fourier analyzer [32], [33], achromatization [34], and opto-electronic methods utilizing optical multiplication by sine and cosine masks followed by electronic detection of the spatially integrated products [35]-[37]. A major advantage of these techniques is their freedom from speckle noise which is a known limitation of coherent optical processing. There are disadvantages however. Major among them is the complexity of carrying out complex operations and the low Fourier plane contrast in the Fresnel zone shadow casting scheme. There is also the "dynamic bias" problem identified in [38] and [39]. To handle complex data and increase throughput the use of color multiplexing or wavelength diversity in opto-electronic schemes has been considered [40].

The opto-electronic scheme described below combines *spatial domain projections* and *wavelength or color diversity* to perform Fourier transform operations on 2-D complex functions representing for example projection hologram data displayed on a color CRT monitor. In addition the scheme has the advantage of overcoming the dynamic bias problem. It differs from all other previously studied schemes in its novel use of the *spatial domain projection* theorem in a two color wavelength diversity scheme and in its potential to execute 2-D discrete Fourier transforms of large data formats approaching 1000 X 1000 pixels at high

AD-A135 253 HIGH RESOLUTION FREQUENCY SWEPT IMAGING(U) MOORE SCHOOL OF ELECTRICAL ENGINEERING PHILADELPHIA PA N H FARHAT 30 SEP 83 ARO-16828.6-EL DAAG29-80-K-0024 2/2

UNCLASSIFIED F/G 9/4 NL

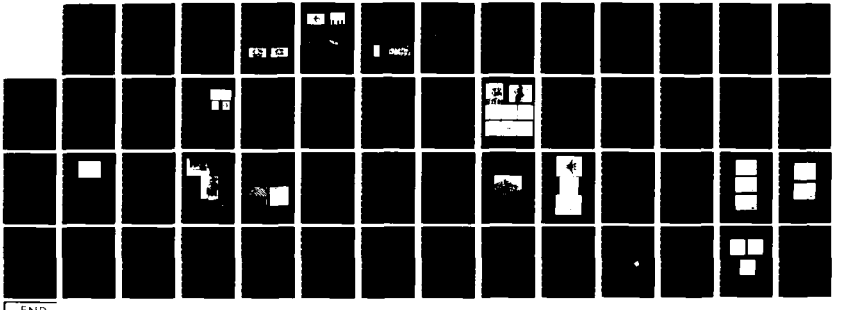

END

FILMED
1-84
DTIC

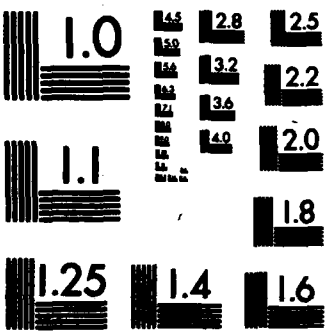

speeds. Another important practical advantage is the compatibility with a color CRT as the input device with its high brightness and precise color pixel locations.

The *Spatial Domain Projection Theorem* (see Appendix I) was first introduced in radio astronomy by Bracewell [22]. Its use in the present scheme is discussed next.

Consider a complex spatial function $f(x,y)$ with its 2-D Fourier transform $F(\omega_x,\omega_y)$, ω_x and ω_y being spatial frequency variables. Thus,

$$f(x,y) \leftrightarrow F(\omega_x,\omega_y) \tag{1}$$

designate a Fourier transform pair, where,

$$f(x,y) = \int_x \int_y F(\omega_x,\omega_y) e^{j(\omega_x x + \omega_y y)} d\omega_x d\omega_y \tag{2}$$

and

$$F(\omega_x,\omega_y) = \frac{1}{(2\pi)^2} \int_x \int_y f(x,y) e^{-j(\omega_x x + \omega_y y)} dxdy \tag{3}$$

The spatial projection of $f(x,y)$ on the x-axis is defined as

$$f_p(x) \triangleq \int_y f(x,y)\, dy \tag{4}$$

or by using (2),

$$f_p(x) = \int_y \{\int_{\omega_x} \int_{\omega_y} F(\omega_x,\omega_y)\, e^{j(\omega_x x + \omega_y y)} d\omega_x d\omega_y\}\, dy \tag{5}$$

Carrying out the integration with respect to y first we obtain

$$f_p(x) = \int_{\omega_x} \int_{\omega_y} F(\omega_x,\omega_y)\, e^{j\omega_x x}\, \delta(\omega_y)\, d\omega_x\, d\omega_y \tag{6}$$

or by the "sifting" property of the δ function,

$$f_p(x) = \int_{\omega_x} F(\omega_x,0)\, e^{j\omega_x x}\, d\omega_x \tag{7}$$

i.e., in abbreviated form,

$$f_p(x) \leftrightarrow F(\omega_x,0) \tag{8}$$

This final result, known as the *spatial domain projection theorem*, states that the spatial projection $f_p(x)$ of $f(x,y)$ and a central slice of its 2-D Fourier transform along a central line $\omega_y = 0$ are Fourier transform pairs. This suggests that the transform $F(\omega_x,\omega_y)$ can be obtained by a repeated application of the following three step process: (1) Rotate the object function $f(x,y)$ in the x-y plane, by an angle $n\Delta\theta$ $(n=1,2....N)$ relative to the x axis where $\Delta\theta = \frac{180°}{N}$, (2) form the projection on the x axis, and (3) one dimensional Fourier transform the projection to obtain the value of $F(\omega_x,\omega_y)$ along a central line passing through the origin of the ω_x-ω_y plane and making an angle $n\Delta\theta$ with the ω_x axis. By repeating the process for all the values of $n=1,2 \ldots N = 180°/\Delta\theta$ one can construct the transform $F(\omega_x,\omega_y)$ on a spoked format of radial lines of angular spacing $\Delta\theta$. Obviously this three step procedure can be implemented entirely digitally to provide a new discrete Fourier transform algorithm. Alternately the one dimensional Fourier transform required in the third step can be carried out with an analog CCD or SAW device [42]. Here an arrangement for performing the three step procedure opto-electronically is presented.

The arrangement is sketched in Fig. 4. The complex function $f(x,y)$ is displayed on a color CRT or TV screen. Two of the three available primary colors, (red, blue and green) are assigned to the real part $f_r(x,y)$ and the imaginary part $f_i(x,y)$ of $f(x,y)$ with the third color left unused or possibly reserved for use in an error correction scheme for enhancing the accuracy of the processor. The color display is imaged on the input face of an idealized tapered coherent fiber bundle C.F.B. 1 which performs the required projection operation by integrating or fusing the image in the vertical direction into a line image while reserving detail horizontally furnishing thus the projection $f_p(x)$ at its sharp edge. The complex nature of $f_p(x)$ is preserved in a two color display at this end. Image rotation is achieved by rotating the dove prism in the projection and image rotating segment which merely acts as a rotating image coupler. The C.F.B. 2 and C.F.B. 3 spread $f_p(x)$ vertically in the y direction while preserving detail in the horizontal x direction. Note that this does

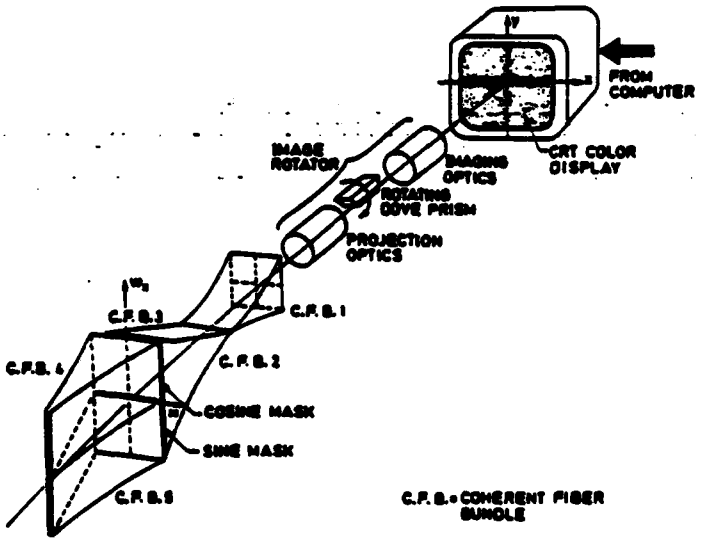

Fig. 4. High throughput incoherent 2-D complex fourier transformer based on the spatial domain projection theorem.

not restore the function f(x,y) but merely smears or "back-projects" the two colored $f_p(x)$ in the vertical direction uniformly. Later we shall see how the vertical projection operation and the vertical smearing or back-projection operation can be implemented simultaneously with a single anamorphic optical system.

In accordance to eq. (7) we seek the transform,

$$F(\omega_x,o) = \int f_p(x)\, e^{j\omega_x x}\, dx$$

$$= \int\{f_p^r(x) + j\, f_p^g(x)\}\{\cos\omega_x x + j\sin\omega_x x\}\, dx \qquad (9)$$

$$= \int\{f_p^r + jf_p^g(x)\}\ \cos\omega_x x\, dx$$

$$+ \int\{jf_p^r(x) - f_p^g(x)\}\ \sin\omega_x x\, dx \qquad (10)$$

Thus we need to multiply the complex function $f_p(x) = f_p^r(x) + jf_p^g(x)$ (where the real part is say coded in red and the imaginary part in green) by $\cos\omega_x x$ and $\sin\omega_x x$ and integrate the multiplication results with respect to x all this while preserving color discrimination. In practice this can be accomplished by placing at the input faces of C.F.B. 4 a cosine mask and at the input face of C.F.B. 5 a sine mask. The cosine and sine masks are neutral density transparencies that influence both colors equally. In practice the transmittance of the sine/cosine masks which are computer generated is positive real given by $(1 + \cos\omega_x x)$ respectively. Similarly because the functions $f_p^r(x)$ and $f_p^i(x)$ are to be represented as spatial intensity variations of incoherent light, one say with red light the other with green, bias terms must be added to handle negative values. Therefore in practice equation (10) assumes the form,

$$F(\omega_x,0) = \int\{[b^r + f_p^r(x)] + j\,[b^g + f_p^g(x)]\}(1 + \cos\omega_x x)\, dx$$

$$+ \int\{j[b^r + f_p^r(x)] - [b^g + f_p^g(x)]\}(1 + \sin\omega_x x)\, dx \qquad (11)$$

$$= \int[b^r\ (1+ \cos\omega_x x) - b^g\ (1 + \sin\omega_x x)]\, dx + j\int[b^g(1 + \cos\omega_x x)$$

$$+\ \ b^r\ (1 + \sin\omega_x x)]\, dx + \int[f_p^r(x) - f_p^g(x)]dx + j\int[f_p^r(x) + f_p^g(x)]\, dx$$

$$+ \int[f_p^r(x) + j\, f_p^g(x)]\, \cos\omega_x x\, dx + \int[jf_p^r(x) - f_p^g(x)]\, \sin\omega_x x\, dx \qquad (12)$$

where b^r and b^g are constant bias terms that enable us to represent the bipolar functions f_p^r and f_p^g by positive real red and green light intensities respectively. In eq. (12) the first and second integrals represent constant d.c. bias terms appearing in the output of the processor. This d.c. bias which has the effect of reducing contrast can eventually be removed by electronic filtering. The third and fourth integrals represent a signal dependent *dynamic bias* term. The fifth and sixth integrals are those of eq. (10) which represent the desired Fourier transform output. While electronic filtering of the d.c. bias term is a straight forward matter, it is not easy to remove the dynamic bias term because of its signal dependent nature. The presence of this term is undesirable since it behaves as noise signal that limits the dynamic range of the processor. A method for eliminating this bias term will be described below. The location of the two transparencies or masks together with the direction of the x and ω_x axis are shown in Fig. 4. Note that because of their neutral density (black and white) nature the screens will spatially modulate the two colors of $f_p(x)$ equally. That is the real and imaginary parts of $f_p(x)$ are each multiplied by the required cosine and sine kernels in accordance to eq. (10). The function of the idealized C.F.B. 4 and 5 is to perform the required integration in the x direction called for in eq. (10) after the multiplications in the integrand. The output data at the sharp vertical edge of C.F.B. 4 will therefore consist of two colors with the data in the two colors corresponding to the real and imaginary parts of the cosine transform of $f_p(x)$. Similarly the vertical distribution of the two colors appearing at the sharp edge of C.F.B. 5 will correspond to the real and imaginary parts of the sine transform of $f_p(x)$. Suitable color selective detection of the outputs of C.F.B. 4 and C.F.B. 5 for example with a color T.V. camera or by imaging the outputs on 4 self-scanned line detector arrays through a dispersive prism would yield four electronic signals representing the terms in eq. (11). These can be combined appropriately to obtain separately the real part and the imaginary of $F(\omega_x,o)$ and the process repeated as the image is rotated in steps. A high precision absolute angle encoder coupled to the rotating prism is used to provide signals that can be employed in displaying the transform line at the correct angle $n\Delta\theta$ relative to the ω_x axis on a CRT display providing thus $F(\omega_x,\omega_y)$ in successive central slices. Because of the high brightness of present day color displays, the flexibility of digital video processors that can be used to address them, the minimization of diffraction effects that give rise to cross-talk through the use of fiber optics technology and the high bandwidth of self-scanned detector arrays and their time integrating features we expect this 2-D optical D.F.T.* approach to yield high throughputs. For example a conventional color CRT such as the RCA RG511 provides 800 x 800 color pixels. This means that at the customary frame rate of 30/sec we can introduce 800 x 800 x 30 = $1.92\ 10^7$ complex data points/sec in the processor. The actual time required to perform a 2-D complex D.F.T. on the 800 x 800 complex data points would be determined by the rotation rate of the image which equals twice the rotation rate of the dove prism (a well known property of the dove prism).

Several image rotating techniques can be used. These include: digital, electron-optical, and opto-mechanical. Although digital and electron-optical schemes are inertialesss and therefore can offer high image rotation rates, a somewhat slower opto-mechanical scheme was found adequate for the present study and was therefore adopted because of its simplicity and much lower cost. The scheme is based on the well known image rotating property of the dove prism. A dove prism image rotator was therefore designed and constructed. Two pictorial views of the completed dove prism image rotator are shown in Fig. 5. In this design

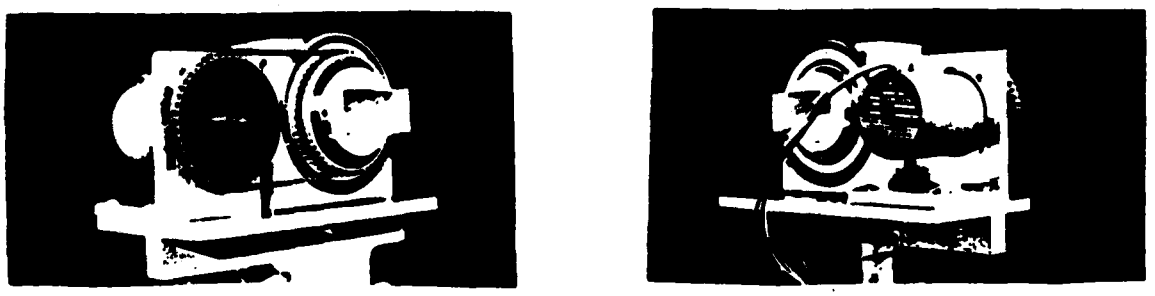

Fig. 5. Two pictorial views of dove prism image rotator and stepper motor drive.

the dove prism (a Rolyn model 45.030 of dimensions 30xmmx30xxml30mm) is mounted within the inner cylinder of a high precision ball bearing. The center cylinder of the bearing is rotated with respect to the outer part which is held stationary. Rotation was achieved with the aid of precision 1:1 belt drive powered by a computer controlled stepper motor capable of performing up to 20,000 half steps of .9° each per second. Means are furnished for centering and axial alignment of the dove prism within the inner cylinder of the ball bearing with the aid of adjustable screws. An example of the image rotating capability of the

*Discrete Fourier transform

image rotator is shown in the top part of Fig. 7. Three rotated images of a test, object shown in Fig. 6, are presented. These correspond to dove prism rotation angles of 0°, 45° and 90° respectively (recall that a dove prism rotation of θ° results in an image rotation of 2θ°).

Fig. 6. Test object

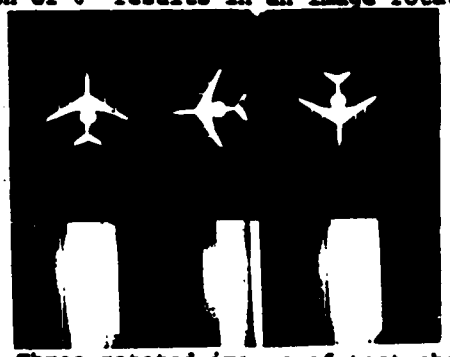

Fig. 7. Three rotated images of test object (top) and their vertically smeared versions (bottom).

Vertical image integration and spreading were to be carried out as originally proposed in Fig. 4 with the aid of tapered coherent fiber bundles CFB1, CFB2 and CFB3. It is clear that specialized and costly techniques are required in the manufacture of such idealized coherent fiber bundles with the required property. In practice a simple anamorphic optical system shown in Fig. 8, can be used to perform the function of the coherent fiber bundles CFB 1,2 and 3. The arrangement shown in Fig. 8 makes use of a single cylindrical lens to vertically smear the image i of any object scene 0. This smearing operation replaces the required vertical integration (spatial projection) and vertical spreading operations at the same time. Obviously this approach is more realistic and much less costly than the one

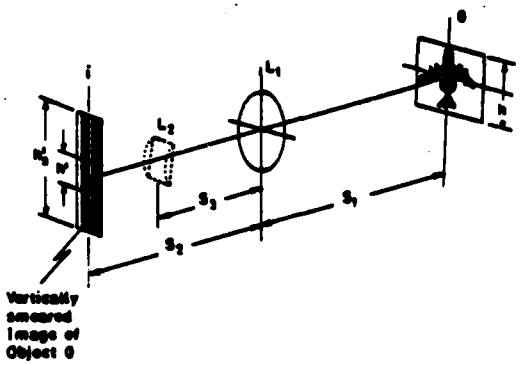

Fig. 8. Anamorphic optical system for vertical image smearing.

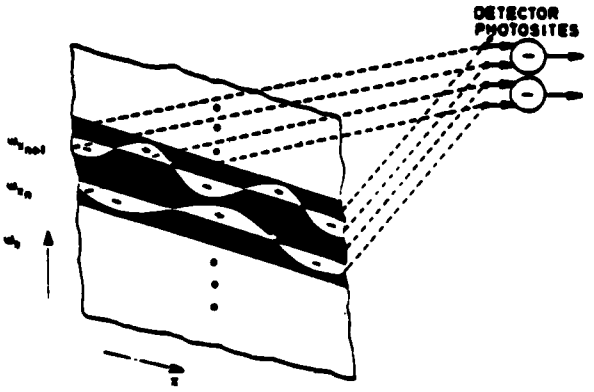

Fig. 9. Detail of transmission pattern on sine/cosine screen capable of eliminating dynamic bias problem.

calling for coherent fiber bundles and is therefore more attractive. In the scheme shown, spherical lens L_1 images the object scene 0 onto the image plane with a magnification $m = S_2/S_1 = h'/h$. The object scene 0 in Fig. 8 represents the rotated image furnished by the dove prism image rotator and its imaging optics (see Fig. 4). The cylindrical lens L_2 is added to smear the image vertically. The height h' of the vertically smeared image depends on the values of S_1, S_2, S_3 and the focal lengths F_1 and F_2 and on the height h of the original scene. The lower part of Fig. 7 is a pictorial record of the vertically smeared versions of the three rotated images shown in the upper part of the figure. These were obtained with the arrangement of Fig. 8 with the following parameter values: S_1 = 40 cm, S_2 = 14.5 cm, S_3 = 5 cm, F_1 = 10.5 cm, F_2 = 4.1 cm, and h = 5.5 cm. Excellent uniformity of the smeared image in the vertical direction is achieved. In the scheme of Fig. 4 a vertically smeared image similar to those shown in Fig. 7 would be projected onto the sine/cosine mask to perform the multiplication required in the integrands of eq. (10). In this fashion the vertical projection (integration) and spreading of the image rotated by the dove prism in Fig. 4 are accomplished simultaneously by the anamorphic optical system of Fig. 8 resulting in great simplification of the input portion of Fig. 4.

Generation of the required sine and cosine masks was achieved with the aid of a DEC Modular Instrumentation Computer (MINC) 11/2 and a high resolution Tektronix model 606A CRT display. A novel scheme was employed in the generation of the sine and cosine mask patterns which has the significant potential for eliminating the *dynamic bias problem* known to be a limiting factor in the operation of incoherent Fourier transform schemes [38],[39]. This approach to elimination of the dynamic bias problem takes advantage of the vertical uniformity of the smeared image projected on the sine/cosine mask to synthesize the equivalent of a negative transmittance with incoherent light. The scheme is opto-electronic in nature since it involves differential readout of the linear photodetector output shown in Fig. 4 in order to synthesize the negative transmittance. The *dynamic bias problem* stems directly from the fact that, aside from its spectral content, incoherent light can be represented by its intensity only which is positive real. Similarly the transmittance of any photographic transparency (such as the sine/cosine masks in our scheme) in incoherent light is also positive real. Therefore to represent a bipolar function that can assume negative values bias terms must be added as discussed earlier. The addition of these bias terms in the treatment above has been shown (see eq. (12)) to lead in the transform $F(\omega_x,0)$ to a d.c term, which can easily be filtered out in an electronic readout scheme, plus an undesirable signal dependent, dynamic bias term, which can not be excluded from the output without resort to complicated adaptive filtering. The presence of this undesirable signal dependent term can be considered as noise and will therefore limit the dynamic range of any incoherent optical processor. It's elimination would increase dynamic range and enhance performance. Our method for the elimination of the dynamic bias term is represented in Fig. 9 which shows the cosinusoidal transmittance of a portion of the sine or cosine masks at two adjacent frequencies ω_{x_n} and $\omega_{x_{n+1}}$. The black areas represent opaque portions. As the vertically smeared version of the rotated image in Fig. 8 is caused to impinge on such a screen the transmittance at each value of x will be proportional to the height of the cosinusoidal aperture at that value of x. By focusing the light emerging from the positive half cycles and the negative half cycles of each spatial frequency ω_{x_n} (as depicted symbolically in Fig. 9 by the dashed lines) on adjacent photosites of the self scanned linear detector array (or arrays) reading the output $F(\omega_{x_n},0)$ of the processor and subtracting the output of the detectors at these sites we essentially make the transmittances of the upper and lower half cycles of each spatial frequency of opposite sign realizing thereby a bipolar transmittance in incoherent light opto-electronically. It is indeed fortunate that many linear self scanned detector arrays marketed today (e.g. Reticon's and Fairchild's) lend themselves for use in this scheme because normally the even numbered photosites are read-out with one shift register while the odd numbered photosites by another. By substracting the outputs of the two shift registers, instead of adding them as done in normal use, the above output readout scheme can be realized immediately.

Figure 10 is an example of a sine/cosine mask that makes use of the above encoding concept. This particular mask was produced on our high resolution computer display for use with a 256 element detector array. The sine and cosine portions of the mask each contain spatial frequencies extending from -34 to +34. Each frequency requires the use of two detector photosites for dynamic bias suppression.

Fig. 10. Computer generated sine/cosine mask.

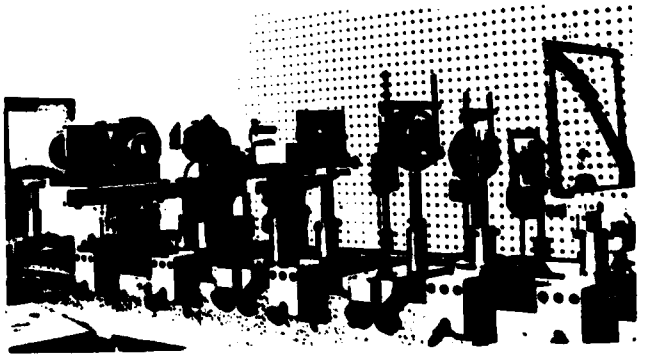

Fig. 11. Pictorial view of incoherent fourier transformer. From left: object scene, dove prism image rotator, imaging lens, cylindrical lens for vertical image smearing and sine/cosine screen, followed by output part consisting of anamorphic spherical/cylindrical lens system.

The preceeding discussion suggests a modified version of the scheme of Fig. 4 for implementing the spatially incoherent Fourier transform. This modified version is shown in

Fig. 12 and in the pictorial view of Fig. 11. The output portion of the modified arrangement comprised of components downstream from the sine/cosine mask, makes use of a second anamorphic optical system consisting of a spherical lens L_3/cylindrical lens L_4 combination, instead of the coherent fiber plugs CFB4 and CFB5 in the original configuration of Fig. 4, to horizontally integrate light emerging from the positive and negative half cycles of each spatial frequency component in the masks onto pairs of adjacent photosites in the output self scanning detector arrays D_G and D_R. The dispersive prism (or alternatively a dichroic beam splitter) is used to separate the two colors (red and green) onto the self scanning detector arrays. In this anamorphic output segment of the processor, spherical lens L_3 images the output of the sine/cosine mask on the plane of the output detectors while the addition of the cylindrical lens power in the horizontal direction only focuses the image detail horizontally over a width equal to the width of the detector. Selection of lenses L_1 and L_2 and the various spacing between components can be made by referring to the anamorphic system representation of Fig. 13. Figure 13 also suggests that detector arrays with the largest available width w' are desirable since a large w' relaxes both the focusing requirement from the horizontally integrating lens and the horizontal demagnification of the system. The widest commercially available w' is that of Reticon S-series (Spectroscopic) self scanning detectors with w'=2.5mm. This family of detectors also has separate odd/even shift register output capability permitting dynamic bias elimination and have a wide bandwidth and dynamic range which makes them ideal for this application.

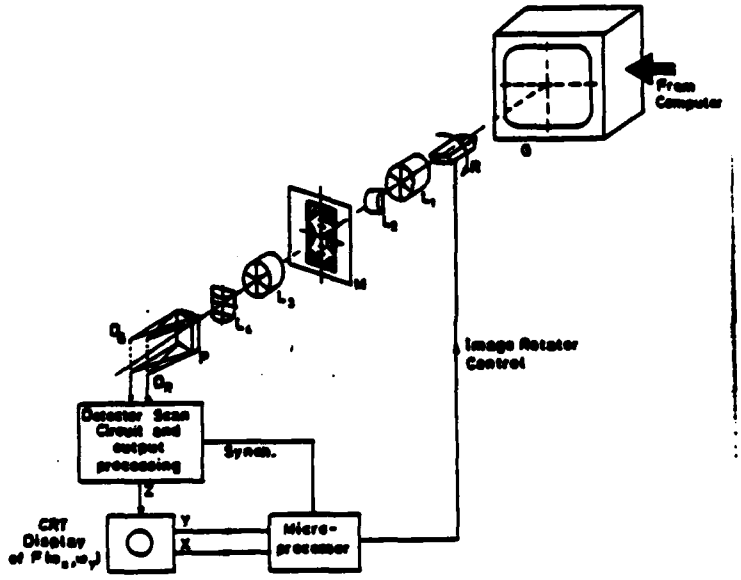

Fig. 12. Incoherent fourier transform scheme employing spatial domain projections and color diversity to perform complex transforms.

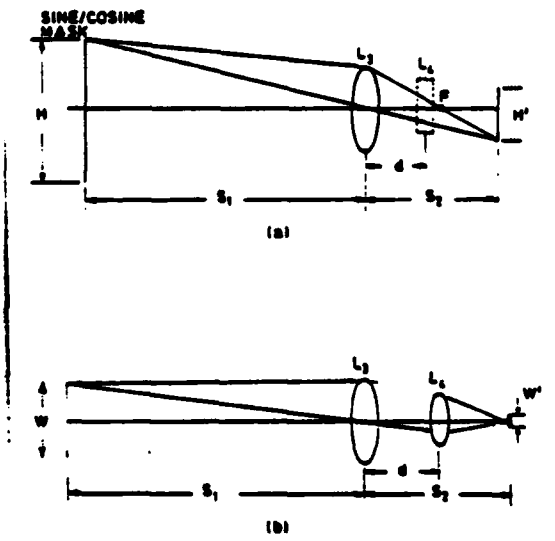

Fig. 13. Anamorphic optical system for use in the output part of Fig. 12.

4. Discussion and conclusions

Optical computing is inherently suited for processing of one dimensional or two dimensional signals. Optical processing of multi-dimensional signals becomes possible through the application of projection theorems. This paper demonstrates the utility of the projection-slice theorem stemming from the multi-dimensional Fourier transform in optical computing particularly in 3-D tomographic image reconstruction and display.

Two hybrid (opto-digital) processing schemes for true 3-D image reconstruction and display were described. Both schemes employ space-time multiplexing to display 3-D images tomographically in parallel slices. The space-time multiplex feature also allows considerable relaxation of the resolution capability of the recording device (photographic film for instance) used to store the projection hologram as compared to conventional holographic 3-D imaging.

In the one scheme employing coherent optical processing, a 3-D volumetric display, few centimeters cube in size, is demonstrated. Unaided viewing of the 3-D image is possible by several observers simultaneously. The fidelity of the retrieved 3-D image is found to be quite good despite the slight curvature of the oscillating projection surface. It is worth noting that the disc film format of the newly introduced Kodak Disc 4000 camera with

its 18 circularly distributed exposure cites is perfectly suited for use as the hologram bearing wheel in this scheme. Replacement of the photographic storage used in this scheme by a fast recyclable spatial light modulator (SLM) would allow its use with a computer display of projection holograms directly to realize overall real-time operation.

The second scheme employing incoherent light has the advantage of being able to accept a color CRT or computer graphic video display as the input format directly. It performs the required 2-D Fourier transform of a projection hologram displayed by the computer as a series of one dimensional incoherent opto-electronic Fourier transforms through the use of a spatial domain projection theorem. The scheme can handle complex data by color coding. It can suppress the dynamic bias problem and has the potential for high throughput. For example the use of four self scanning detector arrays of 1024 elements each at 5MHz clock rate in this scheme would permit carrying out a complete 2-D complex Fourier transform of 100 radial lines each containing 612 frequency points in about 10 msec. This indicates a throughput of 6.12 10^4 operations per msec which is about two order of magnitudes faster than a digital array processor. The required dove prism rotation rate then is 6000 RPM. The rotation period of the prism and the persistance of the color CRT display must however be matched.

Tradeoff between serial and parallel processing in the scheme of Fig. 12 is possible. This can be achieved by using N processors of the type shown in Fig. 12 to view the CRT display (or object scene) in parallel simultaneously with each processor handling a different set of the 180°/$\Delta\theta$ radial lines of the fourier transform $F(\omega_x,\omega_y)$. This would have the advantage of reducing the processing time by a factor N.

To date characterization of the various parts of the scheme such as the image rotation subsystem, the integration and image spreading subsystem, and the sine/cosine masks has been completed. Evaluation of the output segment is underway. Overall performance evaluation is expected in the near future.

5. Acknowledgement

This work was sponsored in part by the Air Force Office of Scientific Research, Air Force Systems Command under Grant No. AFOSR-81-0240 and by the Army Research Office under Contract No. DAAG-29-K-0024.

References

1. E. Wolf, Optics Comm., Vol. 1, 153, Sept/Oct. 1969.
2. E. Wolf, J. Opt. Soc. Am., Vol. 60, 18-20, Jan. 1970.
3. R. Dandliker and K. Weiss, Optics Comm., Vol. 1, 323-328, Feb. 1970.
4. W.H. Carter, J. Opt. Soc. Am., Vol. 60, 306-314, March 1970.
5. W.H. Carter and P-C Ho., App. Optics, 13, 162-172, Jan. 1974.
6. A.J. Devany, J. Math. Phys., Vol. 19, 1526-1531, July 1979.
7. A.F. Fercher, et. al., Appl. Optics, Vol. 18, 2427-2439, July 1979.
8. A. Jain, App. Phys. Letters., Vol. 28, 451-453, April 1976.
9. R.M. Lewis, IEEE Trans. on Ant. and Prop., Vol. AP-17, 108-314, May 1969.
10. N. Bojarski, Report under contract B0019-73-C-0316, Naval Air Syst. Command, Feb., 1974.
11. IEEE Trans. on Ant. and Prop. - Special Issue on Inverse Methods in Electromagnetics, W. Boerner, A.K. Jordan and I. Kay (Eds.), Vol. AP-29, March 1981.
12. N.H. Farhat and C.K. Chan, in *Acoustical Imaging*, Vol. 8, A. Metherell (Eds.) Plenum Press, 499-515, New York (1980).
13. C.K. Chan and N.H. Farhat, IEEE Trans. on Ant. and Prop., Vol. AP-29, 312-319, March 1981.
14. G.W. Stroke and M. Halioua, Trans. Am., Cryst. Assoc., Vol. 12, 27-41, (1976).
15. W. Swindell and H. Barrett, Physics Today, Vol. 30, 32-41, Dec. 1977.
16. G. Baum and G.W. Stroke, Science, Vol. 189, 994-995, Sept. 1975.
17. D.L. Vickers, Lawrence Livermore Laboratory, Report No. UCID-17035, Feb. 1976.
18. T. Okoshi, *Three-Dimensional Imaging Techniques*, Academic Press (1976).
19. T. Okoshi, "Three-Dimensional Displays", Proc. IEEE, Vol. 68, 548-564, May 1980.
20. T. Walters and W. Harris, Byte, Vol. 3, 16-30, May 1978.
21. J. Radon, "Uber die Bestimmung von Funktionen durch ihre integralwerte langs gewisser Mannigfaltigkeiten", Ber. Saechs. Akad. Wiss. (Leipzig), Vol. 69, pp. 262-278, (1917)
22. R.N. Bracewell, Aust. J. of Phys., Vol. 9, 198-217, (1956).
23. R.N. Bracewell and S.J. Werneke, J. Opt. Soc. Am., Vol. 65, 1342-1346, Nov. 1975.
24. G. Stroke, et. al., Proc. IEEE, Vol. 65, 39-62, Jan. 1977.
25. R.M. Mersereau and A.V. Oppenheim, Proc. IEEE, Vol. 62, 1319-1338, Oct. 1974.
26. H.H. Barrett, Optics Letters, Vol. 7, June 1982, pp. 248-250.
27. H.H. Barrett, "Three-Dimensional Image Reconstruction from Planar Projections, with Applications to Optical Data Processing", in *Transformations in Optical Signal Processing*, W.T. Rhodes, J.R. Fienup and B.E.A. Saleh (Eds.). SPIE, Bellingsham 1982, (To be published).
28. H. Barrett, "The Radon Transform and its Applications", to be published in Progress in Optics.

29. N. Farhat, "High Resolution 3-D Tomographic Imaging by Wavelength and Polarization Diversity", University of Pennsylvania Proposal submitted to AFORS, May 14, 1981
30. N.H. Farhat and C-Yi Ho, in Optics in Four Dimensions, M.A. Machado and L.M. Narducci (Eds.). Am. Inst. of Phys., New York (1981), 341-354.
31. P.R. Bradley-Moore and E.A. Woloshue, Strobosopic Analyzing Monitor, Zyntrax Corp. Report, 135 East 65th St., New York, NY 10021.
32. J.M. Richardson, "Device for Producing Identifiable Sine and Cosine (Fourier) Transforms of Input Signals by Means of Noncoherent Optics", U.S. Patent 3,669,528, June 1972.
33. G.L. Rogers, *Noncoherent Optical Processing*, J. Wiley & Sons, London (1977).
34. G.M. Morris, App. Optics, Vol. 20, 2017-2024, June 1981.
35. J. Goodman and L.M. Woody, App., Opt., Vol. 16, 2611-2612, 1977.
36. J. Goodman, et. al., Optics Letters, Vol. 1, 1978.
37. K. Bromely et. al., "Incoherent Optical Signal Processing Using Charge Coupled Devices (CCD's)", in *Optical Signal and Image Processing*, SPIE, Vol. 118, pp. 118-123, 1977.
38. A.R. Dias, "Incoherent Matrix-Vector Multiplication for High Speed Data Processing", Stanford Electronics Laboratory, Stanford University Technical Report No. L722-4., June 1980.
39. J. Goodman and K. Johnson, "Optical Computing Research", Stanford Electronics Laboratory, Stanford University Technical Report No. L722--6, March, 1981.
40. P. Wiersma, Optics Comm., Vol. 28, 280-282, March, 1979.
41. Y. Das and W.M. Boerner, IEEE Trans. on Ant. and Prop., Vol. AP-26, pp. 274-379, March, 1978.
42. H.J. Whitehouse, "The Role of Charge Coupled Devices and Surface Acoustic Wave Devices in Optical Signal Processing", SPIE, Vol. 118, 1977, pp. 124-131.

Appendix 1

The projection-slice theorem

Let $\gamma(\bar{r})$ and $\Gamma(\bar{p})$ be a Fourier transform pair representing a 3-D object function and its 3-D Fourier transform respectively, i.e.,

$$\Gamma(\bar{p}) = \int_v \gamma(\bar{r})\, e^{-j\bar{p}\cdot\bar{r}}\, d\bar{r} \tag{A-1}$$

where v defines the object extent and

$$\gamma(\bar{r}) = \frac{1}{(2\pi)^3} \int \Gamma(\bar{p})\, e^{j\bar{p}\cdot\bar{r}}\, d\bar{p} \tag{A-2}$$

where working in cartesian coordinates $\bar{r} = x\,\bar{I}_x + y\,\bar{I}_y + z\,\bar{I}_z$ and $\bar{p} = p_x\,\bar{I}_x + p_y\,\bar{I}_y + p_z\,\bar{I}_z$ are position vectors in object space and Fourier space respectively with $d\bar{r}$ and $d\bar{p}$ being differential elements in $\bar{r}$-space and $\bar{p}$-space.

The projection of $\Gamma(\bar{p})$ on a given plane, for example the p_x - p_y plane, is

$$\Gamma_{proj.}\,(p_x,p_y) = \int_{p_z} \Gamma(p_x,p_y,p_z,)\, dp_z \tag{A-3}$$

Substituting (A-1) in (A-3), we obtain

$$\Gamma_{proj.}\,(p_x,p_y) = \iiint \gamma\,(x,y,z) \int e^{-j(p_x x + p_y y + p_z z)}\, dp_z)\, dx\, dy\, dz \tag{A-4}$$

If the extent of $\Gamma(\bar{p})$ is sufficiently large the integration of the exponential $e^{-jp_z z}$ with respect to p_z yields approximately a delta function $\delta(z)$ leading to,

$$\Gamma_{proj.}\,(p_x,p_y) = \iiint_{xyz} \gamma(x,y,z)\,\delta(z)\, e^{-j(p_x x + p_y y)}\, dx\, dy\, dz$$

$$= \iint_{xy} \gamma(x,y)\, e^{-j(p_x x - p_y y)}\, dx\, dy. \tag{A-5}$$

where $\gamma(x,y)$ is a central slice through the object $\gamma(\bar{r})$ parallel to the p_x - p_y plane.

It follows from eq. (A-5) by the inverse transform that

$$\gamma(x,y) = \frac{1}{(2\pi)^2} \int_{p_x} \int_{p_y} \Gamma_{proj.}\,(p_x,p_y)\, e^{j(p_x x + p_y y)}\, dp_x dp_y \tag{A-6}$$

which is one form of the required theorem. Accordingly, the projection of the 3-D transform data on a given plane is the Fourier transform of a central or meridional slice through the

object oriented parallel to the particular projection plane.

Fourier transform relationships between parallel projections and parallel slices can be obtained by invoking the concept of *weighted projection*. For example let $\Gamma^{\alpha}_{\text{proj.}}(p_x,p_y)$ be the weighted projection of $\Gamma(\bar{p})$ defined as,

$$\Gamma^{\alpha}_{\text{proj.}}(p_x,p_y) = \int_{p_z} \Gamma(p_x,p_y,p_z)\, e^{j\alpha p_z}\, dp_z \qquad \text{(A-7)}$$

where α is a real weighting parameter. Substituting for Γ from eq. (A-4) yields,

$$\Gamma^{\alpha}_{\text{proj.}}(p_x,p_y) = \int_{p_z} e^{j\alpha p_z} \int_x \int_y \int_z \gamma(x,y,z)\, e^{-j(p_x x + p_y y + p_z z)}\, dx\, dy\, dz\, dp_z \qquad \text{(A-8)}$$

Carrying out the integration with respect to p_z first while assuming the extent of $\Gamma(\bar{p})$ in the p_z direction is sufficiently large, the integral with respect to p_z may be approximated by $\delta(z-\alpha)$. Equation (A-8) can then be reduced to,

$$\Gamma^{\alpha}_{\text{proj.}}(p_x,p_y) = \int_x \int_y U(x,y,z=\alpha) e^{-j(p_x x + p_y y)}\, dx\, dy \qquad \text{(A-9)}$$

which says that $\Gamma^{\alpha}_{\text{proj.}}(p_x,p_y)$ and $\gamma(x,y,z=\alpha)$ are two dimensional Fourier transform pairs. The weighted Fourier domain projection theorem follows from the inverse transform

$$\gamma(x,y,z=\alpha) = \frac{1}{(2\pi)^2} \int_{p_x} \int_{p_y} \Gamma^{\alpha}_{\text{proj.}}(p_x,p_y) e^{j(p_x x + p_y y)}\, dp_x\, dp_y \qquad \text{(A-10)}$$

Accordingly parallel slices of the object can be reconstructed from the weighted projection $\Gamma^{\alpha}_{\text{proj.}}(p_x,p_y)$ computed for different values of the weighting parameter α.

Because of the symmetrical nature of the Fourier transform the above treatment can be repeated by starting with projections in object space rather than projections in Fourier space to show that projections of $\gamma(\bar{r})$ and slices of $\Gamma(\bar{p})$ form Fourier pairs.

Finally it is worth noting that 2-D projections in Fourier space can be regarded as proposed in [14] and [21] as *projection holograms*.

APPENDIX VII

TOMOGRAPHIC AND PROJECTIVE RECONSTRUCTION OF 3-D IMAGE DETAIL IN INVERSE SCATTERING

(Reprint from IEEE 1983 Proceedings of the 10th International Optical Computing Conference on Non-conventional Imaging and Transforms, Boston)

TOMOGRAPHIC AND PROJECTIVE RECONSTRUCTION OF 3-D IMAGE DETAIL IN INVERSE SCATTERING

N. H. Farhat
T. H. Chu
C. L. Werner

Reprinted from IEEE 1983 PROCEEDINGS OF THE
10TH INTERNATIONAL OPTICAL COMPUTING CONFERENCE

TOMOGRAPHIC AND PROJECTIVE RECONSTRUCTION OF 3-D IMAGE DETAIL IN INVERSE SCATTERING

N.H. Farhat, T.H. Chu and C.L. Werner
Electro-Optics and Microwave Optics Laboratory
University of Pennsylvania
The Moore School of Electrical Engineering
Philadelphia, PA 19104

Abstract

A procedure for accessing the 3-D Fourier space of a conducting or nondispersively scattering object by angular (aspect) and spectral diversity is described. Cost-effective data acquisition in the microwave regime is achieved by substituting spectral degrees of freedom for the more costly angular degrees of freedom set by the number of observation points defining the imaging aperture. A novel *target derived reference* (TDR) technique is utilized to generate a synthetic phase reference signal emanating from a point on the target achieving thereby a *3-D lensless Fourier hologram* recording arrangement that has many practical advantages. Application of the *projection-slice theorem*, derivable from the multidimensional Fourier transform, to the accessed Fourier space volume is shown to allow the retrieval of 3-D image detail. This can be achieved either tomographically in slices (or cross-sectional outlines) or as shown here in the form of a projection image of the object scattering function. Examples of microwave data acquisition, data normalization for an undesirable range dependent phase term via the TDR method, and image reconstruction are presented for a complex conducting test object. The results shown herald a new generation of high resolution 3-D imaging radars and can be applied in NDE (nondestructive evaluation), biomedical imaging, and remote sensing applications.

Introduction

The implementation of high resolution longwave (microwave and acoustic) inverse scattering or holographic imaging systems involves the acquisition of the object scattered field over extended recording apertures that subtend sufficiently large solid angles at the object. Because of the discrete nature of longwave sensors, only a sampled version of the scattered field distribution over the recording aperture can be recorded. Sampling considerations ordinarily require dense sampling to avoid retrieved image degradation through deterioration of the impulse response and aliasing. The cost of implementing such densely sampled apertures is at present quite prohibitive because of the large number and high cost of the coherent sensors required to form the aperture specially for remote scattering objects when the extent of the aperture required to yield high resolution is quite large. Obviously *aperture thinning* by reducing the number of elements can be employed to cut cost. However a systematic study of ordered and random aperture thinning [1],[2] indicates rapid deterioration in resolution and image quality with degree of thinning. The effect of aperture thinning is best described by its influence on the shape and side-lobe level of the impulse response or point spread function of the aperture [2]. It is generally true that even with an acceptable degree of thinning, where the deterioration of image quality is still tolerable, the cost of longwave apertures remains generally high. To overcome this constraint we have proposed to use a target derived reference [3]-[6] and demonstrated the utility of wavelength diversity [3],[4] as a means of making a highly thinned (sparse) aperture collect more information about a scattering conducting or nondispersive object thus imparting to the aperture a resolution capability better than would be possible monochromatically at the shortest operational wavelength case. The effect of wavelength diversity can be explained in terms of spectral aperture synthesis or as trade-off between costly spatial degrees of freedom associated with the number of elements and the less costly spectral degrees of freedom associated with wavelength diversity. Specifically one can show from inverse scattering theory [3]-[8] that coherent multiaspect monostatic or bistatic measurements of the far field scattered by a plane wave illuminated nondispersive object, as a function of frequency, can be used to access the 3-D Fourier space $\Gamma(\bar{p})$ of the object scattering function $\gamma(\bar{r})$, $\bar{r}$ and $\bar{p}$ being 3-D position vectors in object space and Fourier space respectively. The scattering function represents the 3-D geometrical distribution and strength of those object scattering centers that contribute to the measured field. Normalization of the measured field for range-phase, clutter, and system frequency response leads in practice to accessing a finite volume $\Gamma_m(\bar{p})$ of the Fourier space $\Gamma(\bar{p})$. It is possible then as shown by computer simulation in references [3] and [4] to retrieve a *diffraction and noise limited* version $\gamma_d(\bar{r})$ of the object scattering function $\gamma(\bar{r})$ by 3-D Fourier inversion.

In this paper we present first a brief review of the principle of 3-D imaging by wavelength diversity. This is followed by a description of the procedure used to access the 3-D Fourier space of a microwave scattering object employing an experi-

CH1880-4/83/0000/0082$01.00 © 1983 IEEE

mental microwave imaging facility [9]. Description of the projection imaging of the 3-D scattering center distribution of a complex scattering object, a 100:1 metalized scale model of a B-52, is then given. Finally the role of polarization diversity to further enhance image quality is briefly discussed and implications of the results in radar imaging and other remote sensing applications are presented.

Theoretical Considerations

It is sufficient for the purpose of this discussion to use a simplified scalar formulation in which polarization effects are ignored. Then the far field scattered by the object (under the physical optics and Born approximations) in the direction of the unit vector $\hat{I}_R$ due to plane wave illumination incident in the direction of the unit vector $\hat{I}_i$ can be expressed as, [3]-[8],

$$V(\vec{p},R) = \frac{jAke^{-jkR}}{2\pi R} \int_{-\infty}^{\infty} \gamma(\vec{r}) e^{j\vec{p}\cdot\vec{r}} d\vec{r} \qquad (1)$$

where $\gamma(\vec{r})$ is taken here to represent the object scattering function, which for conducting bodies of interest in this paper departs from zero only on the illuminated surface of the body, $\vec{r}$ is a 3-D position vector of an object point measured relative to a common origin in the object or its vicinity, $\vec{p} = k(\hat{I}_R - \hat{I}_i)$ is a 3-D position vector in Fourier space, $d\vec{r}$ is the differential element of integration, R is the distance between an observation point and the common origin and A represents the strength of the incident illumination. The integral in eq. (1) shows that far field measurements carried out for a sufficient range of values of $\vec{p}$ that are realized by varying $\hat{I}_R$ and/or $\hat{I}_i$ (angular diversity) and by varying k (frequency or wavelength diversity) permits accessing a finite region of the 3-D Fourier space

$$\Gamma(\vec{p}) = \int_{-\infty}^{\infty} \gamma(\vec{r})\, e^{j\vec{p}\cdot\vec{r}} d\vec{r} = -j\,\frac{2\pi R}{Ak}\, e^{jkR}\, V(\vec{p},R). \qquad (2)$$

$\Gamma(\vec{p})$ can be regarded as a *3-D Fourier transform hologram* of the object scattering function. The size and shape of the accessed region of $\vec{p}$-space depends on the values of $\vec{p}$ used in the measurement. Equation (2) shows that derivation of $\Gamma(\vec{p})$ from the measured field $V(\vec{p},R)$ requires knowledge of the range R from a reference point on the object to each observation point in order to carry out the required range-phase normalization. Equation (2) shows further that a diffraction and noise limited version of $\gamma(\vec{r})$ can be retrieved by 3-D Fourier inversion of the available $\Gamma(\vec{p})$. It is clear that the function $\Gamma(\vec{p})$ can in practice be determined over only a finite number of points defining the accessed volume of $\vec{p}$-space. We assume here without further elaboration that the $\vec{p}$-space sampling interval obeys the Nyquist criterion in order to avoid aliasing in the image reconstruction. Inversion of eq. (2) yields,

$$\gamma(\vec{r}) = \int_{-\infty}^{\infty} \Gamma(\vec{p}) e^{-j\vec{p}\cdot\vec{r}} d\vec{p} \qquad (3)$$

where $\vec{r}$ is now a 3-D position vector in image space.

Representing next the conjugate variables $\vec{r}$ and $\vec{p}$ by their cartesian components and computing the projection of $\gamma(\vec{r})$ on the x-y plane we obtain,

$$\gamma_{proj}(x,y) = \int_{-\infty}^{\infty} \gamma(x,y,z)\, dz = \int_{-\infty}^{\infty} dz$$

$$\iiint_{-\infty}^{\infty} \Gamma(p_x,p_y,p_z) e^{-j(p_x x + p_y y + p_z z)} dp_x dp_y dp_z$$

$$= \iint_{-\infty}^{\infty} \Gamma(p_x,p_y,o) e^{-j(p_x x + p_y y)} dp_x dp_y \qquad (4)$$

which shows that the projection $\gamma_{proj}(x,y)$ of the scattering function on the x-y plane and a central slice $\Gamma(p_x,p_y,o)$ though $\Gamma(\vec{p})$, that is parallel to the projection plane are a Fourier transform pair. Because the Fourier transform conserves rotation, i.e. rotation of the object function results in identical rotation of the Fourier transform, the result in eq. (4) can be generalized to show that projections of $\gamma(\vec{r})$ in any given direction, other than the z direction chosen above, is the 2-D inverse Fourier transform of a central slice through $\Gamma(\vec{p})$ oriented normal to direction of projection. This *projection-slice theorem* was discussed by Radon in 1917 [10] and has since been applied to radio astronomy [11], crystallography and electron microscopy [12], X-ray and radio-emissive tomography [13], and to microwave imaging and radar target shape recognition [3],[4],[14],[15] and is applied below in the first demonstration of projection imaging of scattering centers on a target from actual microwave scattering data in the (6-17) GHz range.

Data Acquisition and Image Reconstruction

The test object, a metalized 100:1 scale model of a B-52 aircraft with 79 cm wing span and 68 cm long fuselage, was mounted on a computer controlled elevation-over-azimuth positioner situated in an anechoic chamber environment. Automated measurement of the scattered field over any band in the (6-18) GHz frequency range is provided by a coherent microwave measurement system consisting of a microwave sweeper and a coherent receiver as shown in Fig. 1.

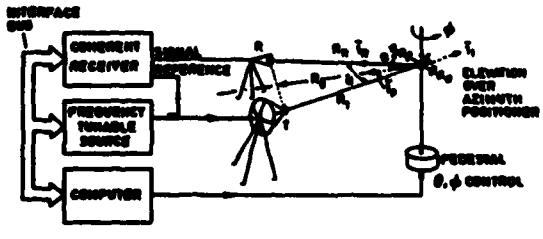

Figure 1. Recording Arrangement

It is important to note that the $\bar{p}$-space accessed by rotating the object relative to a fixed T/R is identical to that accessed by spherical scanning the T/R about the fixed object over the same range of aspect angles. The measurement system of Fig. 1 is specifically configured to provide maximum versatility in the study of broadband microwave imaging, holography, and inverse scattering and in the evaluation of innovative radar imaging concepts [9]. Plane wave illumination of the object at an irradiance level of about 10 mW/cm^2 is produced. Circularly polarized transmitting and receiving antennas are utilized and the amplitude and phase of the scattered field at the receiving antenna R is measured with the aid of a microwave network analyzer acting as a coherent receiver. Note the measurement configuration in Fig. 1 is nearly monostatic except for a slight spacing between the T/R antennas for the insertion of a microwave absorbing panel (not shown) intended to minimize direct leakage between antennas. In the arrangement shown $\alpha = 20°$ and $R_0 \approx 7$m. The entire measurement sequence consisting of angular positioning of the object in azimuth and elevation in increments of .7°, incremental frequency stepping over the (6-17) GHz in selectable frequency steps, digitization and storage of the amplitude and phase readings of the coherent receiver is carried out under control of a DEC Modular Instrumentation Computer, a MINC 11/2, which also performs the data reduction and display and all necessary image computations. The specified accuracy of amplitude and phase measured by the coherent receiver are $\pm$1.2dB and $\pm$4 degrees respectively. Settability in frequency tuning is possible to an accuracy of better than 1 MHz through precalibration with a microwave counter and least squares fit of a quadratic function to the measured frequency versus voltage transfer function of the sweep oscillator performed by the computer. Frequency incrementing by $\delta f = c/2L$ where L is a characteristic size of the scattering object is chosen to satisfy the Nyquist sampling criterion and avoid aliasing in the retrieved image. Assuming L = 79 cm for the B-52 a δf = 86.6 MHz was used requiring accordingly 128 frequency steps to cover the (6.1-17.1) GHz range employed in obtaining the data used below. A single Fourier space slice of finite extent was obtained for a fixed object elevation angle of $\theta = 30°$ while the azimuth angle ϕ was altered between -45° to +45° relative to broadside orientation of the model (when the fuselage is perpendicular to the line bisecting the angle α in Fig. 1) in steps of .7° for a total of 128 angular looks. This arrangement was chosen to simulate the $\hat{p}$-space data that would be collected in the imaging geometries of a passing aircraft depicted in Fig. 2. For the value of $\alpha = 20°$ used in the recording geometry the vector $\hat{p} = k(\hat{l}_1 - \hat{l}_2) = 2k \cos\frac{\alpha}{2}\,\hat{l}_p$ extends from $p_1 = 2k_1\cos\frac{\alpha}{2} = 503.25$ Rad/m to $p_2 = 2k_2\cos\frac{\alpha}{2} = 1402.5$ Rad/m in the direction of $\hat{l}_p$ along the bisector of the angle α in Fig. 1. In this fashion the p-space is accessed in a polar format consisting of 128 radial lines each corresponding to one value of ϕ covering an angular span of 90° with each line containing 128 data points for a total of 16,384 complex data points. A computer display of $\mathrm{Re}\{\Gamma(\hat{p})\}$ over the accessed slice obtained in this fashion is shown in Fig. 4 (a). The time required to obtain the slice data is of the order of 20 minutes. This includes measurement time and data correction time.

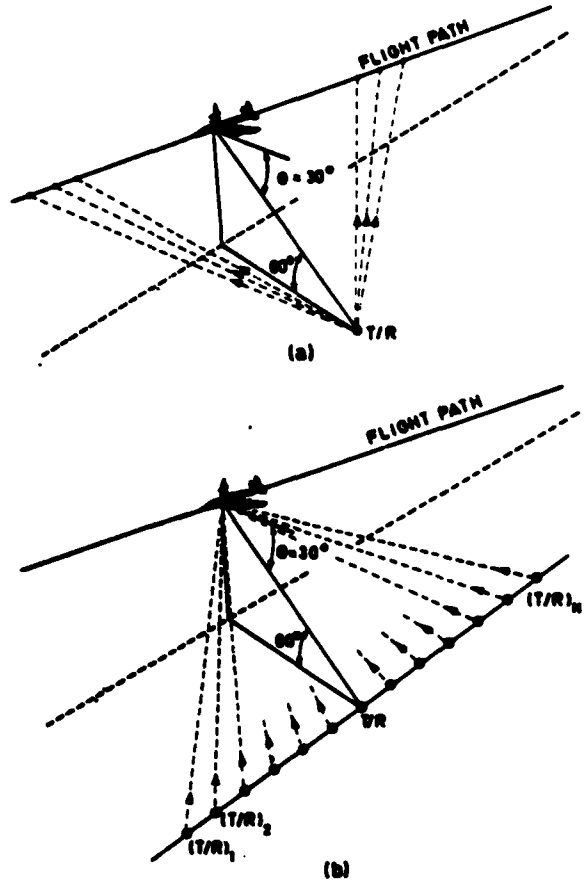

Figure 2. Imaging arrangements equivalent to that of Fig. 1. (a) Target synthesized aperture or inverse Synthetic Aperture Radar arrangement. (b) Imaging radar network arrangement.

In practice the measurement system of Fig. 1 can not measure $V(\bar{p},R)$ of eq. (1) directly. Instead the measurement is distorted by undesirable effects of clutter and measurement system response. Clutter is an additive signal component caused by reflections from the microwave absorber paneling covering the chamber walls, floor and ceiling and from any other present items such as the object mount and positioner. Also included in clutter is any direct signal leakage from the transmitting to receiving arms of the measurement system as, for example, through antenna coupling. System response represents the combined multiplicative effect of the frequency response of all measurement system components such as antennas, cables, amplifiers, etc. which can modify the measured values of $V(\bar{p},R)$. Error free determination of $\Gamma(\bar{p})$ requires, therefore, not only the phase-range normalization indicated in eq. (2), but also requires correction of the measured scattered field for clutter and system response. The most significant advantage of computer controlled auto-

mated microwave measurements, in addition to speed of data acquisition, is that such corrections can be carried out readily by the computer using algorithms that lead to the determination of $\Gamma(\bar{p})$ with an accuracy unattainable otherwise. One data correction procedure developed in our work and found to be quite effective enables the correction of the measured scattered field for both range-phase and system response simultaneously. The procedure uses the frequency response of a reference target of known linear phase dependence on frequency and of constant amplitude response. Both the conducting sphere and conducting cylinder satisfy this requirement over a wide range of bistatic scattering angles in their physical optics scattering regime where ka>1, a being the radius [16]. For both cases, the frequency dependence of the phase of the copolarized scattered field received at R relative to the phase of the transmitted signal at T can be represented by $\exp -jk[(R_T+R_R) - 2a\cos\alpha/2]$ where R_T and R_R are the distances between the phase centers of the transmitting and receiving antennas respectively and the center of the reference sphere or axis of the reference cylinder when either is used in place of the object in Fig. 1 [16]. The correction data for the results presented below were produced using a conducting cylinder as the reference target. The cylinder used was of diameter $2a = 7.5$ cm$>\lambda$ and length $\ell = 1m \gg \lambda$. A quantitative description of the procedure is given next. Let,

$$\Psi_m(\bar{p}) = kAe^{-jk(R_T+R_R)}\Gamma(\bar{p})H(p)+C(p) \qquad (5)$$

be the scattered field measured by the system of Fig. 1. Here A is a complex constant and H(p) and C(p) represent the multiplicative complex frequency response of the system and the additive clutter respectively. Note that H and C are functions of frequency alone though $p = 2k\cos\frac{\alpha}{2}$ and when polarization effects are taken into account that C(p) is also polarization dependent. Furthermore C(p) in eq. (7) contains implicitly the effect of the system response H(p) on the clutter measurement. The copolarized scattered field for a vertically oriented conducting reference cylinder whose axis coincides in Fig. 1 with the azimuthal axis of rotation is independent of aspect and is given therefore by,

$$\Psi_c(p) = kAe^{-jk(R_T+R_R)}e^{jk2a\cos\frac{\alpha}{2}}H(p)+C(p). \qquad (6)$$

If the reference cylinder is positioned with its axis displaced by an amount a in range from the axis of azimuthal rotation of the pedestal, the measured field of eq. (6) becomes,

$$\Psi_r(p) = kAe^{-jk(R_T+R_R)}H(p)+C(p). \qquad (7)$$

with the first term on the right hand side representing specular reflection at the leading edge of the cylinder which acts as a line scatterer positioned on the axis of azimuthal rotation. The copolarized scattered field of the displaced reference cylinder is seen to contain the required data correction terms: the range-phase term, the system response term and the clutter term. To effect data correction the clutter term C(p) is first measured by the system without any target in place and stored in computer memory. Then the reference cylinder is positioned as described above and the response (of eq.(7)) is measured and stored. The computer is then used to subtract C(p) from the previously measured and stored object frequency response of eq. (5) and from the stored reference response of eq. (7) to finally obtain the required object response from,

$$\Gamma(\bar{p}) = [\Psi_m(\bar{p}) - C(p)]/[\Psi_r(p) - C(p)]. \qquad (8)$$

The preceeding procedure has been tested in our studies and found to provide good results. However, it is frequently not practical or possible to locate the reference target in place of the scattering object in order to effect data correction for range-phase and system response simultaneously as described above. This is particularly true when the object is remote as in actual radar imaging situations. A procedure different than that indicated by eq. (8) is then needed. Therefore a more practical method in which the system response and the range-phase are determined separately was devised and applied in obtaining the imaging results presented in this paper. The method is novel in that it synthesizes a phase-reference on the target realizing thereby all the advantages of a TDR[3]-[6]. It is based on utilizing the available measured multiaspect frequency response data of the scattering object to determine the total path length (R_T+R_R) between the phase centers of the transmitting and receiving antennas to a selected phase reference point on the object. Clutter is measured exactly as before, however the reference target is utilized now only to determine the system response H(p). The path-length information for each "look" or viewing angle (aspect) of the object is obtained by Fourier inversion of the already available frequency response data after correcting it for clutter and system response. This provides the impulse response of the object for each viewing angle as a function of a spatial variable ξ proprotional to ct, c and t being the velocity of light and time respectively. Because plane wave illumination is utilized, the resulting "spatial" impulse response represents essentially the geometrical projection of the visible scattering centers of the object, weighted properly by their scattering strengths, on a line in the $\hat{\imath}_p$ direction. With the impulse response information in hand, the location of the *scattering centroid** of the object on the ξ axis is determined for each viewing angle and then used to estimate the range information (R_T+R_R) as will be described below. The accuracy of this method for determining range information is well known and is given by $c/2\Delta f$, Δf being the width of the spectral window utilized in data acquisition [20]. The last step in data correction, namely the range-phase normalization, can now be carried out to yield the desired $\Gamma(\bar{p})$. This last operation is in effect equivalent to an alignment or coalescing of the positions of the scattering centroids for the various viewing angles into a single phase reference point on the object that represents a synthetic TDR.

*This often coincides with the location of a dominant peak in the impulse response when there is a dominant scattering center on the object.

To put the above remarks on a quantitative basis we write from eq. (6),

$$H(p) = \frac{1}{kA} e^{-j\left(\frac{R_T+R_R}{2\cos\alpha/2} - a\right)p} [V_r(p) - C(p)]. \quad (9)$$

All quantities on the right side of this equation are known (from clutter data and measurements with the reference cylinder) with the exception of (R_T+R_R) which we determine by Fourier inversion of the known quantity,

$$G(p) = \frac{1}{kA}[V_r(p)-C(p)] = e^{-j\left(\frac{R_T+R_R}{2\cos\alpha/2}-a\right)p} H(p) \quad (10)$$

This inversion yields,

$$g(\xi) = \frac{1}{2\pi} \int G(p) e^{jp\xi} dp = \frac{1}{2\pi} h(\xi-\xi_c) \quad (11)$$

where $h(\xi)$ is the Fourier inverse of $H(p)$, and

$$\xi_c = (R_T+R_R)/2\cos\frac{\alpha}{2} - a \quad (12)$$

By taking ξ_c to equal the centroid of g (see Fig. 3) which is defined as,

$$\xi_c = \int \xi g(\xi)\, d\xi \;/\; \int g(\xi)\, d\xi \quad (13)$$

and equating eqs. (12) and (13) we can determine the range information (R_T+R_R) which can then be substituted in eq. (9) to yield the system response $H(p)$.

Figure 3. Plane wave impulse response representation used in defining the scattering centroid ξ_c.

Having determined $H(p)$ we can find $\Gamma(\vec{p})$ from eq. (5) as,

$$\Gamma(\vec{p}) = \frac{1}{kA} e^{-jk(R_T+R_R)} [V_m(\vec{p})-C(p)]/H(p) \quad (14)$$

Again we note that all quantities on the right side of this equation are now known from measurements except for the range information (R_T+R_R) of the object which will be aspect dependent since the scattering centroid is aspect dependent. This term can be determined as before by Fourier inversion of,

$$Q(\vec{p}) = [V_m(\vec{p})-C(p)]/H(p) = e^{-jk\left(\frac{R_T+R_R}{2\cos\alpha/2} - a\right)p} \Gamma(\vec{p}) \quad (15)$$

to first obtain the impulse response for each viewing angle and then to determine the distance of the scattering centroid for each look to find the corresponding (R_T+R_R) which can finally be used in eq. (14) to obtain $\Gamma(p)$.

An example of the $\theta = 30°$ slice of $\Gamma(\vec{p})$ of the B-52 test object extracted from the measured data by the above procedure is shown in Fig. 4(a).

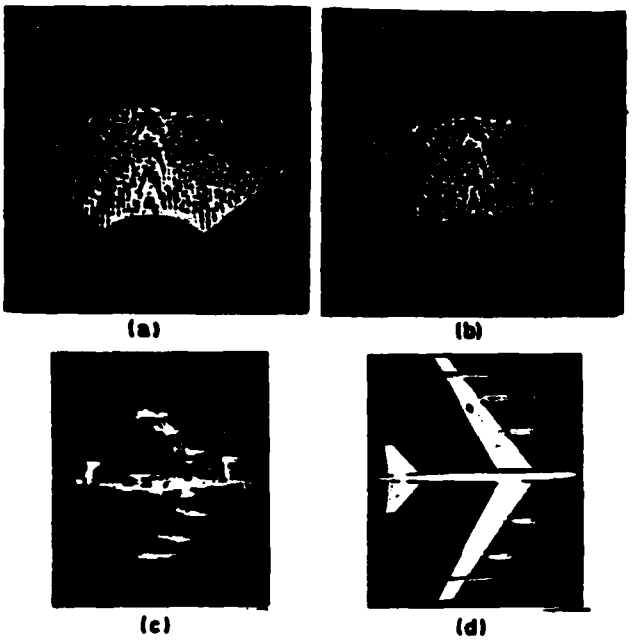

Figure 4. Results of projection imaging of B-52. (a) Slice of 3-D Fourier space of object. (b) Same slice in rectangular format obtained by interpolation. (c) Projection image showing characteristic scattering centers identifiable in the pictorial view (d).

This represents the real part of the slice data as displayed by the computer on a high resolution CRT display. Fourier inversion of the data in this slice should yield, as explained previously, a *projection image* representing the projection of the scattering centers of the object on a plane parallel to the plane of the $\vec{p}$-space slice. Digital Fourier inversion of the $\vec{p}$-space slice data requires its conversion first from the polar format in which it is originally acquired to a rectangular format suitable for application of the 2-D Fast Fourier transform. Conversion from polar to rectangular format was achieved by means of a weighted average of four nearest neighboring data points algorithm [17]. The result is shown in Fig. 4(b). Typical interpolation time on the MIMC 11/2 for the 16K complex data point of the $\vec{p}$-space slice was about 10 minutes. The result of applying the 2-D FFT to the interpolated data is shown in Fig. 4(c). This projection image is actually magnified in the vertical direction by a factor $1/\cos\theta = 1.155$ in order to obtain a properly scaled projection image of the scattering centers as they would be seen in a bottom view of the B-52 shown in Fig. 4(d). The same scaling effect can also be achieved by scaling (contracting) the slice hologram of Fig. 4(b)

in the vertical direction by the same factor $1/\cos\theta$ before interpolation and Fourier inversion. It is seen that prominent characteristic scattering centers of the B-52 e.g. engines, fuel tanks and fuselage are delineated clearly and in the correct geometrical relation and relative size to enable recognition and classification of the scatterer. The image resolution achieved is of the order of 2 cm and is in agreement with theoretical predictions[3].

Discussion

Several important conclusions and remarks can be drawn from the work presented.

(a) The principles and methods discussed show how to access the 3-D Fourier space of a nondispersively scattering object by angular and wavelength diversity. Although not specifically discussed in this paper, polarization diversity can also be employed to increase the amount of information in the accessed Fourier space.

(b) The accessing of the Fourier space is facilitated through the use of a novel synthetic target derived reference (TDR) technique whose advantages have been enumerated elsewhere [3]-[6] and whose effectiveness has been demonstrated here in the microwave regime. The TDR method has been used routinely in our tomographic and projective imaging of complex objects yielding unprecedented resolutions. The TDR technique results in a recording arrangement that yields what can be regarded as a 3-D lensless Fourier transform hologram.

(c) The first centimeter resolution microwave projection imaging of scattering centers of a complex conducting body from measured data is demonstrated. This is achieved by applying the projection-slice theorem to realistic microwave scattering data collected in our experimental microwave imaging facility.

(d) Projection imaging of characteristic highlights or scattering centers of a complex shaped object of the kind employed in this study is shown to provide sufficient geometrical image detail to enable identification.

(e) Centimeter resolution is demonstrated through the use of frequency diversity in the (6-17) GHz range and angular diversity over $\pi/2$ in the data acquisition and by using digital image reconstruction. Excellent microwave image quality is obtained from data contained in a single finite slice of the Fourier space accessed in an angular format of 128 equally spaced radial lines covering an angle of 90° with each radial line containing 128 complex data points. A study, not reported here, of the effect of angular aperture thinning and reduction, shows that reducing the number of radial lines (aspect angles) covering the 90° angular aperture from 128 to 64 hardly causes any noticeable change in image quality while narrowing the angular aperture to 45° does not degrade image quality to any significant degree that renders it unrecognizable.

(f) The retrieved image is nearly free of the speckle noise that plagues conventional coherent imaging systems [18] and particularly microwave imaging systems. Speckle noise suppression is attributed to wavelength diversity which tends to make the impulse response of a coherent imaging system change from bipolar (i.e. with negative sidelobes) to unipolar making it thus behave like a speckle free incoherent imaging system [19].

(g) The concepts described and verified in this paper show for the first time how a network of widely dispersed, extremely broadband, coherent radar stations can be used in a cooperative mode to produce 2-D projective images or 3-D tomographic images of distant aerospace objects with unprecedented resolution. This resolution can exceed the capabilities of optical imaging systems whose operation, unlike microwave systems, is severely hindered by atmospheric effects.

(h) The results presented here were obtained from data collected without having to maintain phase coherence from one angular frequency response measurement to another. This has important practical advantages when multiaspect interrogation of the scatterer with an array of broadband monostatic coherent transmitter/receiver elements is employed as the mode for data acquisition as envisioned in the proposed radar imaging network since it indicates that maintenance of phase coherence between the sources at the various stations is not required. This eliminates the need for reference signal distribution networks which are known to be a major obstacle in the realization of giant coherent microwave imaging apertures [5] because of economical and practical constraints on their implementation.

(i) Despite the fact that for the distance $R_T = 7m$ and scatterer size $L = .79m$ the receiving antenna position in Fig. 1 is hardly in the far field zone ($R > L^2/\lambda_{min}$) of the scatterer, high quality images were obtained using algorithms that stem from far field inverse scattering considerations. This seems to indicate that the imaging methods described here are applicable to intermediate range applications and possibly with some modifications to near field imaging situations.

(j) The Fourier space slice accessed by the measurements described here using our experimental microwave imaging facility is identical to the $\vec{p}$-space that one might access in the inverse SAR geometry of Fig. 2(a) or the imaging radar network geometry of Fig. 2(b). This can readily be verified by drawing the $\vec{p}$-space sampling format for these equivalent geometries to find that they are identical since both access the $\vec{p}$-space of the scatterer over the same range of aspect angles one doing so sequentially in time as the scatterer progresses in its flight and the other acquiring the same data simultaneously. The questions of $\vec{p}$-space acquisition in the presence of scatterer motion and simultaneous interrogation where "cross-talk" can be a problem in the arrangement of Fig. 2(b) have been considered in our work and will be addressed in a future publication.

(k) Customarily, the function $\gamma(\vec{r})$ is identified as the *characteristic function* of the scatterer defined as being unity within it and zero outside [7], [8]. The results presented here show that in practice γ can assume zero values on those parts of the scatterer's surface that are not seen by the system (i.e. do not scatter radiation in the direction of the observation point or points) such as the case of the flat wing sections and other gross detail in the example of the B-52 test object

utilized in this work.

(l) The two vertical wedges appearing in Fig. 4(c) are the projection image of the vertical plexiglass arms supporting the test object (see Fig. 1(a)). Since the clutter information used in the data correction procedure is obtained for a single positioner orientation in ϕ, it will remove the effect of all cylindrically symmetric features of the positioner that do not change with ϕ from the image such as the vertical plexiglass tubing but not the vertical plexiglass arms since these lack cylindrical symmetry. The imaging of the plexiglass arms is evidence of the effectiveness of the methods described here in imaging of composite (metalic/dielectric) bodies.

(m) Since scattering from a complex shaped object is polarization dependent, polarization selective measurements can readily be incorporated in the procedures described. This would yield a wavelength and polarization diversity imaging method capable of providing more information about the scattering object.

Acknowledgement

This research was supported by the Air Force Office of Scientific Research, Air Force Systems Command under Grant No. AFOSR-81-0240B and by the Army Research Office under contract DAAG29-80-K-0024P02.

References

1. N.H. Farhat, "Longwave Holography" in *Holography in Medicine*, P. Gregnss (Ed.), IPC Science and Technology Press, Richmond (England), 1975.

2. N.H. Farhat, et. al., "Real-Time Microwave Holography - A Feasibility Study", University of Pennsylvania Report - Prepared for University Science Center Inc., Oct. 1972.

3. N.H. Farhat and C.K. Chan, "Three-Dimensional Imaging by Wave-Vector Diversity", Presented at the 8th Int. Symp. on Acoust. Imaging, Key Biscayne, Fla., 1978 and published in *Acoustical Imaging*, Vol. 8, A. Metherell (Ed.), pp. 499-516, Plenum Press, New York 1980.

4. C.K. Chan and N. Farhat, "Frequency Swept Tomographic Imaging of Three-Dimensional Perfectly Conducting Objects", IEEE Trans. on Ant. and Prop., Special Issue on Inverse Methods in Electromagnetics, Vol. AP-29, pp. 312-319, March 1981.

5. N.H. Farhat, W.I. Landauer and W.E. Wallace, "Computer Assisted Naval Applications of Holography", Computer Command and Control Co., Report No. 132-4, prepared for Naval Analysis Programs, Office of Naval Research under contract No. N0014-69-C-0167, February 1973.

6. N. Farhat, C.K. Chan and T.H. Chu, "A Target Derived Reference Technique for Frequency Diversity Imaging", North American Radio Science Meeting, Quebec, 1980.

7. N. Bojarski, "Inverse Scattering", Naval Air Command Final Report N000 19-73-C-0312F, Feb. 1974.

8. R.M. Lewis, "Physical Optics Inverse Diffraction", IEEE Trans. on Ant. and Prop., Vol. AP-17, pp. 308-314, May 1969.

9. N.H. Farhat and C.L. Werner, "An Automated Microwave Measurement Facility for Three Dimensional Tomographic Imaging by Wavelength Diversity", presented at the 1981 Intern. IEEE AP-S Symp./National Radio Science Meeting, L.A., June 1981.

10. J. Radon "Über die Bestimmung von Fonktionen Durch ihre Integraldwerte Längs Gewisser Mannigfaltigkeiten" Ber. Saechs. Akad. Wiss. (Leipzig), Vol. 19, pp. 262-278, 1917.

11. R.N. Bracewell, "Strip Integration in Radioastronomy", Australian J. of Phys., Vol. 9, pp. 198-217, 1956.

12. G. Stroke and M. Halioua, "Three-Dimensional Reconstruction in X-ray Crystallography and Electron Microscopy by Reduction to Two Dimensional Holographic Implementation", Trans. Amer. Crystal. Assoc., Vol. 12, pp. 27-41, 1976.

13. H.H. Barrett and W. Swindle, *Radiological Imaging: Theory and Image Formation, Detection and Processing*, Academic Press, New York 1982.

14. Y. Das and W.M. Boerner, "On Radar Shape Estimation Using Algorithms for Reconstruction From Projections", IEEE Trans. on Ant. and Prop., Vol. AP-26, pp. 274-279, March 1978.

15. A.J. Rockmore, R.V. Denton and B. Friedlander, "Direct Three-Dimensional Image Reconstruction", IEEE Trans. on Ant. and Prop., Vol AP-27, pp. 239-241, March 1979.

16. G.T. Ruck *Radar Cross Section Handbook*, Plenum Press, New York 1970.

17. R.M. Mersereau and A.V. Oppenheim, "Digital Reconstruction of Multidimensional Signals From their Projections", Proc. IEEE, Vol. 62, pp. 1319-1338, October 1978.

18. J.C. Dainty (Ed.) *Laser Speckle*, Springer-Verlag Berlin, (1975).

19. N.H. Farhat and C.K. Chan, "Super-resolution by Wavelength Diversity in Longwave Imaging", in Optica Hoy Y Mañana Proc. ICO-11 Conference J. Bescos et.al. (Eds.), Inst. De Optica-Sociedad Española De Optica, Madrid 1978.

20. N.H. Farhat, "High Resolution Longwave Frequency Swept Holographic Imaging", 1975 Ultrasonics Symposium Proc., IEEE Cat #75CH0994-4SU.

APPENDIX VIII

TOMOGRAPHIC IMAGING OF DIELECTRIC BODIES

TOMOGRAPHIC IMAGING OF DIELECTRIC BODIES

This task of our research program is concerned with the ability to image dielectric and composite bodies using the λ and polarization diversity imaging techniques developed in our work. There are several reasons for this concern. One is the fact that many objects of interest in remote imaging are composite in nature i.e., they contain conducting, semi-conducting, or dielectric parts. Another is the important role that can be played by an effective means of 3-D visualization in nondestructive evaluation (NDE). Microwave and millimeter wave (mmw) visualization of internal defects and flaws can be particularly important in materials that do not lend themselves to inspection by ultrasound techniques such as large solid propellant grains*. Preliminary results of (6-17) GHz microwave projection imaging of a dielectric test object consisting of two concentric cylindrical tubings of .3 cm wall thickness and inner and outer cylinder diameters of 4.750 cm and 29.70 cm respectively are given in Fig 1. The object was mounted on an elevation-over azimuth positioner as shown in the top photographs of Fig. 1 and horizontal plane slices of its Fourier space where accessed over an azimuthal angle range of $0 \leq \phi \leq 360°$ for different values of elevation angle θ (= 0°, 20°, 30°). Since a single Fourier space slice is measured, the images retrieved from it by Fourier inversion will, in accordance to the projection-slice theorem, correspond to projections of the object scattering function on a plane parallel to the projection plane. Such projections are shown in the second row of Fig. 1 for the three values of θ chosen.

* R.W. Cribbs and B.L. Lamb, "Resolution of Defects by Microwave Holography", Proc. of the Engineering Applications of Holography Symposium, conducted for ARPA by TRW Systems Group, Los Angeles, Feb. 1972.

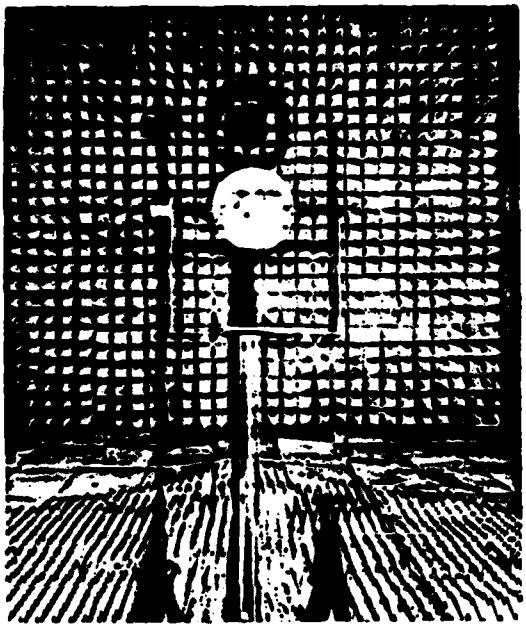

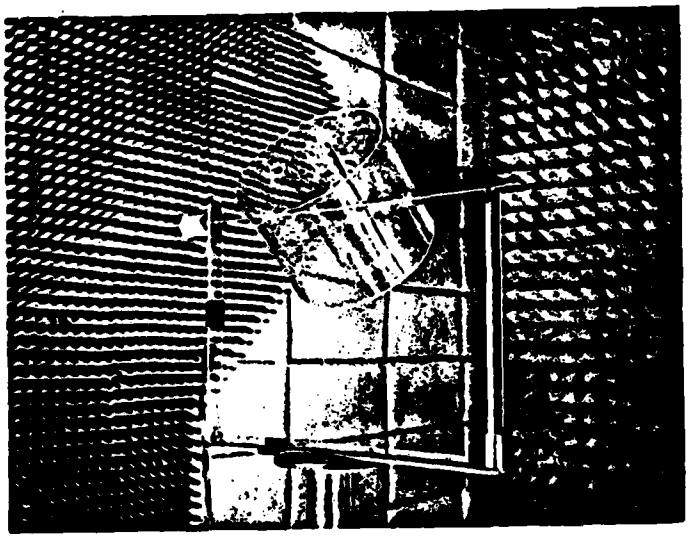

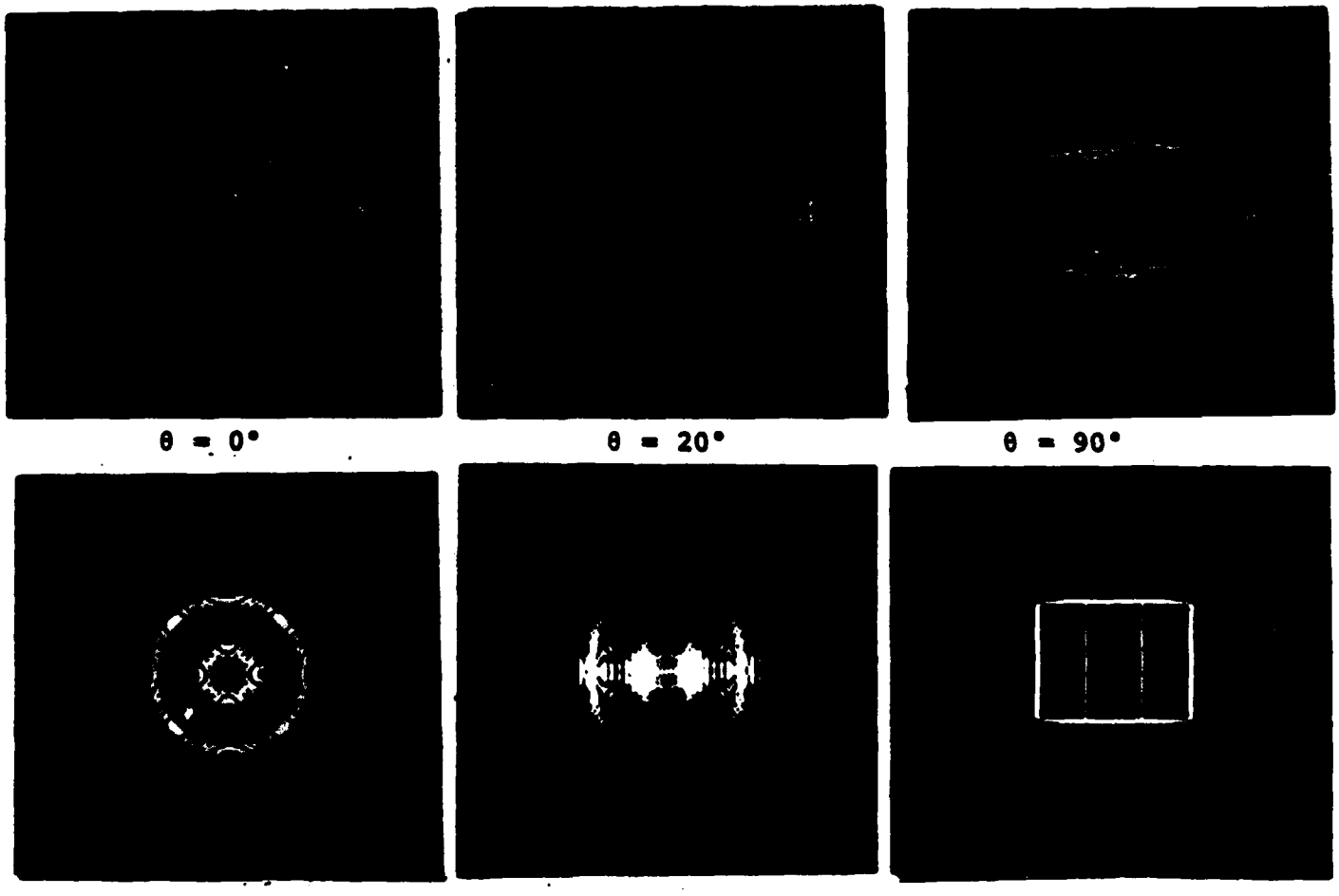

Fig. 1. Results of microwave tomographic imaging of two concentric plexiglass cylinders shown in the two views of the top row mounted on elevation-over-azimuth positioner. Second row - Digital reconstruction from Fourier space slices obtained using a 6-17 GHz spectral window and 360° angular aperture. Bottom row - Digital reconstruction from equivalent computer simulation. θ is the angle between the cylinder axis and the vertical.

The projection images shown are seen to have adequate resolution for identification of gross detail but obviously not for the identification of other features such as possible voids, cracks, delaminations and other fine detail and imperfections of interest in NDE which would require higher mmw resolutions. Also shown for comparison (bottom row of Fig. 1) are the results of a computer simulation. It is seen that good agreement exists between the experimentally and numerically obtained results.

APPENDIX IX

PROJECTION IMAGING OF INCOHERENT OBJECTS

PROJECTION IMAGING OF INCOHERENT OBJECTS

Theoretical considerations show that the concept of 3-D tomographic imaging by wavelength diversity is extendable to incoherent radiation and thus to thermally emitting objects [1]. Verification of this concept can lead to true passive 3-D imaging (radiometry or thermography) capabilities with important implications in surveillance, remote sensing and possibly radio-astronomy. Specifically we have shown, [1], that spectrally selective cross-correlation measurements or equivalent cross-spectral density measurements of the random wavefield emitted by a 3-D incoherent source of brightness distribution $b(\bar{r})$ can be employed to access the 3-D Fourier space $B(\bar{p})$ of the emitter where $\bar{p} = k(\bar{1}_{R_1} - \bar{1}_{R_2})$. $\bar{1}_{R_1}$ and $\bar{1}_{R_2}$ being unit vectors from an origin in the object in the directions of the observation points located at $\bar{r}_1$ and $\bar{r}_2$ and k being the wavelength (central wavelength of the synchronously tuned filters used to achieve spectral selectivity in the correlator arms).

Successful verification of the concept was achieved recently employing acoustic noise emission rather than microwave emission because of easier and less costly implementation. Because of the large ratio of velocity of light to velocity of sound ($\approx 10^6$) the same wavelength ranges of interest in incoherent microwave frequencies can be achieved with sound frequencies that are 10^6 times lower i.e., sound spectra in the KHz range.

Two acoustive measurement systems have been implemented to experimentally verify and study 3-D interferometric imaging of incoherent objects. Both measure the cross-spectral power density. One directly by spectrally selective cross-correlation measurements (see Fig. 1) and the other indirectly (see Fig. 2) by measuring the coherence function $\Gamma(\bar{r}_1, \bar{r}_2, \tau)$ first, then Fourier trans-

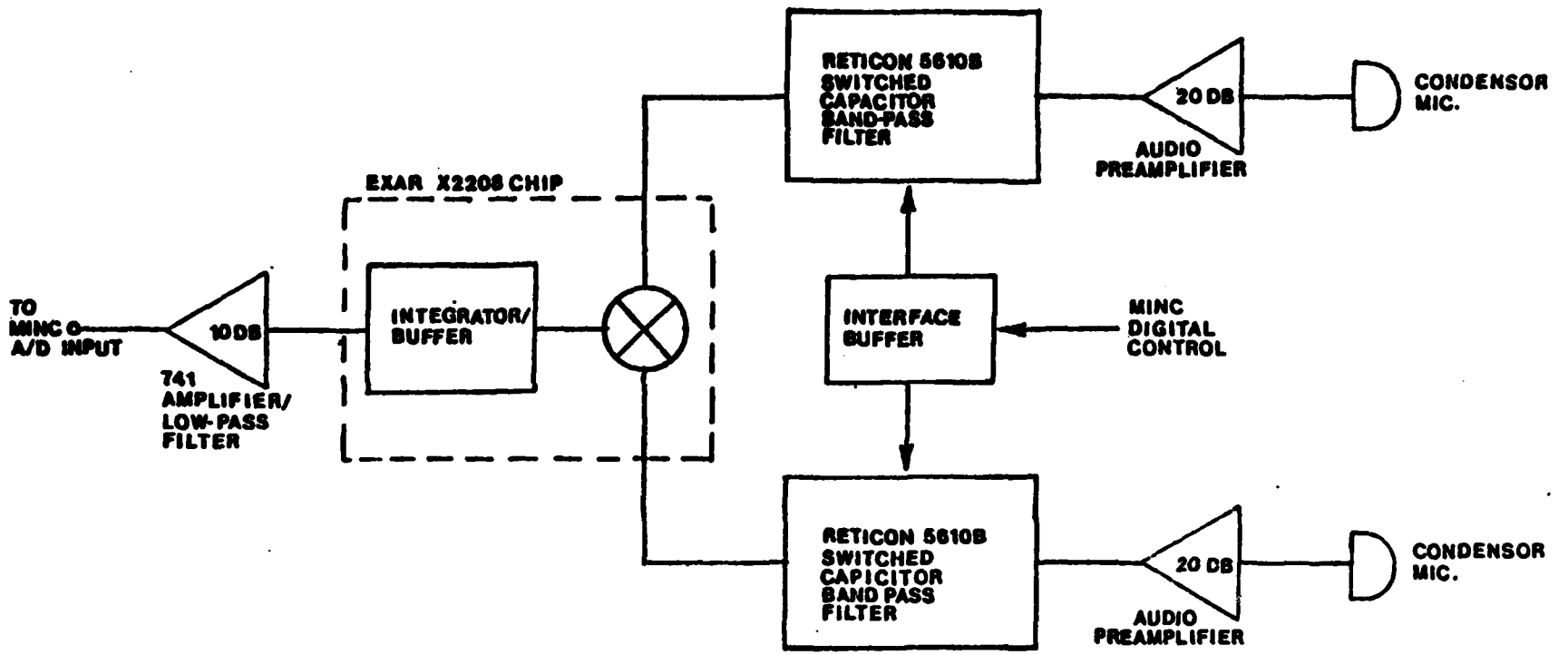

Fig. 1. System for 3-D imaging of incoherent acoustic objects by automated spectrally selective cross-correlation measurement in the (4 - 18) KHz acoustic range.

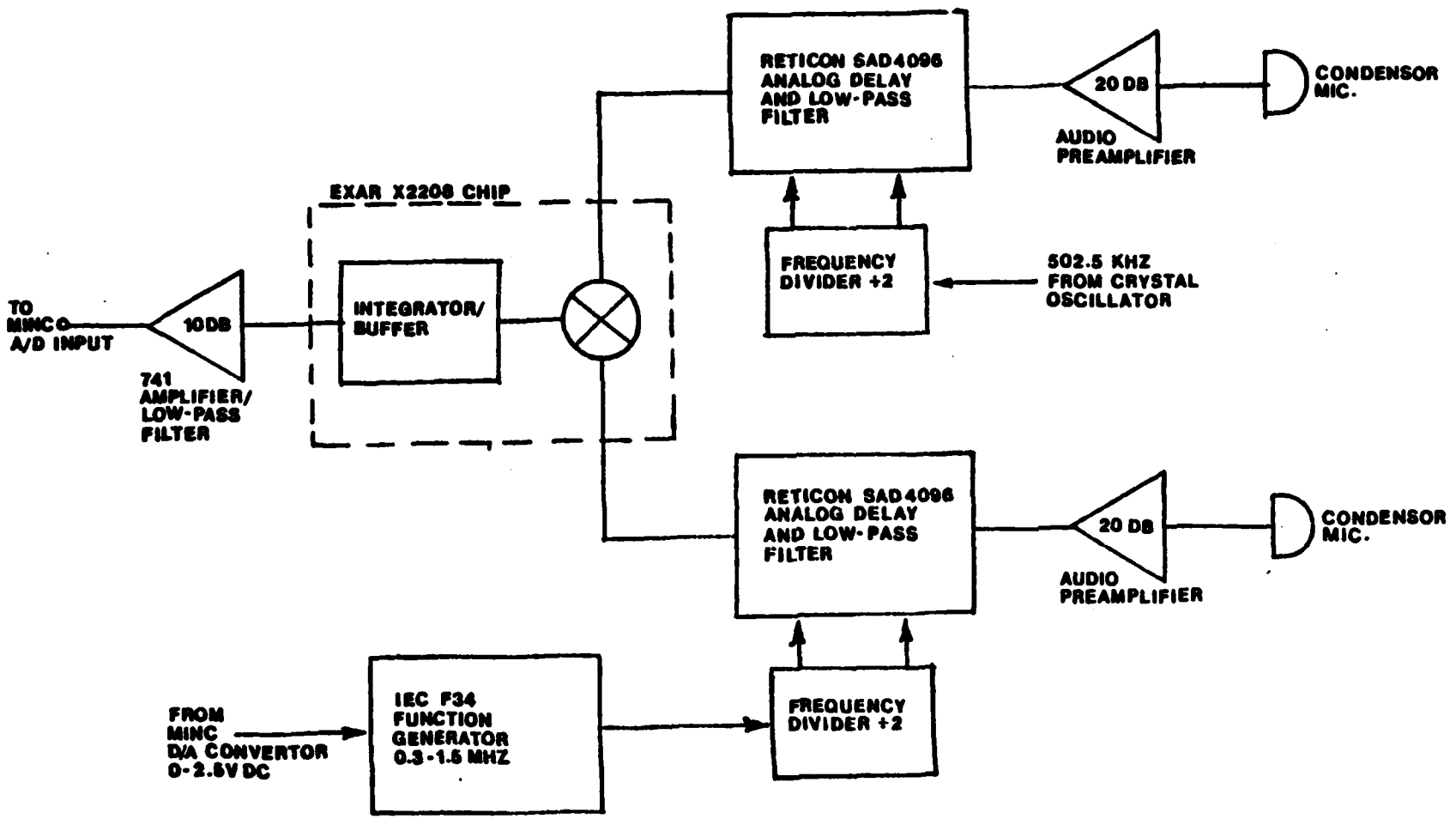

Fig. 2. System for automated measurement of the coherence function of an incoherent acoustic source in the (4 - 18) KHz.

forming $w \cdot r$ to τ, where $\bar{r}_1$ and $\bar{r}_2$ being the position vectors of the transducers. The receiving transducers in both systems are wide-band condenser microphones each located approximately 8 meters from the object. The angle between them as seen from the object is approximately 60°. The object itself consists of 5 dome tweeters arranged in a 3-D array on top of an azimuth positioner (rotating pedestal). The rotation of the pedestal is controlled by a MINC 11 Computer which coordinates system data acquisition and storage.

The first system shown in Fig. 1 utilizes digitally controlled dual switched capacitor band-pass filters that select quasimonochromatics bands of the received signals. The Q of these filters is on the order of 200 which implies a 50 Hz bandwidth at 10 KHz. The filter outputs are multiplied and integrated to form an estimate of the cross-spectral density. The second system is based upon measurement of the mutual coherence function. By the well known Weiner-Kinchin Theorem the cross-spectral power density and the mutual coherence function are a Fourier transform pair. Hence knowledge of the former leads to determination of the latter via a discrete Fourier Transform. This system is shown in Fig. 2. It utilizes two CCD20 48 stage bucket brigade devices in order to achieve a programmable analog delay. The MINC 11 Computer can program the delay time in 7μs increments. The mutual coherence function is measured by chinging the delay in one channel relative to the other channel. The product of the two channels is then integrated to yield an estimate of the coherence function. The width of the correlation peak resulting from a point source is inversely related to the bandwidth of the systems which in turn determines the range resolution. System resolution is found to be on the order of 1.5 cm. An example of a measured cross-correlation function of an incoherent point source, a single dome tweeter, is shown in Fig. 3. This was obtained with the arrangemeut of Fig. 2.

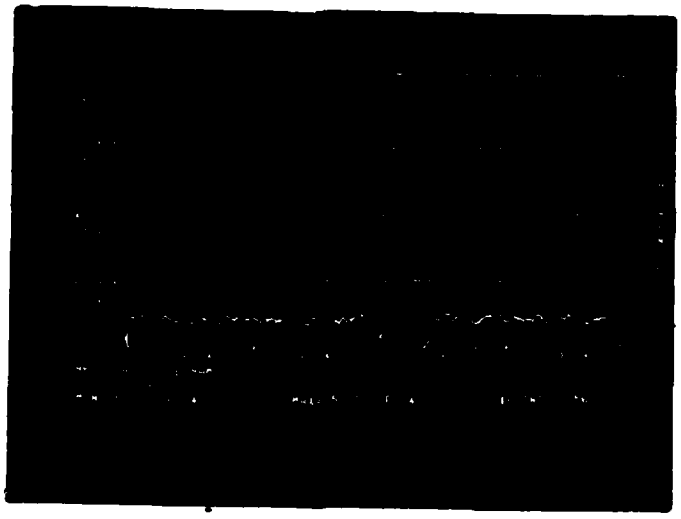

Fig. 3. Results of a cross-correlation measurement of an incoherent point source.

In order to obtain a three dimensional image of the 3-D test object described earlier the multiaspect cross-spectral density must be measured over as large a volume of Fourier space as possible. Successive slices of the object can then be retrieved using Fourier's domain projection theorems.

Recently, single slices or *correlograms* of the 3-D Fourier space $\overline{B}(\overline{p})$ of the incoherent test object were obtained. These correlograms were employed in a digital reconstruction scheme identical to that used in the reconstruction of our wavelength diversity holograms to produce the first projection images of a 3-D incoherent object.

The results to be described below show the validity of applying the projection-slice theorem (see Appendix VI) in the context here and are therefore indicative of the feasibility of tomographic imaging of 3-D incoherent objects from cross-spectral power density data. Note that our work differs from

medical radio-emissive tomography that is based on flux density measurements that are noninterferometric in nature.

Pictorial views of the measurement system utilized are given in Fig. 4(a). The 3-D noise emitting object, shown in Fig. 4(b), was realized using a 3-D formation of five acoustic tweeters as mentioned earlier excited from independent random noise generators in the (.6 - 13.5) KHz range. The tweeter assembly is mounted on a computer controlled azimuthal positioner that is used to change their azimuthal angle ϕ relative to the sensors. The random wavefield produced was transduced at two points in space separated as seen from the object by angle $\theta \simeq 60°$ with the aid of two condenser microphones shown in Fig. 4(c) and the cross-spectral power density of their outputs was obtained using the indirect arrangement of Fig. 2.

The correlogram recorded when only two of the five tweeters, indicated in the top view given in Fig. 5(a), were excited is shown in Fig. 5(b)

Figure 5(b) is the real part of the correlogram as recorded by changing ϕ in Fig. 5(a) over a range of 180° in 196 steps and plotting the measured cross-spectral density radially over a range equivalent to the (.6 - 13.5) KHz spectral window utilized. The correlogram consists of 196 radial lines each consisting of 48 frequency points and represents the data in a slice of the Fourier space of the object. A digitally interpolated version of this correlogram was obtained by a four-nearest-neighbors algorithm [2]. In accordance with the projection-slice theorem, Fourier inversion of the data in this slice should yield a projection image of the brightness distribution of the source as projected on a plane parallel to that of the slice. The results of 2-D digital Fourier inversion of the correlogram slice of Fig. 5(b) after interpolation is shown in Fig. 5(c). This preliminary result

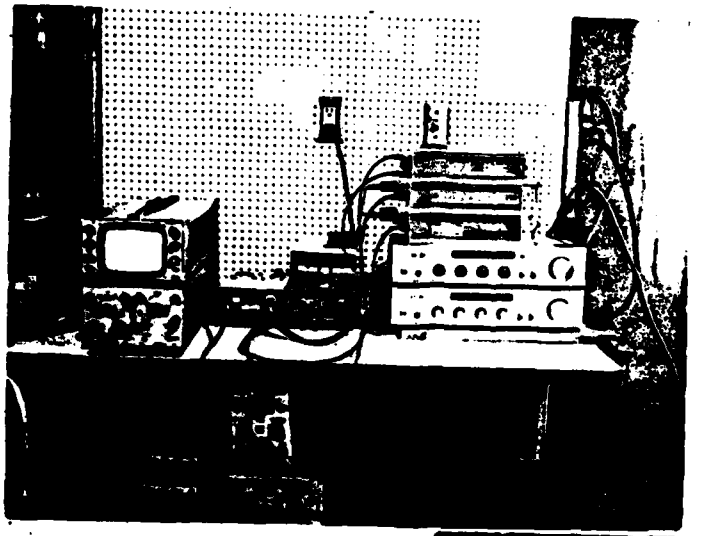

(a)

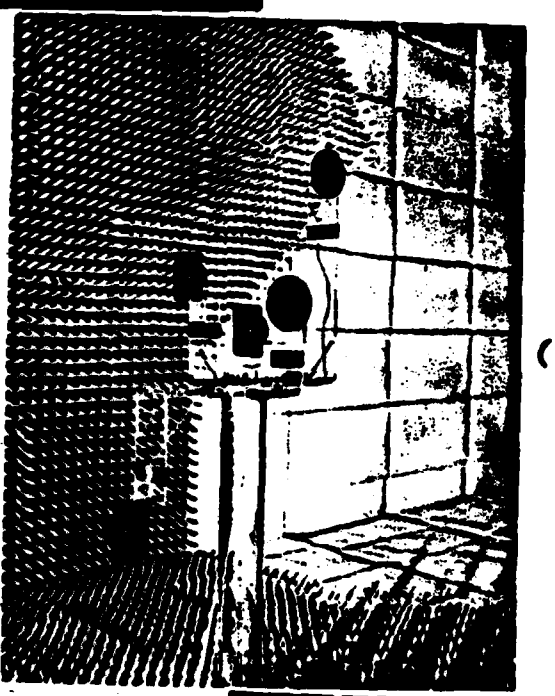

(b)

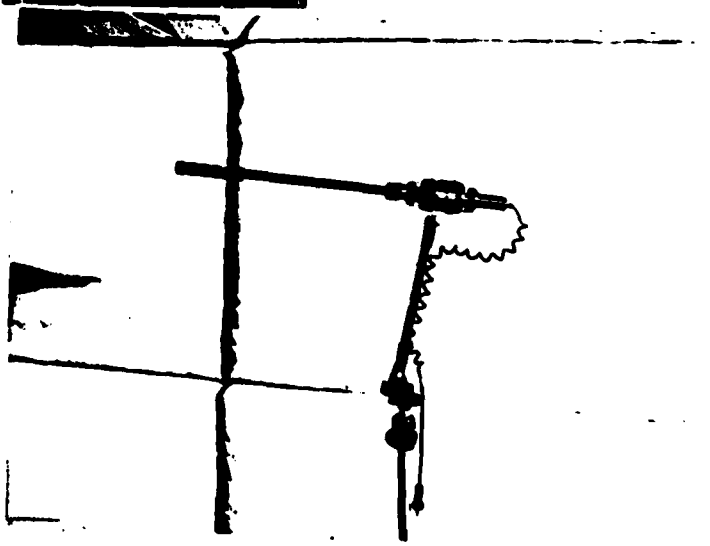

(c)

Fig. 4. Pictorial detail of measurement system employed in accessing a slice of the 3-D Fourier space of an incoherent 3-D acoustic source. (a) Instrumentation including amplifiers, programmable delays and multiplier. (b) View of 3-D distribution of five acoustic noise emitters (tweeters). (c) View of one of the two condenser microphones used for sensing the random acoustic field in the (.6 - 13.5) KHz range.

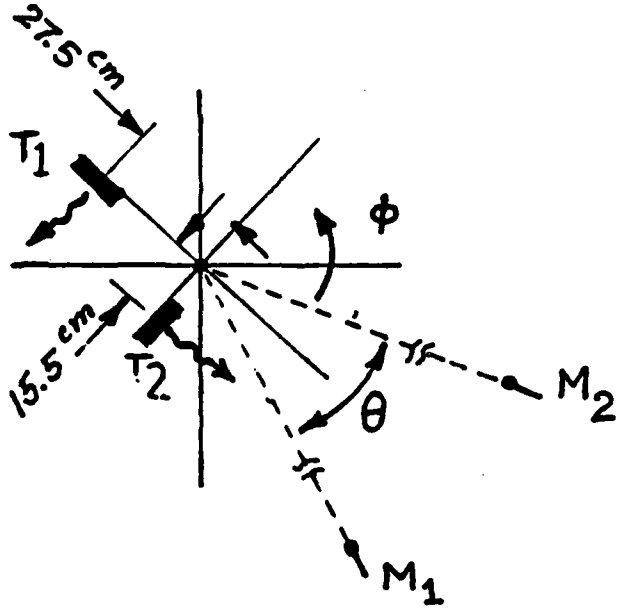

(a)

(b)

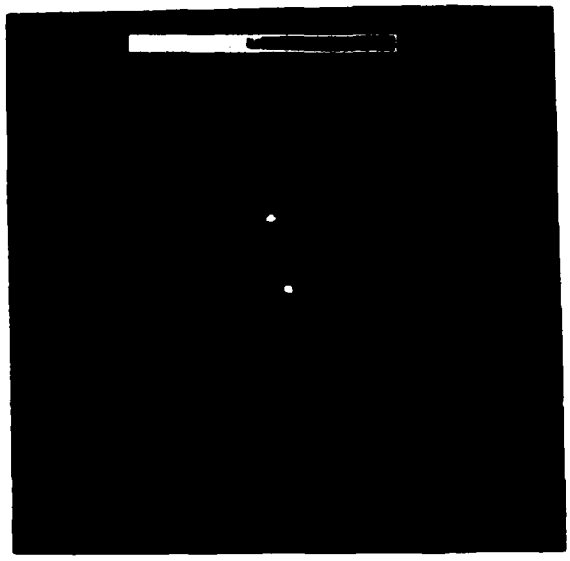

(c)

Fig. 5. Results of the first wavelength diversity correlation imaging experiment of two acoustic noise emitters (tweeters) in the (.6-13.5) KHz range. (a) Top view of source geometry (T_1 and T_2) relative to transducer microphones (M_1 and M_2). (b) Real part of *Correlogram* and (c) Digitally retrieved projection image.

represents the first successful experimental verification of the concept of projective imaging of 3-D detail of an incoherently emitting object employing spectrally selective cross-correlation measurements or equivalent cross-spectral density measurement. The results pave the way to true 3-D tomographic imaging of such objects and raise intriguing questions on the 3-D object information content in random wave-fields produced by thermally emitting objects.

References

1. N.H. Farhat, "High Resolution 3-D Tomographic Imaging by Wavelength and Polarization Diversity", University of Pennsylvania Research Proposal, Submitted to Air Force Office of Scientific Research, March 16, 1982.

2. R.M. Mersereau and A.V. Oppenheim, "Digital Reconstruction of Multidimensional Signals From Their Projections", Proc. IEEE, Vol. 62, pp. 1319-1338, October 1978.

APPENDIX X

SPECKLE SUPPRESSION BY WAVELENGTH DIVERSITY

SPECKLE SUPPRESSION BY WAVELENGTH DIVERSITY

Considerable progress in the understanding of speckle, its use, and its elimination has been achieved (see for example [1]-[4]) following the advent of the laser when the observation of speckle and its related phenomena became a routine everyday occurrence. This progress has resulted in good understanding of the statistics of speckle patterns formed in polarized monochromatic electromagnetic fields. These are shown to result from a classical random walk in the complex plane with the resulting irradiance fluctuations obeying a negative exponential law and the contrast of the speckle pattern, defined as the ratio of the standard deviation to the mean, being equal to unity [8]. Examples of millimeter wave images illustraing the deleterious effect of speckle on image quality and effective resolution are shown in Figs. 1 and 2. Most methods for the reduction of speckle [1],[2],[3]-[8] rely on either frequency diversity, spatial or angular diversity, or polarization diversity all of which are naturally present in wavelength and polarization diversity imaging. In particular the effect of wavelength diversity in suppressing speckle can be explained in terms of decorrelation of the speckle patterns at the various recording frequencies making thus the effect of speckle on the recorded data resemble that of random noise. It can be appreciated from this brief discussion of speckle that the wavelength and polarization diversity imaging method has inbuilt mechanisms for suppressing speckle noise. This leads us to expect that the reduction by speckle of the information content of obtained images should not be excessive. This speckle combating capability is one of the most significant features of wavelength and polarization diversity imaging allowing it to combine the best of two worlds, the world of incoherent imaging where speckle noise is nonexistent and the world of coherent imaging where sensitive heterodyne detection techniques and versatile data acquisition and processing is available.

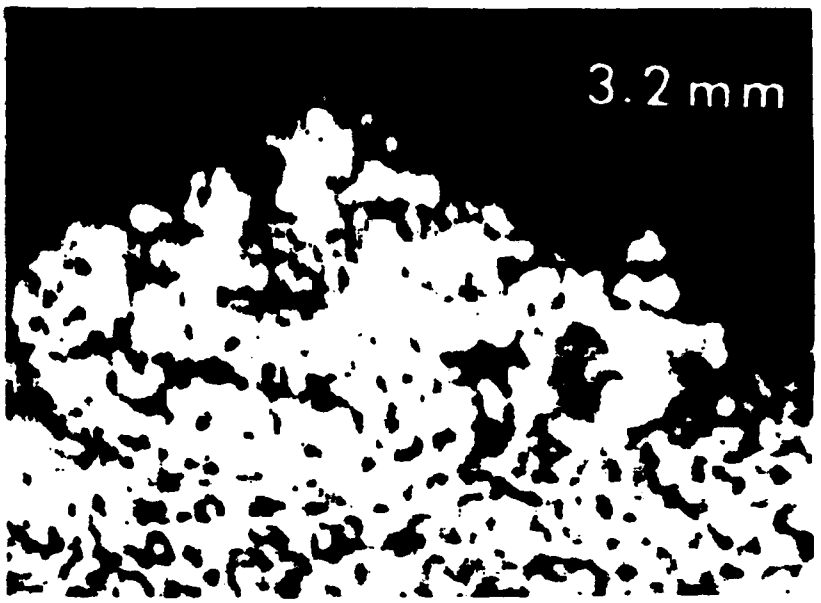

Fig. 1. 90 GHz (λ = 3.2mm) radar image of an M-48 tank showing deleterious effect of speckle. [From Ref. 12]

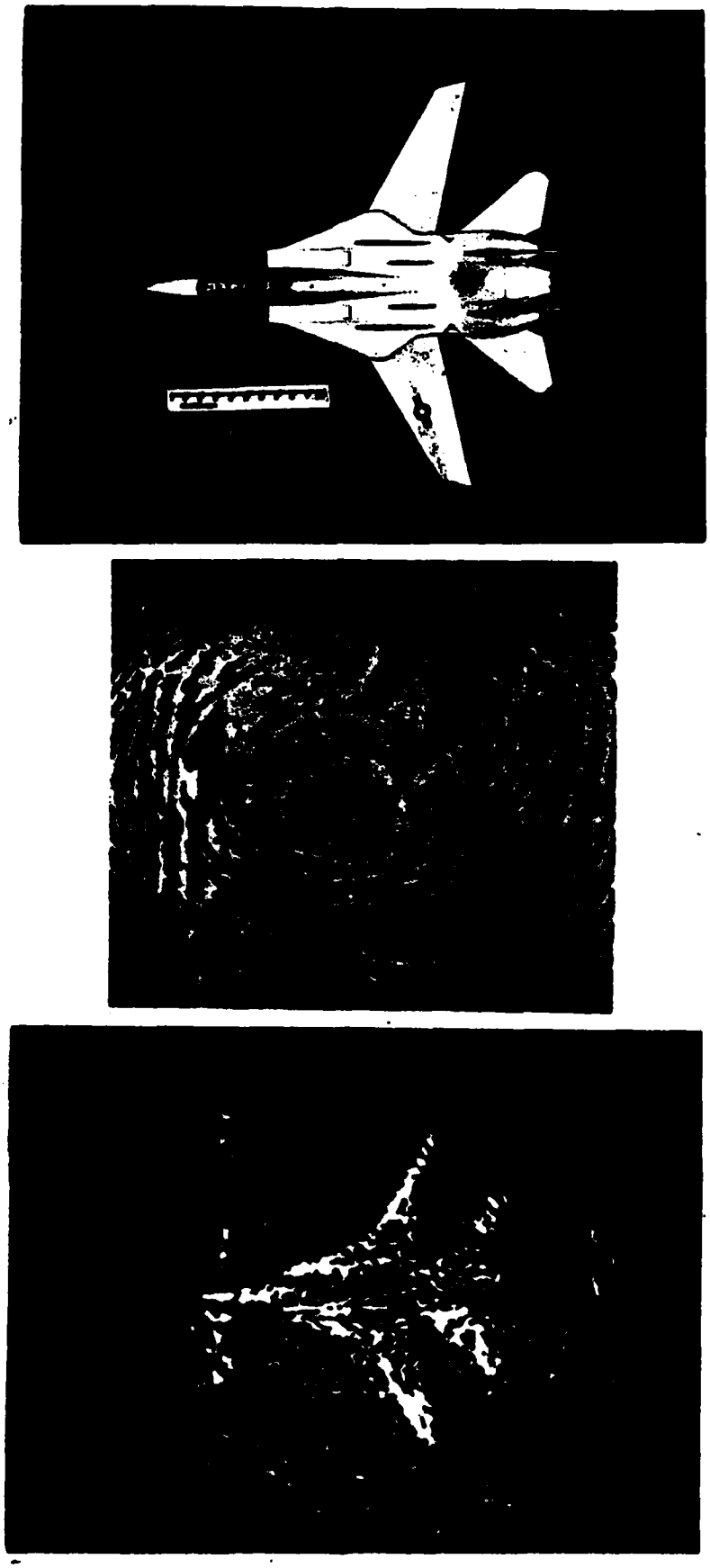

Fig. 2. 70 GHz (λ = 4.3mm) scanned T/R imaging of a 1:64 scale model of an F-14 aircraft. From top to bottom: object, hologram, and retrieved image degraded by speckle or coherent noise.

Our research program calls for closer examination of the effect of speckle noise on information content. Therefore to understand the role of wavelength diversity in suppressing speckle we consider an ideal λ-diversity imaging situation in which the $\bar{p}$-space of the object is accessed over a ball of radius $p_o = 2k_o$ by monostatic multiaspect interrogation of a scattering object over an angular aperture of 4π[sr]. The volume of this ball in Fourier space is represented by,

$$H(\bar{p}) = \begin{cases} 1 & \ldots\ldots\ p < p_o \\ 0 & \ldots\ldots\ \text{elsewhere} \end{cases} \tag{1}$$

The 3-D impulse response or *point spread function* (PSF) obtained by 3-D Fourier transformation of eq. (1) is [9],

$$h(\bar{r}) = \frac{4\pi p_o^{\,3}}{(p_o r)^2} \{\text{sinc } (p_o r) - \cos (p_o r)\} \tag{2}$$

and is seen to be spherically symmetric. In eq. (2), $\bar{r}$ is a position vector in spatial domain. In comparison $H(\bar{p})$ for a spherical shell in $\bar{p}$-space of radius $p=p_o$ and unit strength can be described by [9],

$$H(\bar{p}) = \begin{cases} \dfrac{1}{4\pi p_o^{\,2}\,\varepsilon} & \ldots\ldots\ p_o < p < p_o + \varepsilon,\ \varepsilon \ll p_o \\ 0 & \ldots\ldots\ldots\ \text{elsewhere} \end{cases} \tag{3}$$

which can be accessed by using monochromatic radiation at wavenumber $k_o = p_o/2$ and angular diversity of 4π[sr]. Fourier inversion of eq. (3) yields, the 3-D PSF,

$$h(\bar{r}) = \text{sinc } (p_o r) \tag{4}$$

Equation (2) can be utilized to determine the 3-D PSF of a spherical shell in $\bar{p}$-space extending from p_1 to $p_2 > p_1$ by simply replacing p_o in eq. (2) by p_2 and p_1 respectively and subtracting the two resulting expressions. This procedure can be also extended to evaluation of the PSF of a series of concentric $\bar{p}$-space spherical shells of arbitrary thickness arising when frequency diversity measurements extending over several available nonoverlapping frequency bands.

Using the above results the PSF for monochromatic and broadband (wavelength diversity) imaging systems operating in different regions of the μwave and mmw spectrum were computed. The results are shown in Figs. 3 and 4. In Fig. 3(a), the monochromatic 18 GHz PSF (inner curve) and the broadband (2-18) GHz PSF (outer curve) are compared. Similar results are shown in (b) and (c) for 17 GHz versus (6-17) GHz and 40 GHz versus (2-40) GHz. The 3 dB width Δr_{3dB}, first zero crossing Δr_{zero}, and the first sidelobe level for all these cases are summarized in Table I. It is evident from the results shown that wavelength or frequency diversity results in a slight broadening of the PSF but has the important effect of suppressing the sidelobes of the PSF as compared with those for the monochromatic shortest wavelength (or highest frequency) in each case. The degree of sidelobe suppression is greater the smaller the value of the lower bound on the frequency spectrum utilized. Of significance is the fact that the PSF for the (2-18) GHz and the (2-40) GHz cases is essentially unipolar, i.e., they are essentially positive real as for *incoherent* imaging systems that exhibit no speckle noise. Similar behavior is exhibited in Fig. 4 and Table II which present similar results for the PSF of several idealized monochromatic and broadband imaging systems operating in the (18-96) GHz range. The broadband (18-96) GHz case is computed for three non-overlapping waveguide bands where travelling wave tube amplifiers are commercially available. These results show that high resolution speckle free wavelength diversity imaging is possible through the use of broad frequency bands with small lower frequency limit.

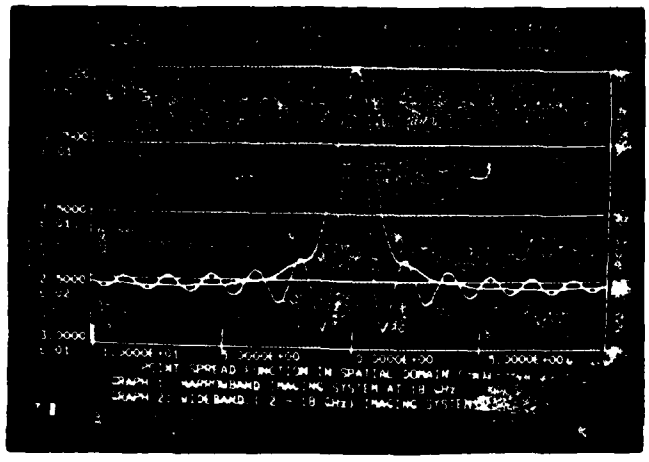

(a)

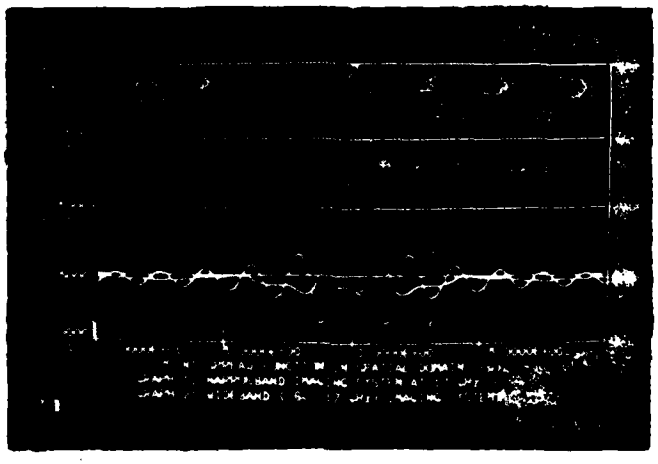

(b)

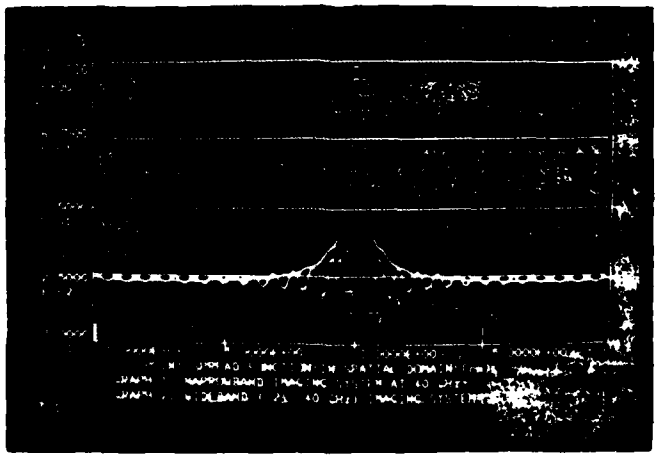

(c)

Fig. 3. Computed PSF of several idealized monochromatic and broadband imaging systems operating in the (2-40) GHz range.

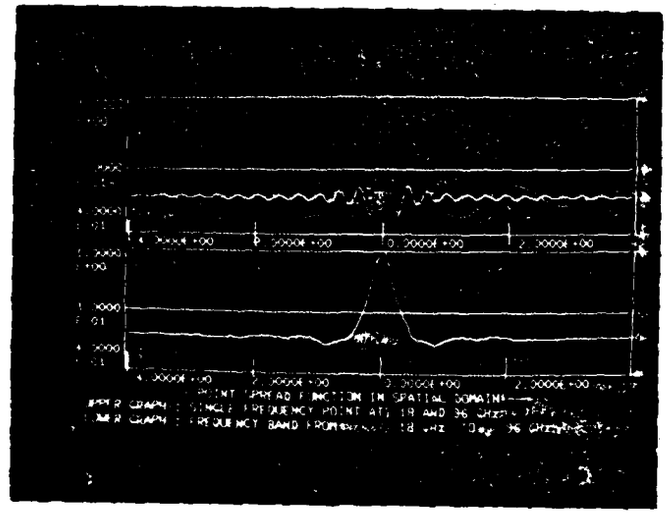

(a)

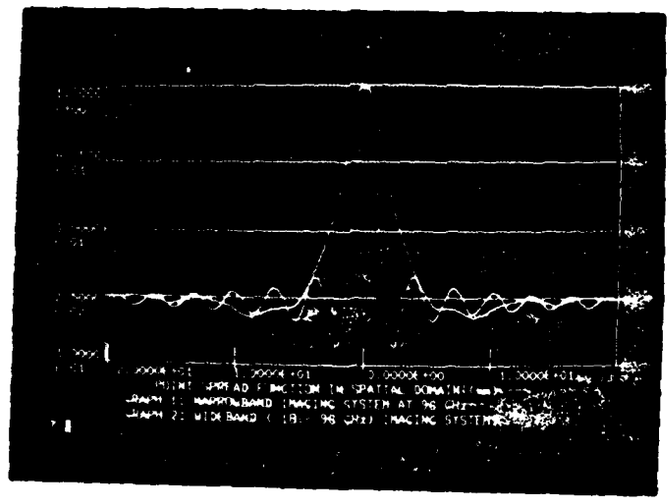

(b)

Fig. 4. Computed PSF of several idealized monochromatic and broadband imaging systems in the (18-96) GHz range. The (18-96) GHz range is covered in three nonoverlapping bands specified in Table II.

	18 GHz	(2-18) GHz	17 GHz	(6-17) GHz	40 GHz	(2-40) GHz
Δr_{3dB} [cm]	.74	1.27	.78	1.12	.33	.58
Δr_{zero} [cm]	1.67	9.13	1.75	2.68	.75	9.76
1st side lobe level [dB]	-13.4	-42.5	-13.4	-23	-13.4	-46

Table I. Comparison of PSF of several idealized monochromatic and broadband coherent imaging systems in the (2-40) GHz range.

	18 GHz	96 GHz	(18-96) GHz in Three Frequency Bands
			18 — 40 — 49.5 — 58 — 91 — 96
Δr_{3dB} [mm]	7.37	1.38	2.5
Δr_{zero} [mm]	16.67	3.125	10.7
side-lobe level [dB]			
1st	-13.4	-13.4	-23
2nd	-18	-18	-36./

Table II. Comparison of PSF for several idealized monochromatic and broadband coherent imaging systems in the (18-96) GHz range.

Finally in this section it is worth pointing out that the PSFs of the solid sphere (ball) and the spherical shell sampling formats in $\bar{p}$-space described by eqs. (2)-(4) are

behavior. The similarity of the two PSFs becomes immediately evident when one applies the projection slice theorem (Appendix VI) to the two sampling formats as elaborated upon in Appendix V. As long as the $\bar{p}$-space sampling format has in any direction an extended projection, as is true for the ball and the spherical shell where the projection areas are also equal, the 3-D PSF will contain a sharp central peak. Accordingly if we were to access the $\bar{p}$-space of an object over a portion of the spherical shell (a cap) as is done in conventional monochromatic "sector scanning" or "rotational scanning" [10], [11] one can lose the 3-D imaging capabilities very rapidly as the depth of the cap diminishes (case of lensless Fourier transform hologram discussed in [11]). This is so because not all directional projections of a shallow cap are extended in area and therefore not all central slices of its PSF are of compact support (narrow extent). The above reasoning provides a new and general way of viewing imaging processes, whether broad-band or narrow, in such a way as to enhance our insight and understanding.

References

1. J.C. Dainty (Ed.) *Laser Speckle*, Springer-Verlag Berlin, (1975).
2. Special Issue on Speckle in Optics, Journal of the Optical Society of America, Vol. 66, November 1966.
3. D. Gabor, "Laser Speckle and its Elimination", IBM J. of Res. and Dev., Vol. 14, pp. 509-514, Sept. 1970.
4. N. George and A. Jain, "Speckle Reduction Using Multiple Tones of Illumination", App. Optics, Vol. 12, pp. 1202-1212, June, 1973.

References - Continued

5. H. Fuju and T. Asakura, "Effect of Surface Roughness on the Statistical Distribution of Speckle Intensity", Optics Comm., Vol. 11, pp. 35-38, May, 1974.

6. J.S. Lim and H. Nawab, "Techniques for Speckle Noise Removal", Optical Engineering, Vol. 20, pp. 472-480, May/June, 1981.

7. V.J. Corcoran, "Speckle and Specular Effects in Submillimeter Imaging", in Reference 12.

8. J.W. Goodman, "Some Fundamental Properties of Speckle (see ref. 1).

9. D.C. Champeney, *Fourier Transforms and Their Physical Applications*, Academic Press, London (1973), p. 52.

10. B.P. Hildebrand, "Acoustical Holography by Sector Scanning", J. Opt. Soc. Am., Vol. 63, pp. 1393-1348, Nov. 1973.

11. K. Yamane and M. Matsou, "Microwave Holography by Rotational Scanning", IEEE Trans. on Ant. and Prop., Vol. AP-26, pp. 280-281, March 1978.

12. R.L. Hartman, "Submillimeter Systems for Imaging Through Inclement Weather", Digest of Second Int. Conf. and Winter School on Submillimeter Waves and Their Applications, IEEE Cat. No. 76 CH 1152-8MTT, Dec. 1976.

APPENDIX XI

MICROWAVE IMAGE RECONSTRUCTION BY BACKPROJECTION

MICROWAVE IMAGE RECONSTRUCTION BY BACKPROJECTION

In this appendix we show that a method for image reconstruction other than that used in our work to date exists. The method is based on a backprojection algorithm similar to that employed in medical computerized axial tomography. The electromagnetic inverse scattering basis for the technique is briefly described here together with a Fourier optics interpretation of the backprojection algorithm. Examples of images obtained using the backprojection algorithm are presented and compared with those obtained using Fourier inversion.

Theoretical Basis

It is well known that monostatic or bistatic multiaspect scattering measurement techniques can be used to access the Fourier transform of a scattering object. The far field measured in the direction of the unit vector $\bar{l}_R$ due to plane wave illumination in the direction of the unit vector $\bar{l}_i$ of a perfectly conducting scattering body is given by,

$$\psi(\bar{p},R) = \frac{jAe^{-j2kR}}{2\pi R} \Gamma(\bar{p}) \tag{1}$$

where we have assumed monostatic probing ($\bar{l}_R = -\bar{l}_i$) with R being the distance between the transmitter/receiver and the origin in the object and where,

$$\Gamma(\bar{p}) = \int_{obj} \gamma(\bar{r})\, e^{j\bar{p}\cdot\bar{r}}\, d\bar{r} \tag{2}$$

is obtained from the measured field (1) by,

$$\Gamma(\bar{p}) = -\frac{j2R}{k} e^{j2kR} \psi(\bar{p},R) \tag{3}$$

$\bar{p}$ and $\bar{r}$ being position vectors in Fourier space and object space respectively, with,

$$\bar{p} = k(\bar{l}_R - \bar{l}_i) = p\,\bar{l}_p \tag{4}$$

and,

$$p = |\bar{p}| = \sqrt{\bar{p}\cdot\bar{p}} = 2k\cos\frac{\alpha}{2}, \quad k = \frac{\omega}{c} \tag{5}$$

Here α is the angle between $\bar{l}_R$ and $\bar{l}_i$ and the monostatic case is denoted by $\alpha = 0$. The scattering function $\gamma(\bar{r})$ represents the 3-D distribution and strengths of scattering centers on the object. It is given by the 3-D Fourier inversion of $\Gamma(\bar{p})$,

$$\gamma(\bar{r}) = \frac{1}{(2\pi)^3} \int \Gamma(\bar{p})\, e^{-j\bar{p}\cdot\bar{r}}\, d\bar{p} \tag{6}$$

Equations (2) to (5) indicate that the 3-D Fourier space of the scattering object, i.e., the Fourier transform of the scattering function, can be measured by changing k for various fixed values of $\bar{l}_p$ over a finite region of $\bar{p}$-space (Fourier space) along radial lines emanating from the origin of a p_x, p_y, p_z coordinate system. The exact shape and size of the accessed Fourier volume depends on the values assumed by the vector $\bar{p}$ i.e., on the spectral window utilized and on the range of aspect angles of the object for which the scattered field is measured.

To simplify the following analysis, without loss of generality of the results, we assume $\gamma(\bar{r})$ consists of a collection of point scatterers of amplitudes a_i located at $\bar{r}_i$ which can be represented by an array of three dimensional delta functions of weights a_i,

$$\gamma(\bar{r}) = \sum_i a_i \, \delta(\bar{r}-\bar{r}_i) \tag{7}$$

where δ is the Dirac delta function. Combining eqs. (2) and (7)

$$\Gamma(\bar{p}) = \sum_i a_i \, e^{j\bar{p}\cdot\bar{r}_i} \tag{8}$$

Now for any fixed direction $\bar{1}_p$ eq. (1) becomes

$$\psi(\omega) = \frac{j\omega e^{-j2\frac{\omega}{c}R}}{2\pi R} \Gamma\left(2\frac{\omega}{c}\bar{1}_R\right) \qquad \omega_1 < \omega < \omega_2 \tag{9}$$

The inverse Fourier transform of $\psi(\omega)/\omega$ represents the temporal impulse response of the object as measured from the direction $\bar{1}_R$. This will be,

$$g(t) \triangleq F\left\{\frac{\psi(\omega)}{\omega}\right\} = \frac{1}{(2\pi)^2} \int_{-\infty}^{\infty} H(\omega) \, e^{-j\frac{\omega}{c}R} \, \Gamma\left(2\frac{\omega}{c}\bar{1}_R\right) e^{j\omega t} \, d\omega \tag{10}$$

where,

$$H(\omega) = \begin{cases} 1 \;\ldots\ldots\; \omega_1 < \omega < \omega_2 \\ 0 \;\ldots\ldots\; \text{elsewhere} \end{cases} \tag{11}$$

represent the rectangular spectral window utilized in the measurement extending from ω_1 to ω_2. Making use of eq. (8) in (10) and making use of eqs. (4) and (5) we obtain,

$$\begin{aligned} g(t) &= \frac{1}{(2\pi)^2} \int_{-\infty}^{\infty} H(\omega) \sum_i a_i \, e^{j2\frac{\omega}{c}\bar{1}_R\cdot\bar{r}_i} \, e^{-j2\frac{\omega}{c}R} \, e^{j\omega t} \, d\omega \\ &= \frac{1}{(2\pi)^2} \, h(t) * \sum_i a_i \, \delta\left[t - \frac{2R}{c} + \frac{2}{c}(\bar{r}_i\cdot\bar{1}_R)\right] \end{aligned} \tag{12}$$

or,

$$g(t) = \frac{j}{(2\pi)^2 R} \sum_i a_i \, h[t - \frac{2R}{c} + \frac{2}{c} (\bar{r}_i \cdot \bar{l}_R)] \tag{13}$$

where h(t) is the inverse Fourier transform of $H(\omega)$. The advantage of using wide spectral windows that make h(t) approach a delta function are obvious. In that case the temporal impulse response of the object as measured from a given direction $\bar{l}_R$ will be composed of a train of narrow impulses occurring at,

$$t_i = \frac{2}{c} (R - \bar{r}_i \cdot \bar{l}_R) \tag{14}$$

All scattering centers for which

$$\bar{r}_i \cdot \bar{l}_R = \text{const} \tag{15}$$

are seen to occur at the same time. Equation (15) is that of a plane normal to $\bar{l}_R$. Therefore all scattering centers lying in a plane normal to $\bar{l}_R$ will contribute a combined echo. The impulse response g(t) represents therefore the projection of the scattering strengths of all scattering centers of the object that lie in planes normal to $\bar{l}_R$ on a line parallel to $\bar{l}_R$. In other words g(t) measures the projection of the 3-D scattering function $\gamma(\bar{r})$ of the object on a line parallel to $\bar{l}_R$ which we call the *projection line*. By repeating the measurement g(t) for a sufficiently large number of different directions $\bar{l}_R$ (different object aspects), enough such 3-D to 1-D projections can be obtained to allow reconstructing $\gamma(\bar{r})$ by backprojection. The required backprojection algorithm would consist of:

(a) Alignment of the various g(t)s in time to eliminate any unequal propagation time delay 2R/c as could occur when an array of transmitter/receiver stations is employed in interrogating the object from different

aspects and the range R between each station and a prescribed origin on the object are not equal. One way of making this alignment is the TDR method described in Appendix VII. Another is based on cross-correlating the impulse responses g(t) belonging to angularly adjacent observations (looks). Since for adjacent aspect angles the g(t)s will be caused mostly by the same scattering centers they will be highly correlated. The time displacement between adjacent g(t)'s required to achieve maximum correlation represents then the relative shift in the location of the scattering centroid of the object. The shifts between successive angularly adjacent looks can then be used to sequentially correct the time delays of the g(t)s obtain the required alignment. Once this time alignment or equivalent range correction is achieved one proceeds to the next step of the algorithm.

(b) The second step of the backprojection algorithm consist of orienting the range corrected functions g(t) in 3-D space along the directions of their $\bar{l}_R$ vectors and backprojecting or "smearing" the values of each g(t) in space into planes normal to the lines of projection and adding the results in 3-D space to reconstruct an image of $\gamma(\bar{r})$.

Our work to date has focused on accessing a single slice in the Fourier space of the scattering object by changing the object orientation in azimuth only. A projection image of the scattering centers of the object is then retrieved by Fourier inversion of the polar formated slice data or "slice hologram" (see Appendix VII). Clearly each radial line in the polar formated $\bar{p}$-space slice represents the frequency response of the object measured from a different aspect angle. Fourier inversion of the data in a given radial line yields, as discussed earlier a "temporal response" or "finite-width-impulse response" which represents essentially the projection of the scattering centers of the

3-D object on a line in the $\bar{l}_p$ direction. In other words, multiaspect frequency response measurements of an object represent indirectly the projection of the scattering centers of the 3-D object on lines of different orientations determined by the directions of viewing. This suggests as pointed out earlier that image reconstruction should be implementable using some sort of backprojection algorithm. Indeed the feasibility of such an algorithm can be appreciated by examining the coherent optical Fourier transform arrangement of Fig. 1(a) utilized in optical image retrieval. The reconstructed image resulting from the optical Fourier transform of the fan-shaped pattern $\Gamma(p,\phi)$ of the projection or slice hologram in Fig. 1(a) can be viewed as being produced by coherent superposition of the Fourier transforms of the individual radial (constant ϕ) lines in the hologram. An example of the Fourier transform of two such lines is shown in Fig. 1(b) where the Fourier transform of each line is seen to be smeared uniformly in the Fourier plane or image plane in a direction normal to each line. Superposition of these two smeared complex field patterns in the image plane provides the contribution of the data in the two radial hologram lines to the image. This Fourier optics interpretation of the optical image retrieval process should also be implementable digitally by Fourier inversion of the individual frequency responses in the projection hologram (or slice hologram) for each ϕ to obtain a collection of corresponding temporal responses. By proper temporal and angular alignment of these temporal responses as described earlier and by smearing or back-projecting each in a direction normal to its angular orientation and adding all the backprojected data at every point coherently we expect to reconstruct the image of the object. One aim of our backprojection reconstruction effort is to analyze and study backprojection algorithms digitally to

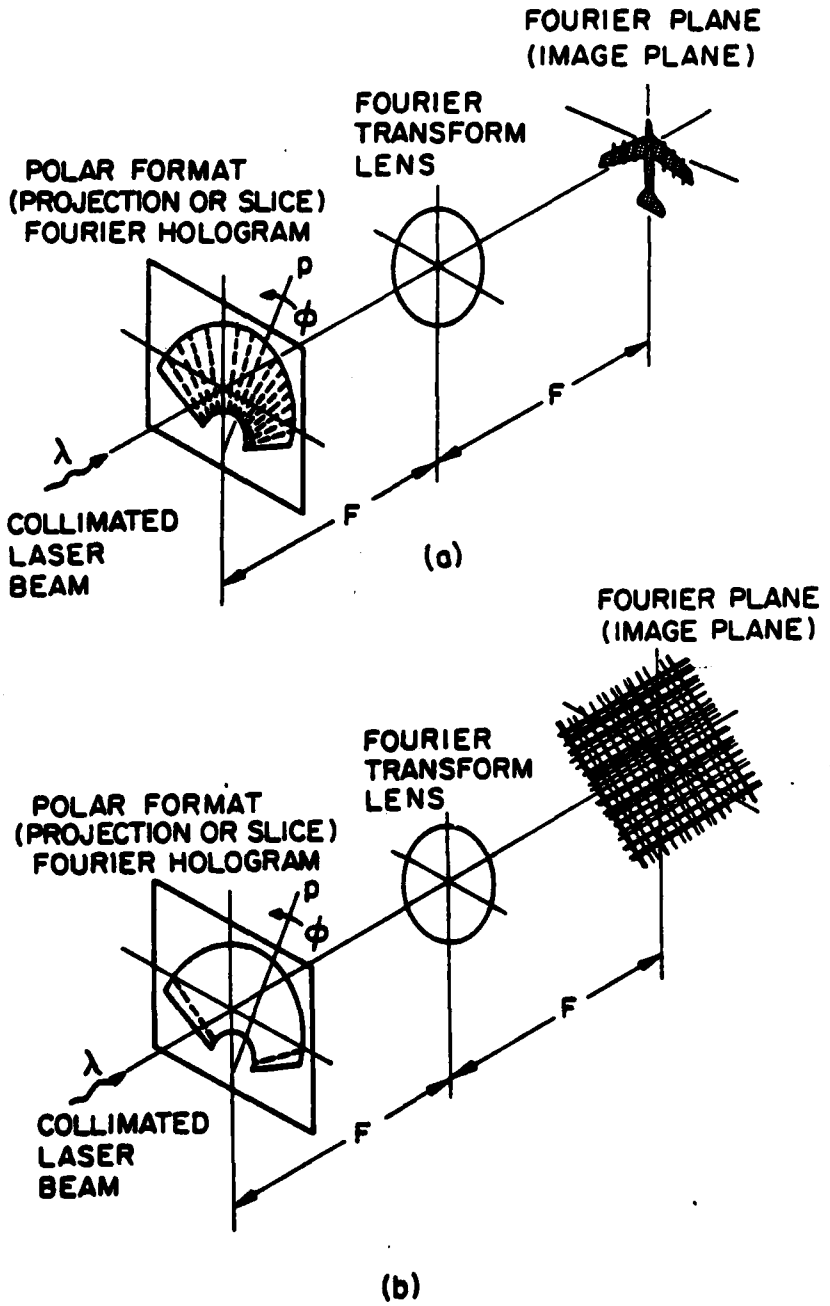

Fig. 1. Fourier optics interpretation of back-projection algorithm. (a) Optical Fourier transform of p-space projection or slice hologram. (b) Contribution of two p-space lines to retrieved image.

see whether they offer any advantages over the digital 2-D interpolation/Fourier transform method used in obtaining the images shown earlier. For example an immediately recognized advantage of the back-projection algorithm over the FFT algorithm is that it does not require data transformation from polar to rectangular formats as needed for applying the 2-D digital Fourier transform. Data interpolation may therefore not be necessary. Another advantage is that the range normalization and "phase tweeking" algorithm described in Appendix VII are directly applicable to the temporal response data for synthesis of a TDR. It is also an aim of this aspect of our study to apply a variety of filtering operations, that have been successfully utilized in tomographic x-ray reconstruction from back-projections, to the temporal response data before backprojecting and reconstructing the image and to assess their influence on image quality.

Experimental Results

Preliminary results of an image retrieved by digital implementation of the backprojection algorithm described above are presented in Fig. 2. The data utilized is that of the B-52 scale model test object collected as described in Appendix VII and employed there to retrieve the image shown in Fig. 4 of that Appendix by Fourier inversion. Figure 2 shows a sequence of 3 photographs illustrating how the image emerges as data from an increasing number of projections are added. In obtaining the result in Fig. 2 each line in the $\bar{p}$-space data utilized was individually multiplied by a ramp function or passed through an R&L filter [1] before Fourier inversion to obtain the corresponding temporal impulse responses to which backprojection is applied after temporal and angular alignment. Comparison of the result in Fig. 2

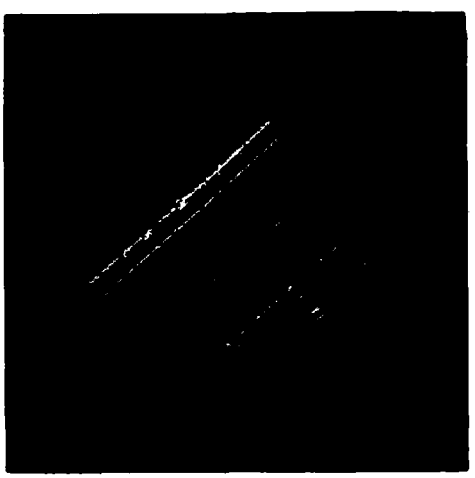

(a) From first projection alone

(b) First ten projections

(c) Reconstructed image from all 128 projections

Fig. 2. Results of backprojection reconstruction of B-52 employing ramp filtering.

and that in Fig. 4 of Appendix VII obtained by Fourier inversion shows that the backprojection algorithm produces sharper images of the visible scattering centers of the B-52 but with "wispy" trailing edges. The image shown in Fig. 2 represents the first backprojection reconstruction of a microwave object from realistic data. Growing interest in the back projection algorithm is becoming evident in the literature for some of the reasons indicated earlier [2],[3]. Work on this aspect of our research program is continuing.

References

1. G.N. Ramachandran and A.V. Lakshminarayan, "Three Dimensional Reconstruction from Radiographic and Electron Micrographic Application of Convolution Instead of Fourier Transforms", Proc. Mat. Acad. Sci. U.S., Vol. 68, pp. 2236-2240, 1970.

2. C.C. Aleksoff, I.J. LaHaie and A.M. Tai, "Optical-Hybrid Backprojection Processing", Proc. 10-th Int. Opt. Computing Conference, IEEE Cat. No. 83CH1880-4, p. 89.

3. D. Munson Jr., J.D. O'Brien and W.K. Jenkins, "A Tomographic Formulation of Spotlight-Mode Synthetic Aperture Radar", Proc. IEEE, Vol. 71, Aug. 1983, pp. 917-925.

END

FILMED

1-84

DTIC